# Development of 2-DOF haptic devices working with magnetorheological fluids

Bin Liu
University of Wollongong

# Development of 2-DOF Haptic Devices Working with Magnetorheological Fluids

A thesis submitted in fulfilment of the requirements
for the award of the degree of

**Master of Engineering – Research**

by

**Bin Liu**

**B.Eng., Harbin Engineering University, China, 2003**

from

**Faculty of Engineering, University of Wollongong**

**February 2006**

Wollongong, New South Wales, Australia

# CERTIFICATION

I, Bin Liu, declare that this thesis, submitted in partial fulfilment of the requirements for the award of Master of Engineering – research, in the School of Mechanical, Materials and Mechatronic, Faculty of Engineering, University of Wollongong, is wholly my own work unless otherwise referenced or acknowledged. The document has not been submitted for qualifications at any other academic institution.

Bin Liu

5th March 2006

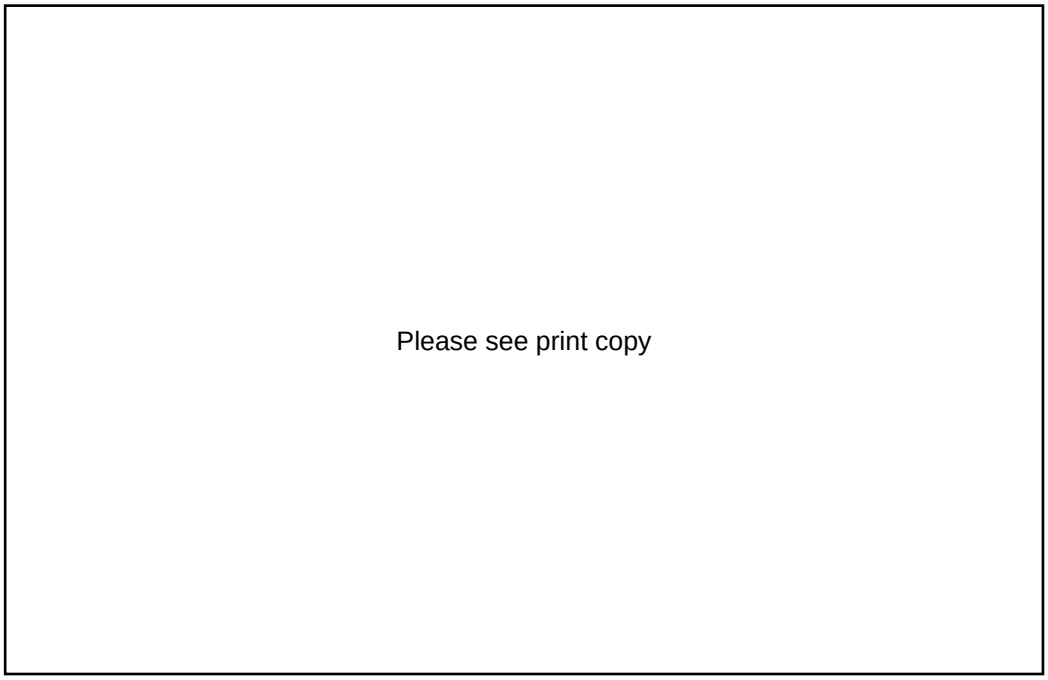


*To my parents and all the people I love*

# ACKNOWLEDGEMENTS

I wish to thank my supervisor, Dr. Weihua Li, for his enthusiastic support, professional direction, and constant encouragement that inspires me to overcome the challenges on my road of life and study.

Pure-hearted appreciations are also due to my co-supervisor, Buyung Kosasih, for his helpful direction on mechanical design and on my thesis writing revision. Particular thanks are extended to Mario Solitro, Michael Geantham, Keith Maywald and Ron Marshall for their help on electrical design and mechanical manufacturing for this project. Thanks are also extended to Troy Coyle, Meeta Padmanabhan, John Burnard (Uniting Church) and Stephen Jeffrey (University of Queensland) for their kind assistance and discussions. Special thanks are expressed to Rui Du for her constant encouragement and empressement during my study period.

Finally, I would like to thank my parents for their love, encouragement, and financial support.

# TABLE OF CONTENTS

# LIST OF FIGURES

# LIST OF TABLES

# LIST OF SYMBOLS

| | |
|---|---|
| $\tau$ | shear stress of the MR fluids |
| $\tau_y$ | yield stress of the MR fluids |
| B | magnetic induction intensity |
| H | intensity of magnetic field |
| $\dot{\gamma}$ | shear strain rate |
| $\eta_0$ | field-independent plastic viscosity of MR fluids |
| $\eta_{app}$ | apparent viscosity of MR fluids |
| K | consistency index in apparent viscosity model of MR fluids |
| F | shear force in the shear mode |
| $F\eta$ | shear force without applied magnetic field in the shear mode |
| $F\tau$ | shear force related to applied magnetic field in the shear mode |
| A | area of the working surface |
| L | length of the working surface |
| W | width of the working surface |
| g | gap between the two working surfaces |
| $\Delta P$ | pressure drop in the flow mode |
| $\Delta P_\eta$ | pressure drop without applied magnetic field in the flow mode |
| $\Delta P_\tau$ | pressure drop related to applied magnetic field in the flow mode |
| Q | volumetric flow rate in the flow mode |
| c | function of the flow velocity |
| $\omega$ | angular velocity of the rotary disc |
| $h$ | MR fluid gap in the disc-shaped actuator |

| | |
|---|---|
| $r$ | position on the rotary disc surface |
| $r_{inner}$ | inner radius of the rotary disc |
| $r_{outer}$ | outer radius of the rotary disc |
| T | resistant torque |
| N | number of the turns of the coil |
| I | current in the coil |
| $H_f$ | magnetic intensity in the MR fluid gap |
| $H_s$ | magnetic intensity in the steel |
| $L_g$ | width of the MR fluid gap |
| $L_s$ | length of the steel path |
| $\mu_o$ | permeability of free space |
| $\mu_r$ | relative permeability of MR fluids |
| $\Phi$ | value of magnetic flux |
| Da | radius of MR actuator |
| Dc | thickness of the casing |
| Dd | thickness of the disc |
| Df | thickness of MR fluids gap |
| Dp | thickness of the plate |
| $T_0$ | initial resistant torque in the sub-hysteresis model |
| $I_s$ | constant electric current difference in the sub-hysteresis model |
| $S_1$ , $S_2$ | two constant slopes of $T$ in the sub-hysteresis model |
| $I_t$ , $I_b$ | two vertexes of sub-hysteresis loop |
| $\theta$ | degree of the longitude of the spherical coordinates |
| $\phi$ | degree of the latitude of the spherical coordinates |

| | |
|---|---|
| $\alpha_x$ , $\alpha_y$ | rotation degree of the two MR actuators |
| $M_\varphi$ | resistant torque along latitude direction of the spherical coordinates |
| $M_\theta$ | resistant torque along longitude direction of the spherical coordinates |
| $M_x$ | resistant torque along X direction of the rectangular coordinates |
| $M_y$ | resistant torque along Y direction of the rectangular coordinates |
| R | value of the resistance |
| C | value of the capacitance |
| $f_c$ | cut-off frequency of the filter |
| $U_i$ | input voltage |
| $U_o$ | output voltage |

T1, T2, T3, T4 transistors

# ABSTRACT

The thesis presents the design and development of a 2-DOF (degree of freedom) magnetorheological (MR) fluid based haptic joystick and studies its applications in virtual reality. MR fluids are controllable fluids that can generate adaptable resistance forces when subjected to a magnetic field. This feature is capable of realizing novel haptic devices.

The developed system consists of three main parts: MR joystick, control and display hardware, and software. The MR joystick is constructed of two disc-shaped MR actuators positioned perpendicularly with a gimbal structure, which transfers the movement of the joystick handle into two actuator rotary movements. Therefore, operators can feel the resisting force generated by the two actuators. The dimensions of the actuators have been optimized using finite element analysis, and the steady-state performance of the actuators has been measured and analyzed. The kinetics of the joystick in terms of working space and resistance will be discussed. In the thesis, a subhysteresis model and a torque converting method will be employed to enhance the accuracy of the force control.

The applications of the MR joystick in virtual reality will be demonstrated by using six typical interface examples designed in LabVIEW. These demonstrations show that the MR haptic devices have a huge application potential in entertainment, medical, and general industry fields.

# CHAPTER 1
# INTRODUCTION

## 1.1 BACKGROUND AND MOTIVATION

Virtual reality (VR) technology is regarded as a natural extension to 3D computer graphics with advanced input and output devices. It brings a completely new environment to the CAD (computer aided design) community. VR offers many advantages compared with traditional CAD. It provides intuitive 3D interaction, direct manipulation, and 3D immersion. The use of VR enhances the user's understanding of a virtual object. It helps to speed up the design process and permits a designer to smoothly develop his concepts, thus fully developing his creativity. Although many significant achievements have been obtained, virtual reality is most often a laboratory term that is able to immerse people in a digital world and make users feel as though they were in a location other than their physical place. We will be seeing the real applications coming into our daily life in the entertainment, education, and medical fields. For a successful VR application, effective and sensitive haptic devices need to be designed to transfer perceptual information between the users and the virtual environment.

A variety of haptic devices have been developed for different applications to simulate the virtual reactions of VR, such as the force feedback mouse and the haptic exoskeleton. It should be noted that conventional haptic devices are based on motor control to provide force and torque. Since it is hard for traditional devices with motor control to accurately simulate forces and some high viscosity environments in VR, some prior projects tried to overcome the disadvantages of the current haptic interfacing systems by introducing some "smart" materials, such as electrorheological (ER) fluids, that is, substances that can change their rheological characteristics on application of an electric field [1]. However, to generate a 2-5 kPa yield stress, ER fluids need a high field of 2-5kV/mm. This yield stress is not adequate for real industrial applications, and the high electric field requirement is not safe for the users. Furthermore, impurities in ER fluids affect their performance significantly. This means that ER devices cannot keep working well in complicated circumstances for a long period. In terms of safety,

performance, and stability, magnetorheological (MR) fluids show more potential in VR applications than ER fluids.

MR fluids have become commercially available in the last decade, since it is now possible to design simple, noiseless, and fast transducers working as interfaces between electronic control systems and mechanical systems. The novel characteristic of MR fluids is their ability to reversibly change from a liquid to a semi-solid state in milliseconds when exposed to a magnetic field. This feature makes it possible for MR fluids to provide a wide range of resistance torques by changing their yield stresses to fulfill different application requirements. For example, MR dampers can be used as suspension systems for different vehicles fitting different road conditions. This application provides the drivers with comfortable and safe driving conditions. In the aviation field, MR landing systems make passengers and crewmen feel less stroke force at the moment of landing or taking off of an aircraft. In civil engineering, MR shake absorbers are being broadly adopted to minimize the shaking of buildings and bridges in strong wind and earthquake conditions. This project is attempting to widen the applications of MR devices based on current research results and in particular, aims to develop an MR haptic system for VR applications.

## 1.2 AIMS AND OBJECTIVES

The objective of this project is to develop an effective 2-DOF MR haptic joystick for VR applications. This haptic system, based on a haptic device and real-time control and display software, would be used for the purposes of entertainment, virtual manufacturing, and medical surgical simulation. . The project is divided into several parts in terms of the functions of the different components of the system. Specific objectives are as follows:

1) Design, manufacturing, and testing of MR actuators
2) MR joystick development and analysis
3) Electrical circuit design
4) Software design
5) VR application demonstrations

## 1.3 THESIS OUTLINE

The thesis begins with a literature review on MR technology, virtual reality and haptic devices in *Chapter 2*, which gives readers a comprehensive overview of the achievements of previous research and the aim of this project. *Chapter 3* gives an overview of the design of the whole haptic system by explaining the interactions among the MR actuators, the joystick, the power amplifier, and the host computer. The design and analysis of MR actuators are explained in *Chapter 4*, in which the performance and the structure of the MR actuator are optimized by the finite element method (FEM). *Chapter5* addresses the testing of the steady-state performance of MR actuators. A parametric steady-state torque model is proposed to accurately predict the actuator performance. A 2-DOF joystick using two MR actuators is constructed and designed in *Chapter 6.* The working space and the space deformation of the joystick are also presented in this chapter. *Chapter 7* covers the method of data acquisition (DAQ) and the design of the power amplifier that is used to amplify the control signal and to drive the MR actuators. The software design, including control unit and display unit design, is described in *Chapter 8*, and several application demonstrations are presented at the end of this part. *Chapter 9*, as the final part of this thesis, consists of a conclusion that reviews and summarises the project. Further research work is also discussed in this chapter.

# CHAPTER 2

# LITERATURE REVIEW

## 2.1 INTRODUCTION

The aim of this project is to develop an effective magnetorheological (MR) haptic device for virtual reality (VR) applications. Therefore, this literature review deals with the combined technologies of MR fluids, VR and haptic devices.

MR fluids, the spirit of this project, are suspensions of microsized particles dispersed in nonmagnetic carrying fluids. Such fluids exhibit unusual characteristics in that their rheological properties can be continuously and reversibly changed within milliseconds solely by applying or removing a magnetic field. This feature has inspired the design of a large variety of MR devices [2,3].

VR will step into real life from the laboratories in the near future. Throughout the relatively short history of computer graphics, engineers have striven to develop more realistic, responsive, and immersive means for human beings to interact with computers. Generally speaking, VR immerses the users in a computer-based visual world by showing information to the users through a flat monitor. The users are able to feel as though they were in a location other than their physical place by a combination of the virtual environment and certain haptic devices [4].

A complete haptic interface usually includes several sensors and actuators in contact with the user in order to apply mechanical signals to several distinct parts of the human body, and to measure the corresponding mechanical signals at the same areas of the body. These signals should refer to forces, displacements, or a combination of these and their time derivatives. On the other hand, the haptic system is the computational system that is used to drive the actuators. The function of this computational system is to provide haptic rendering capabilities. Haptic rendering, however, stresses the bi-directional exchange of information between the interface and the user [5]. By combining both traditional audio and video systems, the haptic system contributes to the

interaction of human and machine. Such a system usually contains two interfaces. One relates to the computer; the other relates to human beings. The computer interface is the information exchange port between the haptic device and the computer, which acts as the virtual environment generator and control unit for the whole system. The haptic device gets the control information and sends position signals back to the computer through this interface. The human interface provides different kinds of perceptual information, allowing the user to feel the virtual environment. Users receive feedback from the environment designed in the computer. The haptic system provides users with integrated perception in the particular entertainment, virtual manufacturing, or medical training area.

In this chapter, a review of the literature relevant to current knowledge and achievements in the above three areas is carried out. The information refined from previous literature has given rise to the principles and foundation of the MR haptic system and inspires creative innovations in this project.

## 2.2 MR TECHNOLOGY

### 2.2.1 MR Effect

MR fluids are suspensions of microsized particles dispersed in a nonmagnetic carrier fluid. Such fluids exhibit unusual characteristics in that their rheological properties can be continuously and reversibly changed within milliseconds solely by applying or removing a magnetic field. The ideal MR fluid is proposed to possess the following features: noncorrosive, stable against settling, high magnetic saturation, large field-induced yield stress, but small apparent viscosity in the absence of an applied field [6].

The initial discovery and development of MR fluids can be credited to Jacob Rabinow at the US National Bureau of Standards in the late 1940s [7]. An MR fluid is a free-flowing liquid without the influence of a magnetic field. In the condition of being exposed to a magnetic field, the material is able to transform from a liquid to a semi-solid state. A reversible change occurs on removal of the activating magnetic field, so the fluid is able to return back to its original free-flowing liquid state. The change of physical property in an MR fluid depends on the intensity of the applied field [8,9].

An MR fluid shows the MR effect by a considerable increase in its apparent yield stress with enhancement of the magnetic field. A simplified explanation for the change in apparent yield stress in MR fluids is shown in Fig. 2.1. Without a magnetic field (Fig. 2.1(a)), the particles are randomly dispersed in the suspension, and the fluid behaves as a Newtonian fluid. When an external magnetic field is applied, the particles become magnetised, become nearly single domain, and behave like tiny magnets. Magnetic interactions between these particles can be minimised if the magnetic particles line up along the direction of the magnetic field (Fig. 2.1(b)). A shear stress or a pressure difference is needed to disrupt this structure formed in energised MR fluids [10]. The strength of the fluid, i.e. the value of the apparent yield stress, increases as the applied magnetic field increases.

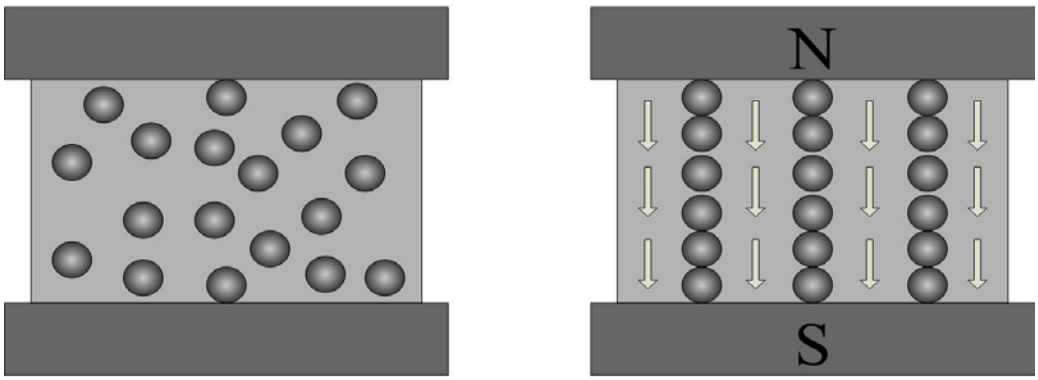


(a) No magnetic field is applied; (b) Magnetic field is applied.

Figure 2.1 The MR effect.

For example, the apparent viscosity of the fluid can be increased by 2 to 3 orders of magnitude, which occurs almost instantaneously. Furthermore, removal of the applied field returns the MR fluid to its initial state.

### 2.2.2 Composition of MR Fluids

Most often, MR fluids are made out of three main components: ferromagnetic particles, stabilizer, and carrier fluid [11].

Particulate materials for the MR fluids generally used are ferromagnetic or paramagnetic particles, with a typical size range of 1-10 μm in diameter. If the size of particles becomes smaller, the Brownian motion [12] will prevent sedimentation and the formation of linear aggregates, and destroy the chain-like structure, leading to a decrease in the yield stress. On the other hand, particles larger than 10 μm make it difficult to prepare MR fluids that are stable against sedimentation [10]. Furthermore, monodisperse particles are preferred to optimize the MR effect. In addition, monodisperse particle based MR fluids are helpful to understand cluster formation and the aggregation mechanisms of magnetic particles, such as iron or iron-based particles [13].

The function of a carrier liquid is primarily to provide a liquid in which the particles are suspended in the magnetically active phase. The approximate relative volume fractions of the liquid phase range from 50% to 90%. Silicone oils, synthetic or semi-synthetic oils, mineral oils, lubricating oils, and combinations of these and many other polar organic liquids and water have all been reported to be used as carrier liquids. In general, ideal carrier fluids should have a low initial viscosity, good anti-corrosion properties, and a wide range of temperature stability.

The small amount of extra stabilizer is to avoid gravitational settling of the particles, aiding the particles in remaining suspended in the carrier fluid. The additives also enhance lubrication and inhibit wear, thus promoting longer life in the MR devices. The stabilizer particles are non-porous and can be spherical in shape with a diameter of 0.005~0.015 μm. Inorganic silicon components are typical stabilizers.

### 2.2.3 MR Rheology

The Bingham visco-plasticity model, as shown in Fig. 2.2, is widely used to describe the field-dependent MR fluid characteristics [14]. In this model, the total post-yield shear stress is calculated by

$$\tau = \tau_y(H)\,\mathrm{sign}(\dot{\gamma}) + \eta_0\dot{\gamma} \qquad (2.1)$$

where $\tau_y$ is the yield stress due to the applied field; H is the magnitude of the applied magnetic field; $\dot{\gamma}$ is the shear strain rate; and $\eta_0$ is the field-independent plastic viscosity. The post-yield shear stress expresses the dynamic shear stress of the fluid, and the fluid post-yield viscosity is assumed to be a constant in the Bingham model. Based on this model, the apparent viscosity ($\eta_{app}$) of the MR fluid is shown in Eq. 2.2, which is defined as the ratio of the shear stress to the shear rate.

$$\eta_{app} = \tau / \dot{\gamma} = \tau_y / \dot{\gamma} + \eta_0 \tag{2.2}$$

Please see print copy for Figure 2.2

Figure 2.2 Visco-plasticity model of MR fluids [14].

Further experiment shows that the apparent viscosity of MR fluids is not a constant and appears as a decreasing trend with shear rate, which is known as shear-thinning behavior [14,15]. In terms of the experimental results, a Herschel-Bulkley visco-plasticity model [16] is employed to accommodate this effect. In this model, the constant post-yield plastic viscosity in the Bingham model is replaced with a power law model dependent on the shear strain rate. Therefore,

$$\dot{\gamma} = 0 \qquad |\tau| \le \tau_y \tag{2.3a}$$

$$\tau = \tau_y \operatorname{sign}(\dot{\gamma}) + (K|\dot{\gamma}|^{(n-1)})\dot{\gamma} \quad |\tau| > \tau_y \tag{2.3b}$$

Where $\tau$ , $\tau_y$ and $\dot{\gamma}$ are the shear stress, the yield stress and the shear rate, respectively. K is the consistency index, and n is the power-law index.

The apparent viscosity according to the Herschel-Bulkley model is given by

$$\eta_{app} = K\dot{\gamma}^{(n-1)} \quad \begin{cases} n<1 & \text{Shear - thinning} \\ n=1 & \text{Bingham Model} \\ n>1 & \text{Shear - thickening} \end{cases} \tag{2.4}$$

Eq. 2.4 indicates that the apparent viscosity decreases as the shear strain rate increases when n<1 in the shear thinning effect. The second condition is used to describe the fluid shear thickening effect when n>1. The Herschel-Bulkley model reduces to the Bingham model when n=1.

### 2.2.4 MR Devices

**(a) The working models**

MR devices often operate in shear-mode or flow-mode as shown in Fig. 2.3. The shear mode works when one surface moves through the fluid with respect to another one [17]. The magnetic field is perpendicular to the direction of the motion as shown in Fig. 2.3(a).

Please see print copy for Figure 2.3

Figure 2.3 MR fluid working modes [17].

An MR based clutch is a good example of the shear mode, and the equation corresponding to the shear mode is given by:

$$F = F_{\eta} + F_{\tau} = \frac{\eta SA}{g} + \tau_y(H)A \tag{2.5}$$

where F is the resultant force based on the effective area. A is the area of the working surface (A=LW, where L, W are the length and the width of the surface), g is the gap between the two surfaces, S is the relative pole velocity, $\eta$ is the viscosity with no applied field, and $\tau_y$ is the yield stress developed in response to an applied field H.

The flow mode is characterized by two static surfaces with the magnetic field normal to the flow [18], as shown in Fig. 2.3(b). In this mode, the magnetic field can be used to control flow resistance and the pressure drop across an MR valve structure. The corresponding equation is described by

$$\Delta P = \Delta P_{\eta} + \Delta P_{\tau} = \frac{12\eta QL}{g^3 W} + \frac{c\tau_y(H)L}{g} \tag{2.6}$$

where Q is the volumetric flow rate and c is a function of the flow velocity profile with a value ranging between 2 and 3.

A comparative study of the different working modes indicates that the shear mode produces a more effective damper [19]. In shear mode, the dampers show a smaller initial force without the effect of the magnetic field and provide better controllability than in other modes. Various MR damper designs based on different modes and the combination of different modes can be found in the literature [10, 20].

**(b) The applications**

MR fluid-based devices have recently achieved commercial success in a number of industrial applications, such as damping equipment for vehicle seat vibration control [21, 22], primary suspensions [23, 24], shock absorbers [22, 25], and engine mounts [25, 26, 27]. In this section some of the main application areas of MR fluids are reviewed.

A main application area for MR fluids is in devices for torque transfer, which include brakes and clutches [28]. Fig. 2.4(a) shows a picture of an MR fluid-based disk-type brake. MR fluid-based brakes are currently commercially available from the Lord Corporation and are being used in various types of exercise equipment [29, 30].

MR dampers, shown in Fig. 2.4(b), can be used as the suspension system for different vehicles fitting different road conditions. This application provides the drivers with a comfortable and safe driving environment. In the aviation field, MR landing systems make passengers and crewmen feel less stroke force at the moments of landing and taking-off of an aircraft. In civil engineering, MR shock absorbers are being broadly adopted to minimize the shaking of buildings and bridges in strong wind and earthquake conditions.

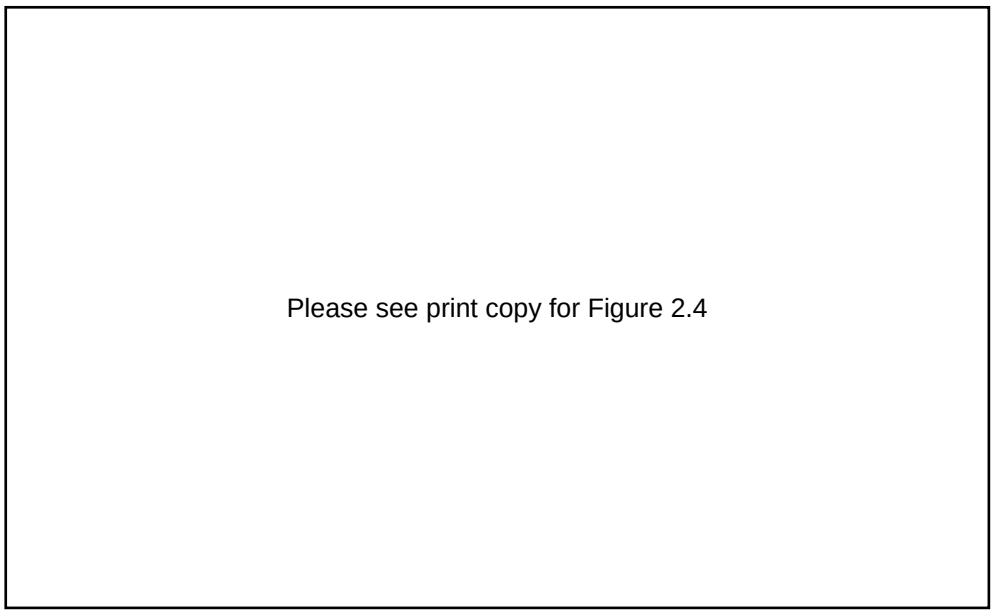


Figure 2.4 Typical MR devices [25].

## 2.3 VIRTUAL REALITY AND HAPTICS

### 2.3.1 Virtual Reality

Our society is increasingly generating ever-larger amounts of information, while the information is also increasingly available in digital format, and the question of how to use this data efficiently emerges. VR is increasingly regarded as the most promising solution for this problem, as VR can potentially communicate large amounts of data in an easily understandable format. Virtual environments are expected to have an immense impact on our ability to deal with information [31, 32, 33].

### 2.3.2 Types of VR Systems

Most configurations fall into three main categories: non-immersive systems, semi-immersive projection systems, and fully immersive systems. Non-immersive systems, as the name suggests, are the least immersive implementation and the lowest cost VR techniques. Semi-immersive systems are usually comprised of a relatively high performance graphics computing system that can be coupled with a large display device. The most direct experience of virtual environments is provided by fully immersive VR systems. To achieve full immersion the user has to employ a head-coupled display that is either head mounted or arranged to move with the head. A summary of the VR classification is shown in Table 2.1 [33].

Please see print copy for Table 2.1

Table 2.1 Types of VR systems.

### 2.3.3 Taxonomy of Physical Media

Physical media are needed for the users to be immersed in any type of the systems described above. The physical media of VR can be classified into Input Media and Output Media, based on Bernsen's physical media classification [34].

| Input media: | Output media: |
|---|---|
| Acoustics | Graphics |
| Graphics | Acoustics |
| Kinaesthetics | Haptics |

Table 2.2 Physical media classification for VR

Graphics and acoustics appear in both of the input and output media that are the first things be conceptualised by people when VR is mentioned. Graphics means video capturing with possibly gesture recognition and environmental display as the input and output media, respectively, providing mutual video and audio information for the user. Thus the virtual environment can be influenced and contorted by a simple gesture or voice command. Meanwhile, the user can get video and sound feedback.

Kinaesthetics and haptics are the counterpoints in the conception of VR media. Kinaesthetics represents the movement of different parts of the body, i.e. fingers and arms, which expresses the motion behaviour of the user. Therefore, the user can feel corresponding force feedback based on the motion information and the VR, which is called haptics. Kinaesthetics and haptics provide users with more realistic and vivid perception, depending on the sophisticated properties of haptic devices that will be introduced in the following sections.

## 2.4 HAPTICS

### 2.4.1 Haptic System Components

Haptic interfaces can be viewed as an approach to addressing the kinaesthetic limitations in a VR system. It is thus possible to classify haptics in the area of computer-human interfaces. Unlike traditional interfaces that provide visual and auditory information, haptic interfaces generate mechanical signals that stimulate human kinesthetic and touch channels. Haptic interfaces also provide humans with means to act on their environment.

It is possible to discuss the function of a haptic interface by considering on the one hand an input device and on the other a display device. The traditional graphic display emphasizes uni-directional information transfer like that of a typical joystick. The basic difference can be understood from Fig. 2.5, in which a regular joystick is compared to a haptically enabled joystick with programmable mechanical properties, with the arrows representing the direction of information flow. With a typical joystick, this is limited to a unidirectional input from the joystick to the computer. The user of a conventional joystick receives almost no information from its movements, although its friction and inertial properties may assist the user in performing skilful movements. However, the haptic joystick can provide the user with programmable feedback based on the sense of touch, allowing a faster and more intuitive interaction with the machine.

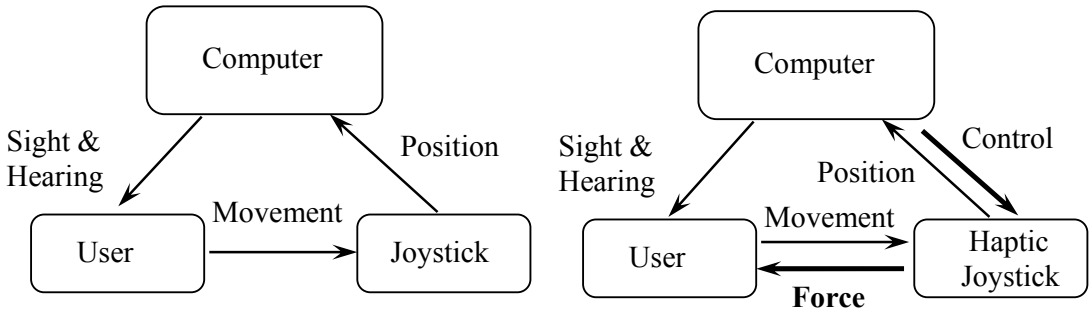


Figure 2.5 Comparison between conventional interface and haptic interface.

By combining with both traditional audio and video systems, the haptic system contributes to the interaction of human and machine. Such a system usually contains two interfaces. One is interfaced to the computer; the other is interfaced to the human. The computer interface is the information exchange ports between the haptic device and the computer, which acts as the virtual environment generator and control unit for the whole system. The haptic device gets the control information and sends position signals

back to the computer from this interface. The human interface provides different kinds of perceptual information that allow the user to feel the virtual environment. Users can get feedback from the environment set up in the computer. As a result, the haptic system provides the users with an integrated perception for applications in the entertainment, virtual manufacturing, and medical training areas.

### 2.4.2 Haptic Devices and Applications

A variety of haptic devices have bloomed for different applications in the last decade. The earliest one is the Programmable Keyboard, the result of a project headed by Cadoz and Ramstein [35], which consists of a piano-like keyboard providing computer-driven force feedback for each of its sixteen keys. Augmented Mice is an innovative system described by Akamatsu *et al*. [36]. It has a similar shape and function to a computer mouse and includes two haptic feedback features. One is an electromagnetic braking system, which provides programmable dissipative friction forces, and the other is a transducer to provide vibro-tactile sensations. The trackball appeared on the market in 1996. Keyson developed a haptic device in the form of a familiar trackball that was used to gain many insights into the effects of haptic feedback in graphical user interface navigation. Two small DC motors drove the ball through a friction drive, providing two degrees of freedom of independent feedback [37].

The latest and the most successful haptic device is the Phantom system. The initial design is described by Massie and Salisbury, and the Phantom system is commercially available [38]. A picture of the three generations of the Phantom system is attached below in Fig. 2.6. There are several variants, but generally a stylus is grasped, or a thimble braces the user's finger. There are six actuated degrees of freedom and six sensed orientations. A key design aspect is a capstan drive, which avoids the use of gears and makes it possible to amplify the torque of small DC motors with a concomitant increase in damping and inertia.

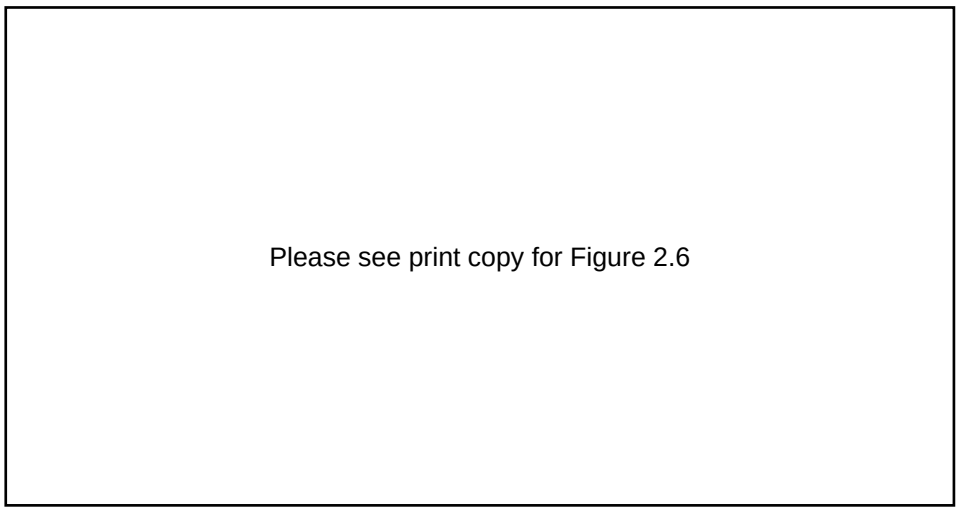


Figure 2.6 The PHANTOM system [39].

The main applications fields of haptic devices are briefly discussed in the following subsections:

**(a) Entertainment**

Modes of interaction and the sense of user immersion are greatly enhanced by applying force feedback to the game player. Force feedback is already at the commercial stage for simulation in games involving driving, piloting, exploring, and so on.

**(b) Medical training and surgery**

Various haptic interfaces for medical simulation may prove especially useful for training in minimally invasive procedures and remote surgery using teleoperators. In the future expert surgeons may work from a central workstation, performing operations in various locations, with machine setup and patient preparation performed by local nursing staff.

**(c) Virtual manufacturing**

In manufacturing, many opportunities exist. For example, haptics can assist design for assembly, in terms of reducing the need for prototyping, as well as for rapid prototyping. It is also possible to assess human maintainability of complex systems

before they are built [40]. Programming of complex manufacturing devices such as numerically controlled machines and robots can be facilitated.

### 2.4.3 ER and MR Haptic Devices

Some typical ER and MR haptic devices with various applications will be demonstrated in this section.

The first device is a tactile display that is used to produce tactile sensing on the skin of the operators. This tactile display directly activates nerve fibres within the skin by means of an electrical voltage across an ER surface [41, 42], thus generating sensations of pressure or vibration without the use of any mechanical actuator. ER fluid (ERF) in the tactile array is subjected to both squeeze and shear modes as shown in Fig. 2.7.

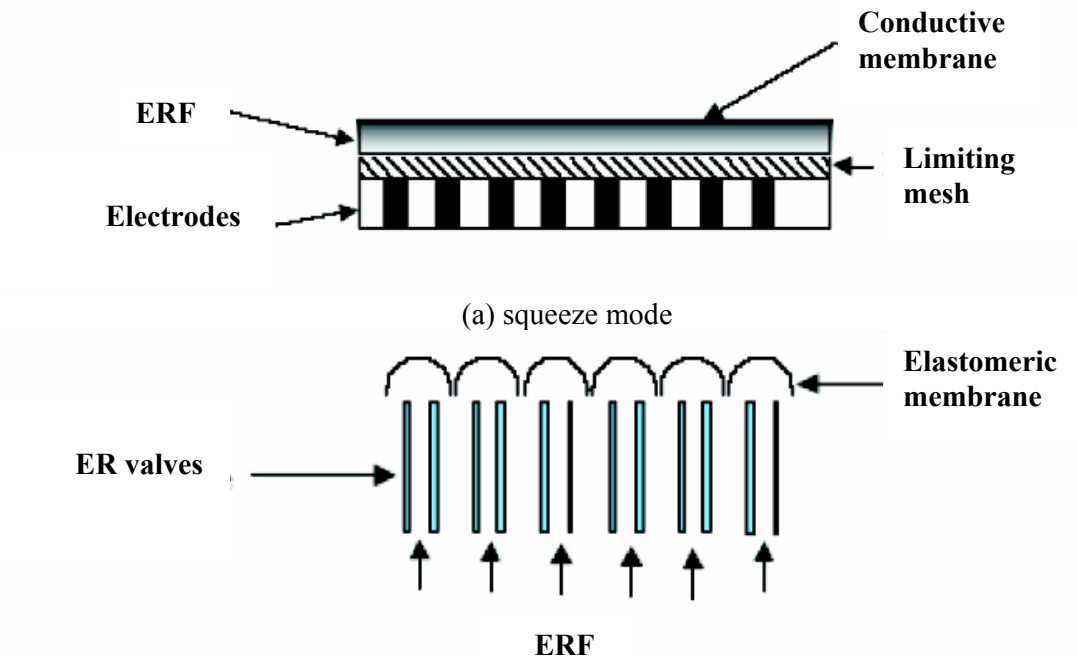


Figure 2.7 ER tactile displays with different modes.

The stiffness of the ER fluids in the squeeze mode is controlled by the electrodes mounted in the bottom of the actuator. The ER fluids held between the limiting mesh and the surface membrane change the hardness of the contact surface. In the flow mode, the surface strength of the actuator can be controlled by limiting the pressure of the ER

fluids. The ER valves can control the pressure of the ER fluids in both static and dynamic ways, so people can feel either a fixed or a changing force from the surface.

A similar structure was designed by Richard [43]. The direct-wired electrodes are used to form one half of the sensing and actuation capacitors. The outer rubber membrane is conductive and grounded, and forms the other half of all the sensing and actuation capacitors. The structure of this sensor is shown in Fig. 2.8

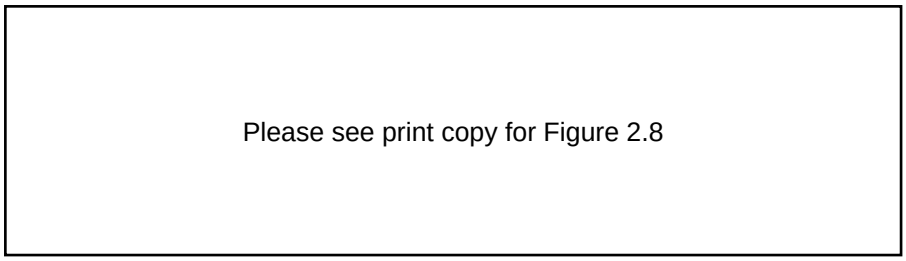


Figure 2.8 ER tactile sensor.

ER force feedback devices are developed to produce more complicated and more comprehensive virtual forces instead of the fingertip forces simulated by tactile displays. To this end, a novel ER-fluid-based haptic system called MEMICA was proposed at Rutgers University [44]. MEMICA is intended to provide human operators with an intuitive and interactive feeling of the stiffness and forces in remote or virtual sites in support of space, medical, underwater, virtual reality, military, and field robots performing dexterous manipulation operations. Fig. 2.9 shows the ER haptic glove of the MEMICA system.

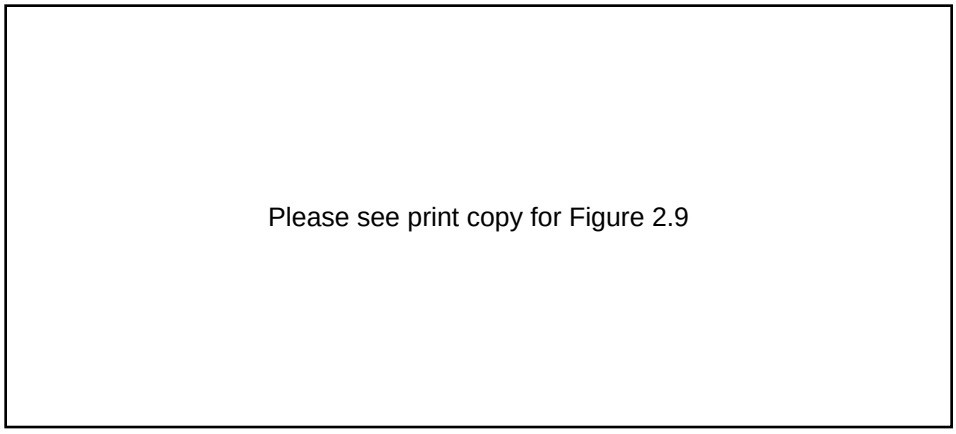


Figure 2.9 The ER haptic glove of the MEMICA system.

The ERF-based joystick was developed at Rutgers University in 2003 as shown in Fig. 2.10 [45]. The ER haptic joystick mechanism has two degrees of freedom, which require one actuator for each degree of freedom. The actuators are mounted at right angles to each other, and the central part is a two degree of freedom joint on which the joystick handle is mounted. Operators can feel the ER resistant force by means of this handle.

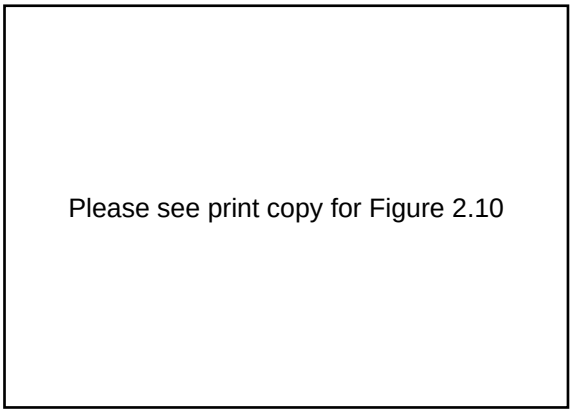


Figure 2.10 Joystick with ER actuators.

ER haptic devices have limited applications because they are unable to provide sufficient force to meet the requirements of large force and torque applications. ER joysticks can only provide a maximum torque of about 0.5 Nm, which is too small to allow a real haptic application for humans. MR devices have emerged to overcome the drawbacks of ER haptic devices.

An MR haptic glove was developed by adopting several compact MR disc-shaped actuators to generate torque on the back of each finger [46]. These actuators can work together through a link structure to simulate the virtual force, which is strong enough for large force applications. The heaviness of the glove is a significant disadvantage for effective simulation. A picture of the glove is shown in Fig. 2.11.

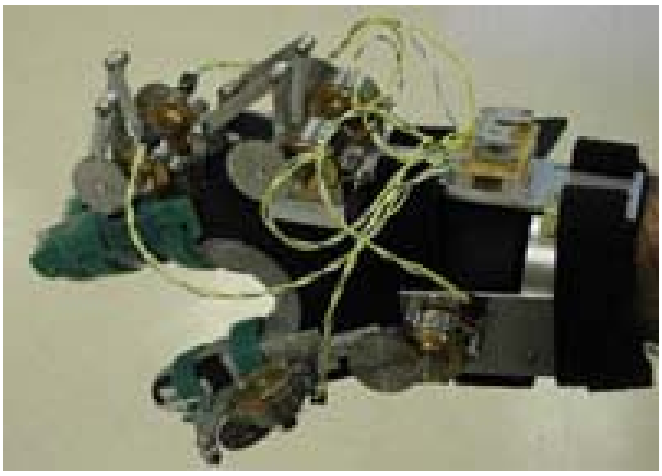

Figure 2.11 MR haptic glove.

A 2-DOF MR haptic display was designed by Junji Furusho's research group at Osaka University [47]. This system uses two groups of MR actuators to simulate virtual forces in two dimensions, respectively. There are two MR actuators and a DC servomotor in each group, and the mechanical structure combines forces from the two groups to execute the simulation in a two dimensional area. The maximum output torque is 10Nm in each dimension. The system is shown in Fig. 2.12.

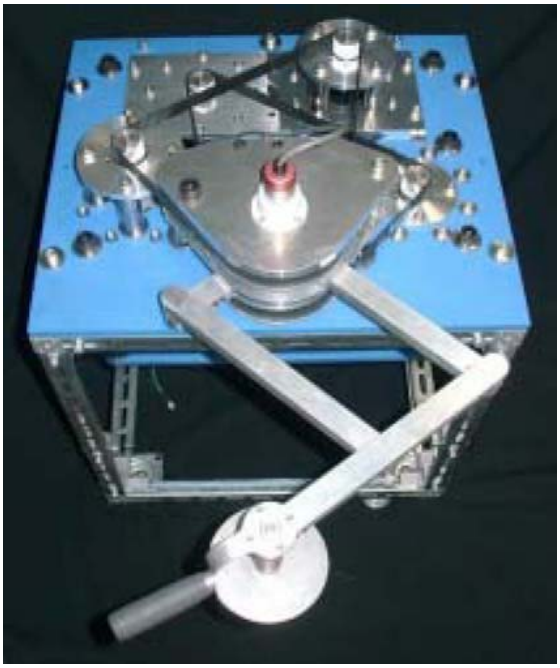

Figure 2.12 A 2-DOF MR haptic display.

## 2.5 CONCLUSIONS

In this chapter, MR technology was firstly introduced in terms of the mechanisms, materials, rheology, and devices. Then the two typical operating modes, shear-mode and flow-mode, were discussed, and MR devices based on the two modes were described. Prior to introducing ER and MR based haptic devices, the basic conceptions of VR and haptics were briefly discussed. The development of the MR haptic joystick in VR applications will be detailed in the next few chapters.

# CHAPTER 3
# SYSTEM OVERVIEW

## 3.1 WORKING PRINCIPLES

Haptic devices are very important components in virtual reality (VR) applications; therefore an effective haptic device with simple structure would simplify the control method and widen VR applications. Accuracy of torque control and position detection is the most crucial criterion for a haptic device. It is noted that conventional haptic devices are motor-based devices with the supporting mechanical structure providing force and torque to simulate the effect of VR. The kind of DC motor generally used can provide a fixed speed, which can be varied if a PWM (Pulse Width Modulation) controller is added [48]. Nevertheless, for a DC motor, it appears to be harder to control torque and position directly, unless some feedback is added. However, the output torque must be calculated by certain functions. Furthermore, the adoption of a feedback circuit increases the difficulty of the control procedure and causes instability in the control system. Since a DC motor is a speed-control device rather than force-control, it is hard for a traditional device to simulate accurately the forces of the virtual environment. The objective of this project is to overcome the distinct shortcomings of motor-based haptic devices by developing an MR fluid based haptic system.

The schematic MR joystick haptic system is shown in Fig. 3.1. It consists of four main components: an MR haptic joystick, a server computer, a data acquisition (DAQ) board, and a power amplifier.

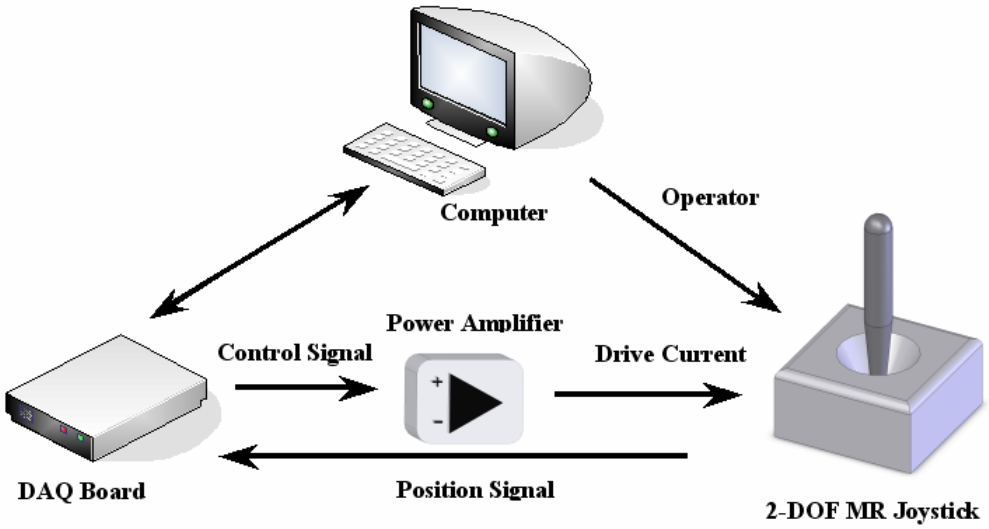


Figure 3.1 The MR Haptic System.

The central force performance part in this system is the 2-DOF MR haptic joystick, which allows the user to feel different resistant forces according to a virtual environment. The Computer performs as a control and display unit in this system. Firstly, for a 2D or 3D model, the VR environment needs to be designed and be input into the computer by the user. Then the computer generates force control signals according to the state of the environment, which corresponds to the virtual environment and the position of the joystick handle detected by the position sensors. When the user controls the object in VR by moving the joystick handle, the computer shows the updated picture to the user as a graphic feedback. The DAQ board is the information exchange platform between the computer and the joystick. It transfers the position signal, detected by the position sensor on the joystick, to the computer for force calculation and model resetting, and meanwhile sends the force control signal to the power amplifier to drive the MR joystick. The power amplifier is used to convert the voltage control signal into an amplified current driving signal, since the computer and the DAQ board cannot provide a current strong enough to drive the joystick directly. Consequently the operator can feel the different resistant forces when the operator moves the cursor, controlled by the joystick, through the images shown on the screen of the computer.

## 3.2 PROJECT TASKS

This project includes a number of tasks, as multiple techniques for controlling and manipulating MR fluids and mechanical design and software programming are involved in this project. To make interactions among the components of the system clear, the separate tasks are highlighted as follow:

**[1] Design, manufacturing and testing of MR actuators**

(1) Optimization of the actuator structure using Finite Element Analysis.

(2) Testing of steady-state performances of MR actuators.

(3) Modelling prediction of steady-state performances.

**[2] MR joystick development and analysis**

(1) Gimbal structure design.

(2) Joystick working space analysis.

(3) Joystick working space deformation.

(4) Force compensation modelling**.**

**[3] DAQ and power amplifier**

(1) Determination of a suitable DAQ board and designing of accessory equipment.

(2) Design of a power amplifier circuit for the joystick providing up to 2.2A current to drive the MR actuators.

**[4] Visual interface and application design**

(1) Design 1D visual interfaces for the MR actuator.

(2) Design 2D visual interfaces and control platforms for the MR haptic system.

(3) Design a 3D visual interface and control platform for the system.

## 3.3 OVERVIEW OF THE THESIS

Individual design and testing for different parts of the system will be described in the chapters following this system overview. Chapters 4, 5 and 6 will focus on the details of the MR haptic device. The electric circuit and software design will be represented respectively in Chapter 7 and Chapter 8. The main findings and recommendations will

be summarized in Chapter 9. The relationship between the different chapters is shown in Fig. 3.1, giving the readers an overview of the thesis.

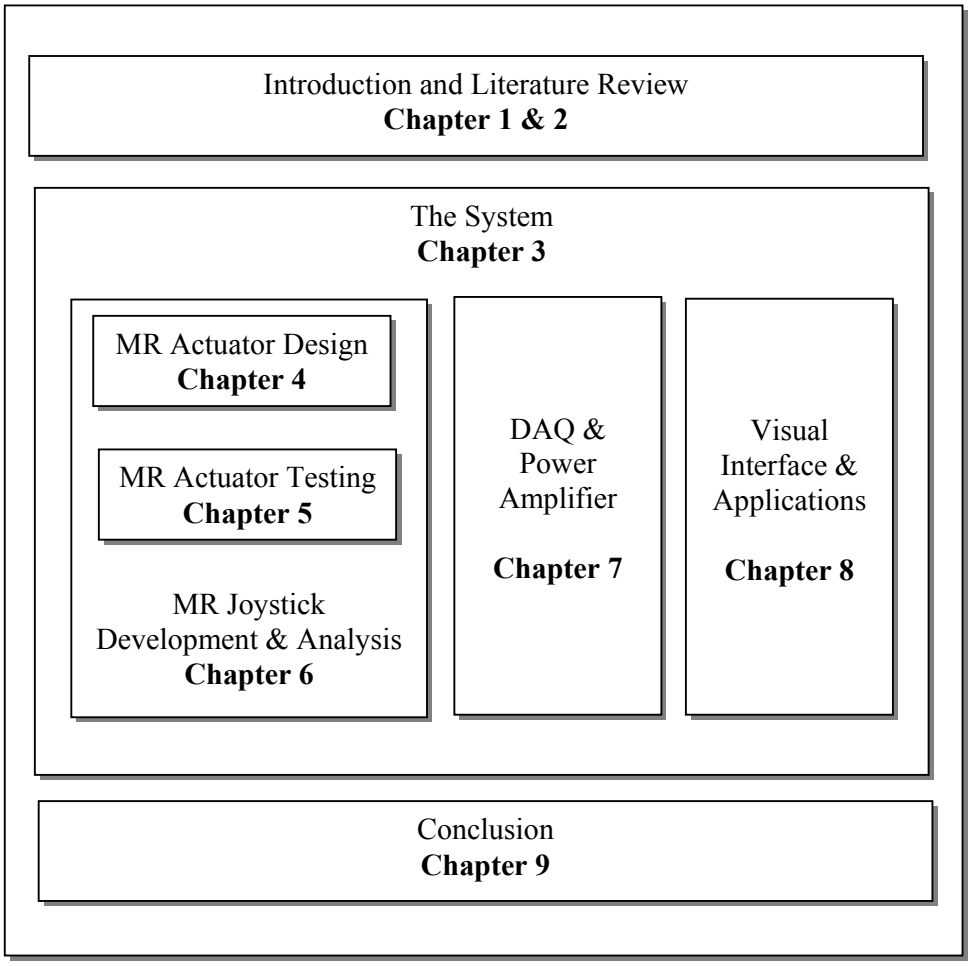


Figure 3.2 Relationships of the different chapters.

# CHAPTER 4
# MR ACTUATOR DESIGN AND MANUFACTURE

## 4.1 INTRODUCTION

This chapter presents the design and manufacture of the position-feedback MR actuator used as one of the resistant torque generators in the MR haptic joystick. The structure and the working principle of the MR actuator are first explained in the actuator design. Then the equation for transmitted torque is derived to evaluate the disc-shaped MR actuator. Finite element method (FEM) analysis is used to analyze the magnetic flux density distribution of the material and the structure of the MR actuator. This means that the design should maximize the magnetic field energy in the fluid gap, and at the same time, minimize the energy lost in the steel, the non-working MR fluid regions [49]. The design considers the difference between the magnetic saturation values of the fluid and the steel components. Magnetic saturation values, which are an inherent property of materials, can be found from their corresponding B-H curves. In order to optimize the response of the MR actuator, the magnetic induction value of the MR fluid and the steel should reach their saturation values at the same electric current. COSMOSEMS [50], a powerful electromagnetic analysis tool, was used to determine the dimensions of the different components of the MR actuator. The crucial manufacture details will be presented in the actuator design part at the end of this chapter.

## 4.2 DESIGN OF MR ACTUATORS

The concepts of accuracy, compactness, and manufacturability were taken into consideration in the actuator design. The main components of the position-feedback MR actuator include a compact shear disk MR actuator and a low resistance linear potentiometer, which is attached concentrically and can be rotated synchronously with the shaft of the actuator.

### 4.2.1 MR Actuator Structure

A side view of the position-feedback MR actuator is shown in Fig. 4.1. This actuator adopts a rotor that spins through a chamber filled with MR fluid. The magnetic field generated by the current flowing in the coil converts the fluid inside the chamber into a semi-solid, thus increasing the shear stress and torque required to turn the rotor. The actuator operates in a direct-shear mode as shown in Fig. 4.2, shearing the MR fluid contained in the space between the two surfaces, the disk surface and the plate, that move with respect to one another. MR fluid viscosity changes in the presence of a magnetic field excited around the coil as the result of the current flow. Resistance torque in the MR actuator depends mainly on the viscosity of the MR fluid.

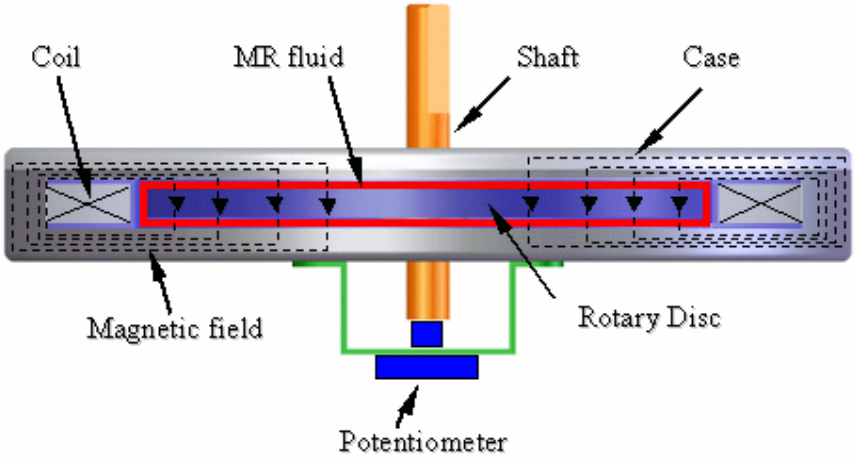


Figure 4.1 Side view of the position-feedback MR actuator.

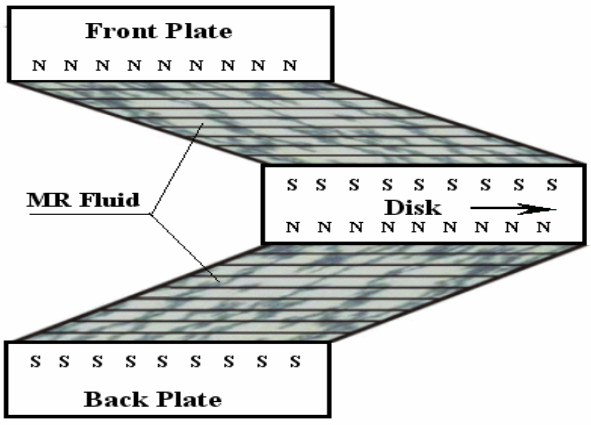


Figure 4.2 Shear Mode of MR fluid.

### 4.2.2 Static Performance Analysis of a Disc-shaped MR Actuator

The torque transmissibility of the MR actuator depends largely on the dynamic yield stress and the viscosity of the MR fluid [51]. Therefore, it is crucial to understand these MR fluid rheological properties under steady shear. The equation for transmitted torque is inferred from the Bingham plastic model. For a disc-shaped MR actuator, the constitutive equation is

$$\tau = \tau_y(H) + \eta_0 \frac{\omega r}{h} \tag{4.1}$$

where $\tau_y$ is the field-induced yield stress, $\omega$ is the angular velocity of the rotary disc, $h$ is the gap, and $r$ is the position on the disc surface as shown in Fig. 4.3.

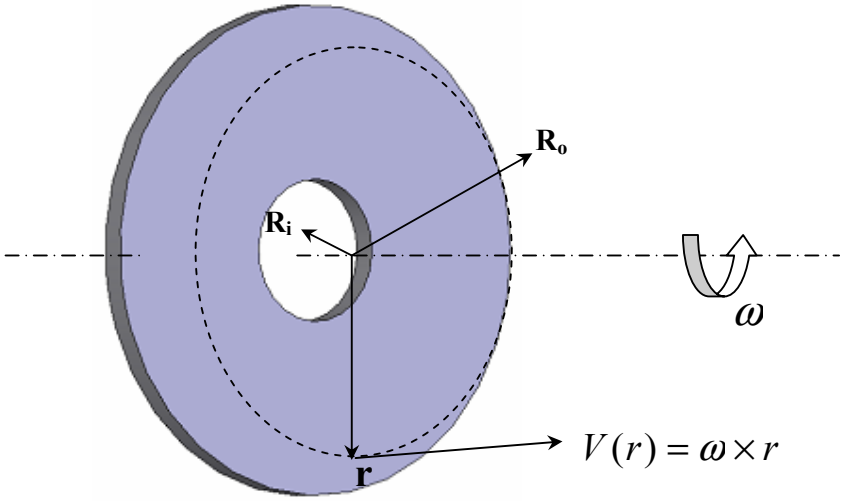


Figure 4.3 The working surface.

Since MR fluid behaves as described by the Bingham plastic property, the static yield stress can be obtained by extrapolating the shear rate to zero shear rate, i.e.

$$\tau \approx \tau_y \qquad (\omega \to 0) \tag{4.2}$$

Based on the static yield stress, the initial resistant torque can be calculated by

$$T = 2 \int_{r_{inner}}^{r_{outer}} (\tau_y \cdot dA) \cdot r \tag{4.3}$$

where $\tau_y$ is the yield stress of the MR fluid, A is the area of the circular disc, and r is the radius of the circular disc. To simplify the modelling and control of the MR actuator, all the parameters are chosen in the linear working area. MRF-132AD is the hydrocarbon based MR fluid that is used in this project. (The properties of the fluid are given in Appendix A.) From the data sheet for MRF-132AD, the top value of $\tau_y$ = 30kPa can be found in the linear area at the magnetic induction of H = 100kAmp/m as shown in Fig. 4.4.

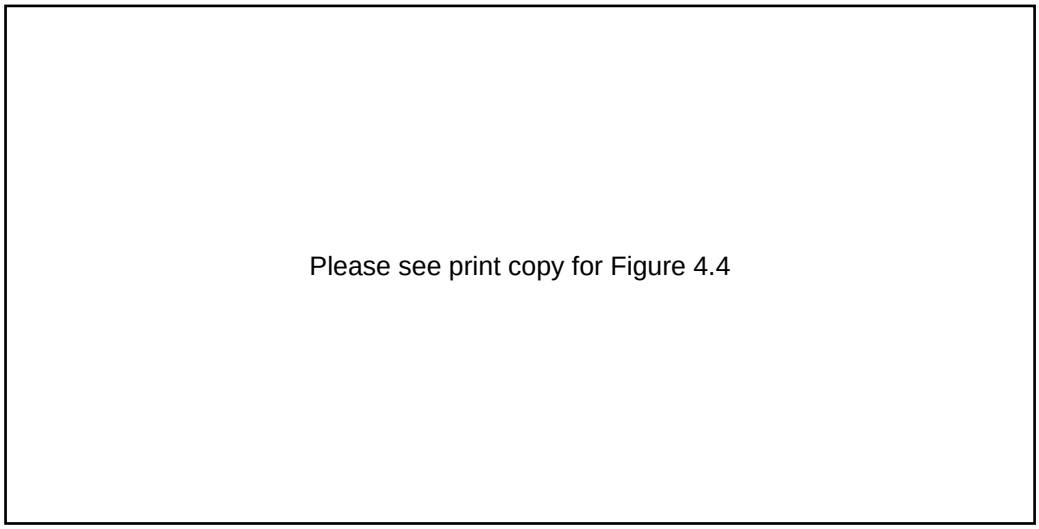


Figure 4.4 Yield stress versus magnetic induction curve [52].

The selected inner radius $r_{inner}$ = 4 mm is determined by the inner faces of the bearings. For the intended joystick VR application, the maximum resistant torque for a human palm was found to be T =15 Nm [53].

$$T = 2\int_{r_{inner}}^{r_{outer}} \left(\tau_y \cdot 2\pi r \cdot dr\right) \cdot r$$

$$T = \left[\frac{4\pi}{3} \cdot \tau_y \left(r_{outer}^3 - r_{inner}^3\right)\right]$$

$$15 = \left[ \frac{4\pi}{3} \times 30 \times 10^3 \left( r_{outer}^3 - 0.004^3 \right) \right]$$

$$r_{outer} \approx 50mm$$

Therefore, the calculated result for the outer radius is $r_{outer}$=50 mm.

### 4.2.3 Electromagnet Design

The dimension of the rotary disc has been calculated in the previous section. The design of the electromagnet coil, a vital component in the operation of the MR actuator, will be described here. The coil is to induce a magnetic field to produce the resisting action applied on the rotary disc. To understand the approximate behaviour of the magnetic circuit controlling the MR fluid, the fundamental laws of magnetostatics are applied. The parameters of magnetic field, the applied current, and the number of the coil turns is given by Ampere's Law [54]:

$$NI = \oint H \bullet dl = \sum_i H_i l_i = H_f L_g + H_s L_s \tag{4.4}$$

where N is the number of turns, I is the current in the coil, $H_f$ is the magnetic intensity, and $L_g$ is the width of the fluid gap. $H_s$ is the field in the steel and $L_s$ is the length of the steel path. Assuming no magnetic leakage, the magnetic induction is constant, so the relation between the field and the magnetic induction intensity B can be calculated by

$$B = \mu_o \mu_r H = \frac{\Phi}{A} \tag{4.5}$$

where $\mu_o$ is the permeability of free space with a constant value of $4\pi \times 10^{-7}$ H/m. $\mu_r$ is the relative permeability of different materials. $\Phi$ is the magnetic flux, and A is the effective area. So the coil can be designed based on the following equation:

$$NI = \frac{B_f L_g}{\mu_0 \mu_f} + \frac{B_s L_s}{\mu_0 \mu_s} \tag{4.6}$$

where $\mu_f$ and $\mu_s$ represent the relative permeability of MR fluids and that of mild steel, respectively. A schematic of the magnetic circuitry for an MR fluid can be demonstrated by the C-shaped model shown in Fig. 4.5.

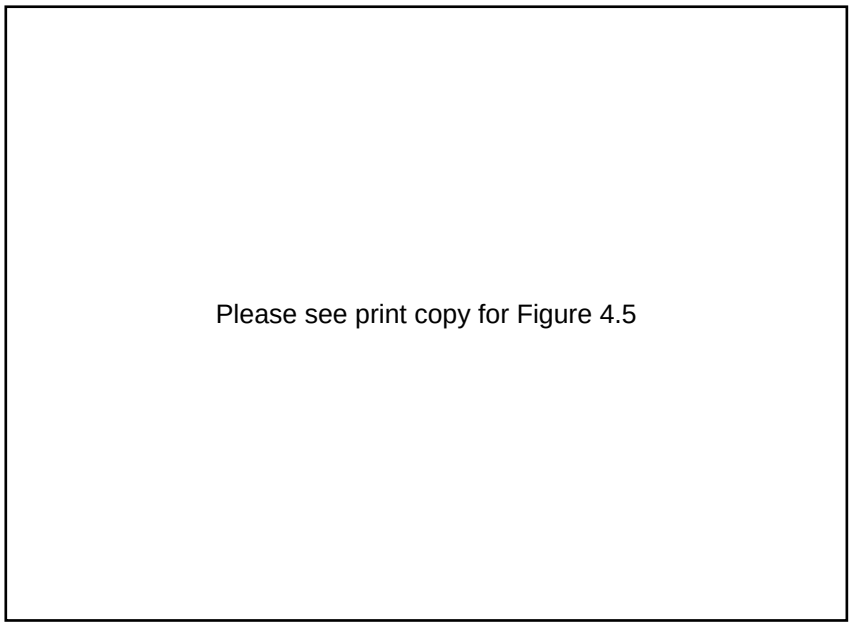


Figure 4.5 Schematic of the Magnetic Circuitry [55].

The picture shows that $\Phi_s = \Phi_f$, $A_S \approx A_f$. Because $\mu_{f} << \mu_{s,}$ the second part of Eq. 4.6 can be ignored, hence the equation can be reduced to:

$$NI = \frac{B_f L_g}{\mu_0 \mu_f} = H_f L_g \tag{4.7}$$

To make the MR fluid work in the linear area, the maximum effective yield stress is chosen as 30 kPa from Fig. 4.4, which was taken from the data sheet of the MR fluid used. The magnetic induction obtained from the graph is 100kAmp/m, according to the working yield stress 30kPa. The MR fluid gap is 1mm on each side, hence the total gap length is $L_g$=2 mm. Based on Eq. 4.7, the value of NI can be derived:

$$NI = H_f \times L_g$$

$$NI = \left(100 \times 10^3\right) \times \left(2 \times 0.001\right)$$

$$NI = 200$$

Therefore, the number of turns inside the electromagnetic holder times the current passed through the electromagnet must be greater than 200. This number is used in the design of the coil holder and in the testing to refine the function of the MR actuator.

### 4.2.4 Finite Element Analysis of MR Actuator

The finite element analysis method (FEM) was adopted to find the optimal structure and dimensions of different components of the actuator. The MR actuator can work more effectively and the electrical energy can be efficiently used in the working area of the MR fluid with an optimized structure. Furthermore, the approximate analytical solution calculated in the previous section only provides fundamental parameters for the actuator structure design. To obtain an effective structure and an accurate distribution of magnetic field, the SolidWorks and COSMOSEMS packages [56] were combined to build the 3D model and to simulate the magnetic distribution with FEM. SolidWorks is a 3D solid modelling CAD package. The innovative feature-based parametric design method of SolidWorks offers the most time-saving capabilities for the user and reduces the design cost of the products. COSMOSEMS is a member of the COSMOSWorks family, which is intended for designers and engineers who are not specialists in design validation. COSMOSWorks helps by allowing the simulating behaviour of SolidWorks models to be studied via FEM before the designs are built.

#### 4.2.4.1 Magnetic properties of MR fluid and mild steel

In an isotropic medium, the magnetic flux density shows a nonlinear relationship with the applied magnetic induction. However, a linear behaviour exists under low magnetic field conditions, i.e. below the magnetic saturation field of the magnetic materials. That is, the flux density cannot increase infinitely when the applied magnetic field is above the saturation point. Therefore, magnetic saturation of the mild steel [53] and the MR fluids should be taken into consideration in the design and analysis of MR actuators.

A B-H curve is used to illustrate the effect of magnetic saturation. The magnetic field, H**,** tends to magnetize space, and the magnetic flux density, B, is the total resultant magnetic effect. The magnetic B-H curves of the MR fluid and the mild steel are shown in Fig. 4.6 (a) and (b).

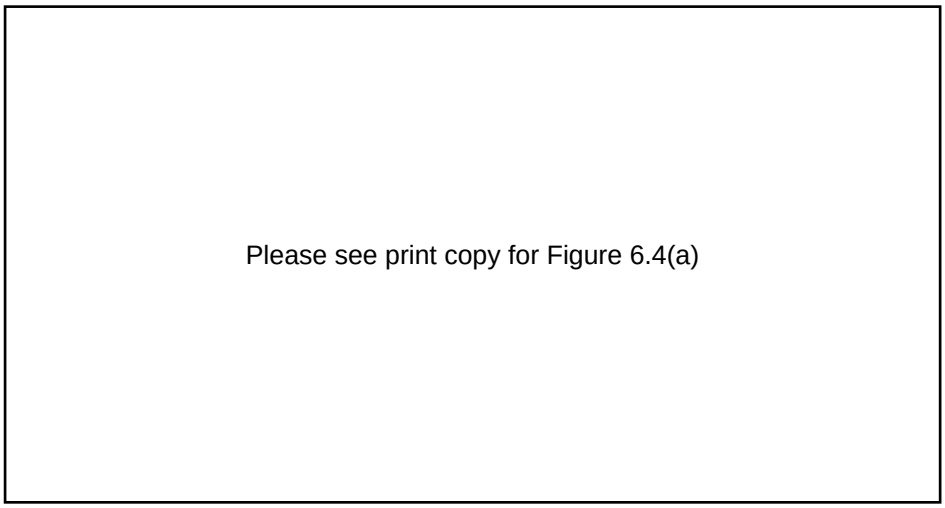


(a) MR fluid B-H curve [52].

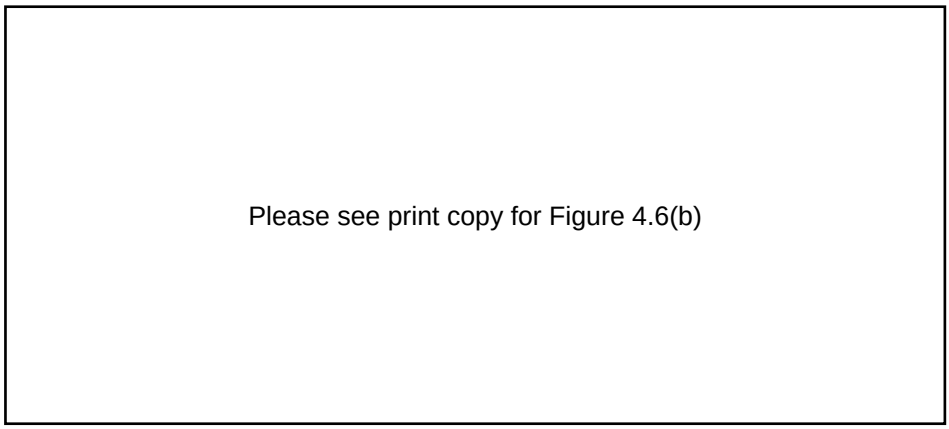


(b) Mild steel B-H curve [57].

Figure 4.6 Magnetic properties of the MR Fluid and the mild steel.

The optimal points, where the slope of the B-H curve changes for the MR fluid (Hs, Bs) and the mild steel (Hf, Bf), are marked in the figures. The values of the optimal points are given in Table 4.1.

| Item | MRF-132AD | Mild steel |
|---|---|---|
| $\mu_r$ | 5 | 1000 |
| Hf or Hs | 130 KA/m | 700 A/m |
| Bf or Bs | 0.6 T | 1.4 T |

Table 4.1 Optimal magnetic performance characteristics.

#### 4.2.4.2 3D magnetic field finite element analysis

Considering the intensity and required non-magnetic characteristics of some of the actuator components, copper was adopted as the material for the shaft and aluminium for the coil holder and frame where the potentiometer is fixed. All the other components of the actuator are made of mild steel, which is strong enough to support the whole structure of the actuator and can be magnetized as well. Due to the symmetrical structure of the actuator, a quarter-disc model was used to simulate the magnetic flux density distribution. The 3D model with dimensions is shown in Fig. 4.7(a). The top view and the side view of the simulation are given in Fig. 4.7 (b) and (c), respectively.

All the dimensions and other parameters of the MR actuator were determined with respect to the outer radius of the disc ( $r_{outer}$ =50 mm). The optimal parameters, listed in Table 2, were derived by a series of successive trials.

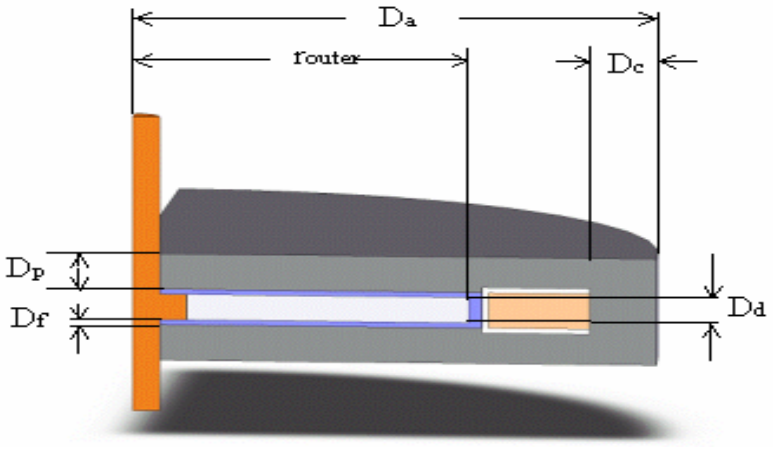


( a ) 3D model of the MR actuator.

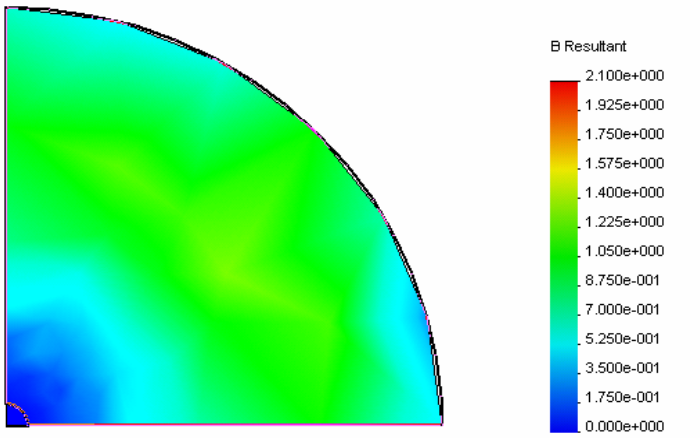


( b ) Top view of the FEM simulation.

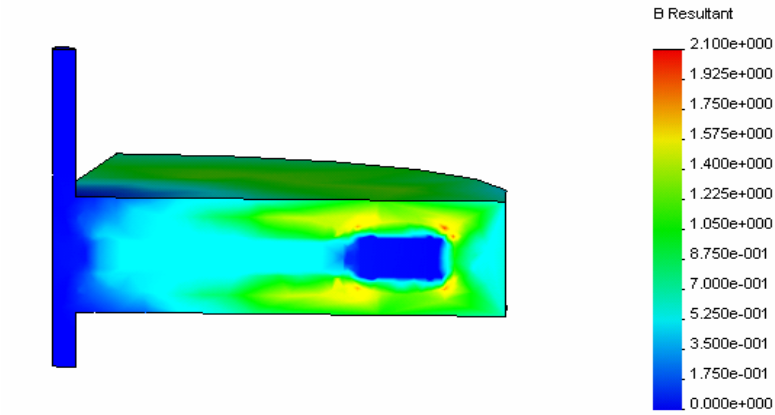


(c) Side view of the FEM simulation.

Figure 4.7 3D FEM magnetic field simulation.

| Symbol | Note | Value |
|---|---|---|
| $r_{outer}$ | Outer radius of the disc | 50 mm |
| Da | Radius of MR actuator | 78 mm |
| Dc | Thickness of the case | 10 mm |
| Dd | Thickness of the disc | 5 mm |
| Df | Thickness of MRF gap | 1 mm |
| Dp | Thickness of the plate | 7 mm |
| N | Turns of the coil | 100 |

Table 4.2 MR actuator parameter list.

Fig. 4.7(b) shows that the distribution of the magnetic flux density is approximately constant in the MRF shear area. The MRF and the mild steel plate reach their saturation values (0.6T and 1.4T, respectively) under the same electric current of 3A. As a result, the magnetic energy translated from the electric energy can maximally contribute to the yield stress of the MR fluids. Fig. 4.8 shows the distribution of the magnetic flux density in MR fluids in the condition of different electric currents. The sample values were chosen along the radial direction. It is conspicuous that the flux density changes proportionally in correspondence to the electric current. The distribution of the magnetic flux density appears independent of the distance from the shaft, except for the end, which is close to the coil. The greater flux density near the plate edge is caused by the edge effect of the magnetic field and the higher magnetic induction closer to the coil.

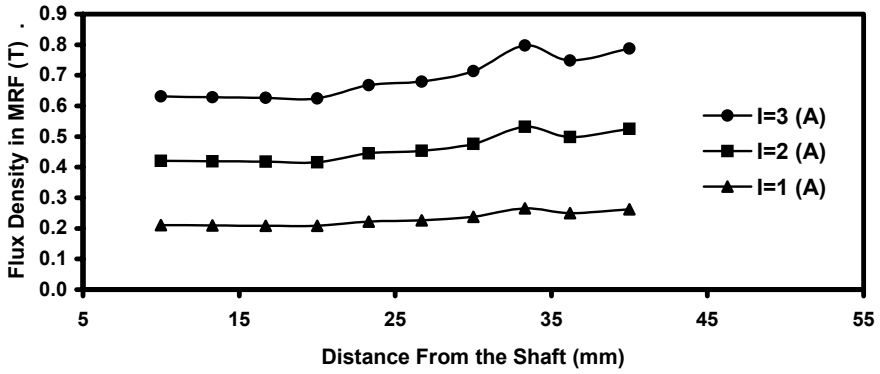


Figure 4.8 Magnetic flux density distribution.

## 4.3 MANUFACTURING OF AN MR ACTUATOR

Each compact MR actuator includes eight components marked from N1 to N8, as shown in Fig. 4.9 (a) and (b). Except for the sealed bearings, all the other components were designed in SolidWorks, which can easily project a 3D model into different views such as exploded views, section views, and assemblies for manufacture. The working principle of the actuator has been described in the previous section. This section focuses on the details of structure, materials, manufacture, and assembly of the components.

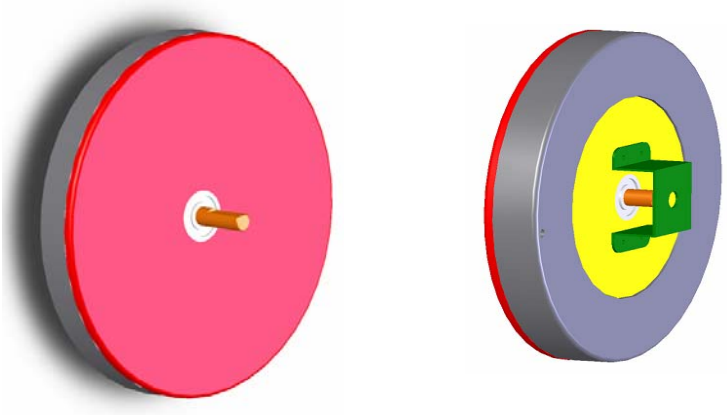

(a) Assembled MR actuator.

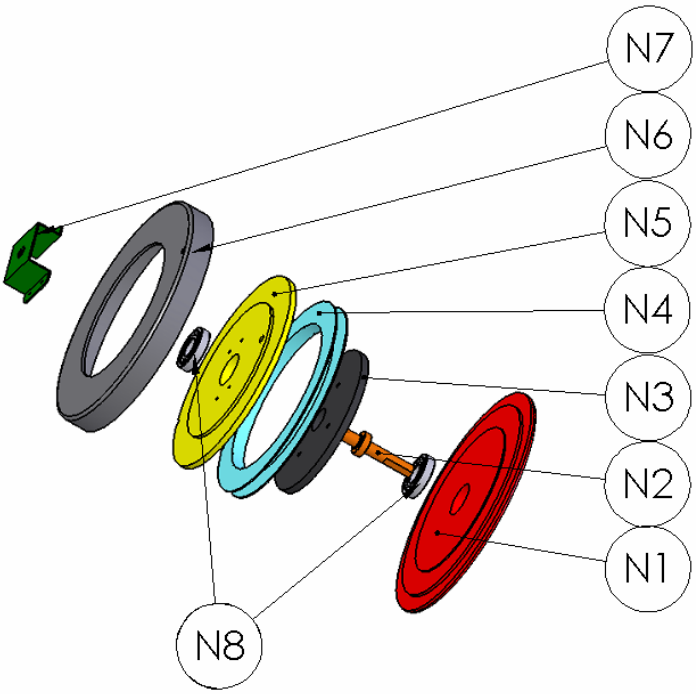


N1: Top plate

N2: Shaft

N3: Rotary disc

N4: Coil holder

N5: Bottom plate

N6: Outer casing

N7: Shelf

N8: Sealed bearing

(b) Exploded view of the MR actuator.

Figure 4.9 The MR actuator.

### 4.3.1 Material And Magnetic Circuit

All the components forming the magnetic circuit were made from mild steel. These components include the top plate (N1), rotary disc (N3), bottom plate (N5), and outer casing (N6) shown as the grey parts in Fig. 4.10. Copper was used to fabricate the shaft (N2) because of its low magnetic permeability and high strength properties. The

magnetic permeability of mild steel is much higher than that of air and copper, as shown in the picture; the uniform magnetic field is formed in the MR fluid area to change the stiffness of this fluid.

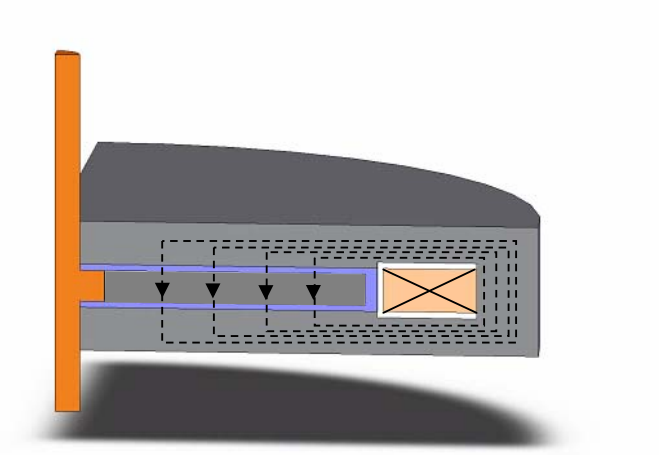

Figure 4.10 Magnetic circuit of the MR actuator.

The coil holder (N4) and the shelf (N7) were made from aluminium. The coil holder was used to hold the coil and functions as the circular wall of the chamber containing the MR fluid and rotary disc. The shelf was used to fix the potentiometer to detect the position of the rotary disc. The potentiometer used in this project is the low resistance linear type, so the torque applied on the shelf by the potentiometer is very weak. The suitable strength and the low density of the aluminium made it an appropriate material for the fabrication of the coil holder and shelf.

### 4.3.2 Structure and Assembly

The structures of the components were designed to be as simple as possible for manufacturing and assembly purposes, but there are still some vital details that need to be described for a comprehensive understanding and to allow further improvement on the current design. The order of assembly of the components is crucial, since there are several push fit tolerances between the components and the MR fluid could easily flow into the assembled actuator.

The shaft (N2) is the essential part that converts the shear force of the MR fluid into the output resistant torque. The shaft was fixed with press fit tolerance to the rotary disc. This was the first step in the assembly of the MR actuator. To locate the two sealed bearings, two steps were designed on each side of the platform with a thickness of 1mm, which was the thickness of the MR fluid. The flat segment at the right end of the shaft was used to fit the coupling, the design of which is described in a later chapter. The hole at the bottom end of the shaft was used to link the shaft with the potentiometer, which could be installed onto the shaft after all the components were assembled.

The rotary disc (N3) was press fit with the shaft and shears the MR fluid when rotated together with the shaft. This was the second step in the assembling process. The bearing selection for the MR actuator is critical for the overall operation of the MR actuator. The bearing selected needs to have a low coefficient of friction and also has to prevent the leakage of MR fluid from the MR actuator. The single row deep groove ball bearing 608-2RSH, which has double-sided full contact seals, was chosen to fulfil the rigorous requirements of this project. The seals were inserted in recesses in the outer ring and provide good sealing at this position without deforming the outer ring. The four holes in the disc allow the MR fluid to flow easily from one side to the other of the disc when the MR fluid is infused into the actuator from the filling hole in the bottom plate (N5). The diameter and the thickness of the disc were calculated by the finite element method (FEM) in the previous section.

The third step was the top plate (N1) installation. The top plate was designed for three functions: to cover the outer casing, to fix the coil holder, and to form the top wall of the MRF chamber. So, two steps were designed in it to form three surface levels on the inner side of the front plate. The maximum thickness of 7mm in the central part of the front plate was determined by the thickness of the bearing, and the diameter of the central hole was chosen as 22mm to fit the outer ring of the sealed bearing. The inner annulus was used to hold the MR fluid in the chamber. The middle annulus was used to fix the coil holder; so the width of this section was equal to the width of the coil holder.

The installation of the coil holder (N4) was the fourth step in the assembly. The holder was manufactured from an aluminum sheet with a thickness of 1mm. The value of the inner radius was 52mm, which was based on the 50mm radius of the rotary disc plus a

2mm gap. The total thickness of the coil holder was 7mm, sufficient to hold the 5mm disc and to leave a 1mm MR gap on each side of the disc. The outer radius was decided by the value of NI=200 calculated before. The maximum working electric current was chosen as I=2A, so the number of the turns was 100. To make the actuator work in a stable condition for a long period, the diameter of the coil wire was chosen as 0.8mm, which is thick enough for a 2A drive current. Finally, the 68mm radius was designed to leave enough space for an N=100 coil. To avoid leakage of the MR fluid, the flange sealant LOCTITE 515, which can hold a working pressure of 690 kPa, was smeared between the middle annulus surface and the side surface of the coil holder.

The bottom plate (N5) was next installed as the bottom of the MR fluid chamber and also was used to fix the shelf (N7) for the potentiometer. One side of the bottom plate was mounted into the outer casing (N6), and the other side was attached to the coil holder with sealant. The MR fluid could be infused into the actuator chamber through the two M4 threaded holes after all the components were assembled. The four M2 holes were drilled to fix the shelf.

The last component for the assembly was the outer casing (N6). The outer casing protects the coil and the rotary disc, and the cylinder wall of the casing forms part of the magnetic circuit, in combination with the top plate, the rotary disc, and the bottom plate. The hole at the top-left corner of the casing is the wire hole, which was drilled through from the coil holder and the bottom plate. The coil wire can be threaded through this hole, but the MR fluid remains sealed in the actuator. The four M4 threaded holes on the front side were used to fix the top plate, and the other three clear holes on the backside of the casing formed a fixing structure, by which the MR actuator could be fixed on the joystick. All the components and the assembled actuator are shown in Fig. 4.11 below:

**N(1)**

**N(2), N(3) and N(5)**

**N(4)**

**N(6)**

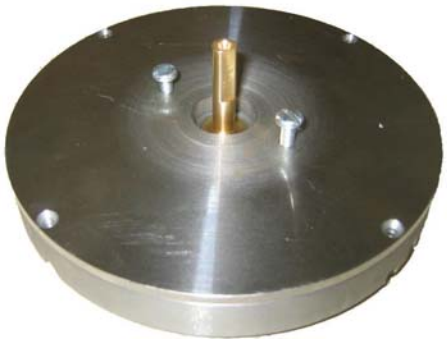

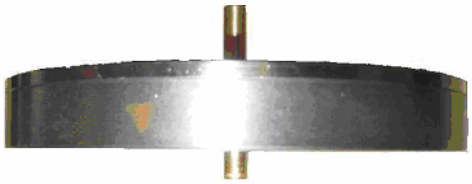

Figure 4.11 The MR actuator.

# CHAPTER 5
# TESTING AND MODELLING OF THE MR ACTUATOR

## 5.1 INTRODUCTION

The design and the fabrication of the MR actuator have been discussed in the previous chapter. Following the manufacturing and assembling of a brake prototype, the mechanical performance of the MR actuator was experimentally assessed by a specifically designed testing procedure. Then a parametric sub-hysteresis model is proposed based on the performance of clockwise/counter-clockwise rotary testing to simplify the control method and to predict the resistant torque accurately. This model was then used in the joystick haptic control system, making the MR joystick simulate a precise resultant force for virtual reality (VR) applications. The comparison between the test results and the results predicted by the model is analysed at the end of this chapter.

## 5.2 STATIC TESTING

This section describes the results of a series of tests based on a low speed haptic application, all of which were performed in the condition of a low and steady rotation rate using an IMADA Model HTG2-85 digital torque gauge as shown in Fig. 5.1. The HTG2-85 is a torque tester that has a Real Time mode to display torque transients and a Peak mode to capture the peak torque achieved during a test. The testing range of this gauge is 0-1000 Ncm with a resolution of 1 Ncm. The torque testing performed in this chapter was designed according to the needs of the VR applications, with low-speed and reciprocating rotation induced on the two MR actuators by the joystick.

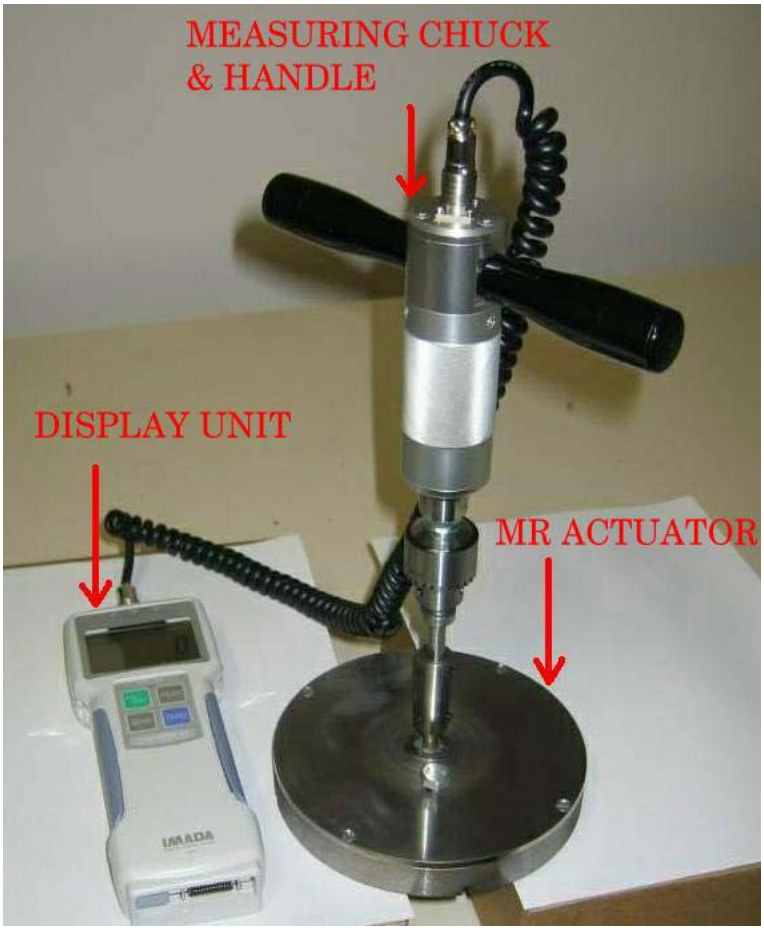


Figure 5.1 Static testing.

### 5.2.1 Clockwise/counter-clockwise Testing

The MR actuator was designed as one of the resistant torque generators in a haptic MR joystick. When the handle of the joystick moves arbitrarily in a 2D area, the disk of the actuators performs a clockwise/counter-clockwise rotation. The clockwise/counter-clockwise testing was designed to find the characteristics of the torque performance under this motion behaviour.

Based on the obtained optimum geometrical dimensions, static testing and modelling of the actuator were subsequently carried out. Because MR actuators, unlike conventional actuators, behave in a non-linear fashion and are more difficult to model than traditional actuators [58], a parametric model was used to predict the performance of the device

and to develop control strategies. A parametric sub-hysteresis model was derived from the clockwise/counter-clockwise testing to predict the experimental results.

The outcomes of the clockwise/counter-clockwise tests are shown in Fig. 5.2. For each direction of rotation, two static behaviour tests were conducted with two different electric current sequential changes: 0-1-0 A and 0-2-0 A. The results of the clockwise and counter-clockwise tests are drawn side by side in the figure. The negative signs on the left side represent the opposite direction of rotation instead of a negative electric current. The torque curves on both sides show a symmetrical feature in the two opposite rotations. It was found that the static behaviour of the actuator was not influenced by the direction of the shaft rotation. This characteristic simplified further testing and modelling on the static behavior of the MR actuator.

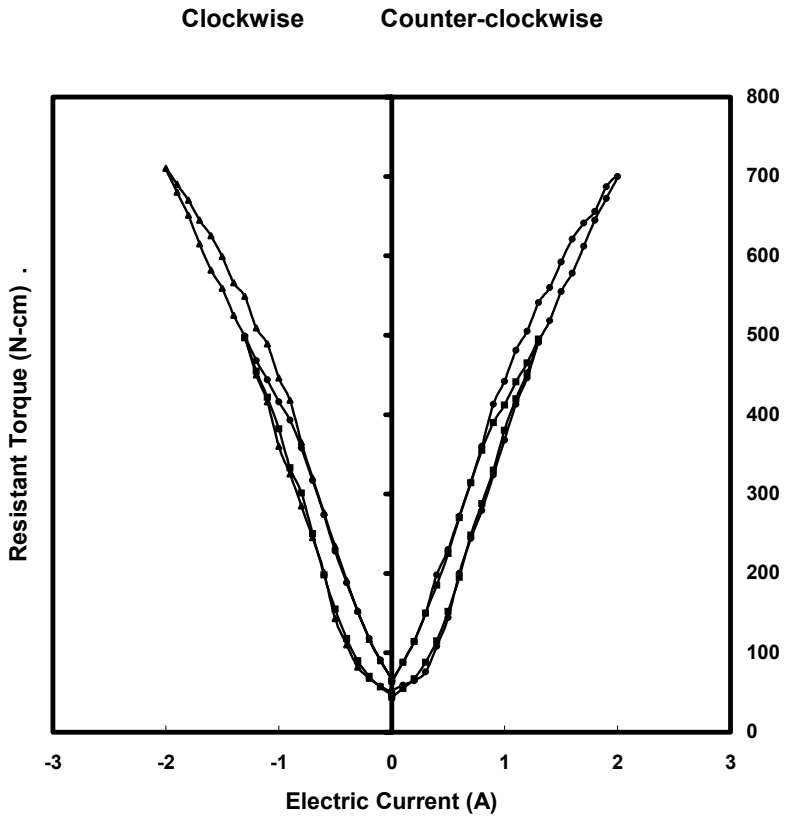


Figure 5.2 Results of clockwise/counter-clockwise tests.

### 5.2.2 Sub-hysteresis Testing and Modelling

Based on the conclusion of the clockwise/counter-clockwise testing, only one direction was chosen to perform further static testing by reciprocating rotational experiments. More detailed and complicated tests were performed under varied electric current conditions: 0-0.5-0A, 0-1-0A, 0-3-0A, and 0-2-1-2A. The results are given below in Fig. 5.3.

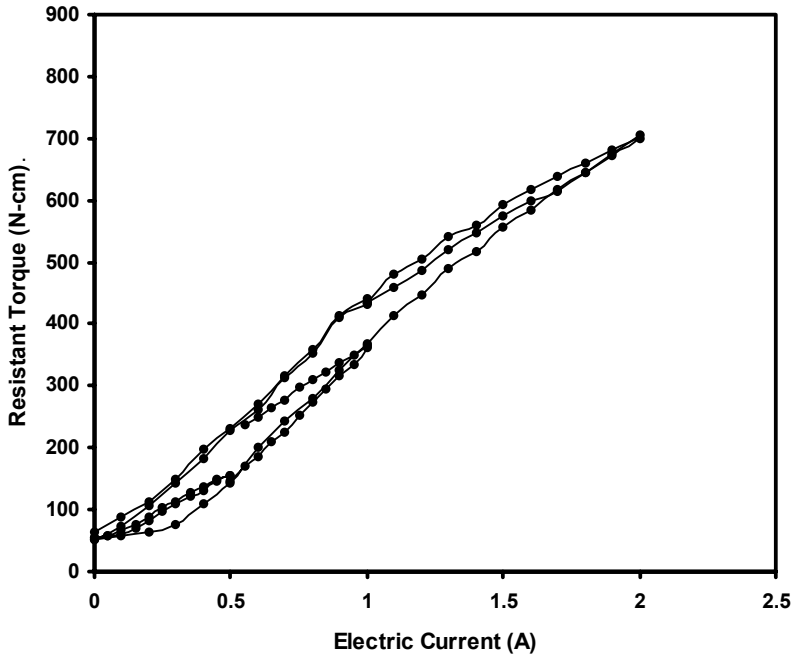


Figure 5.3 Sub-hysteresis testing of MR actuator.

When a ferromagnetic material is magnetized in one direction, it will not relax back to zero magnetization when the imposed magnetizing field is removed. It must be driven back to zero by a field in the opposite direction [59]. This phenomenon is called hysteresis. The behavior of the MR actuator shows a series of hysteresis loops that are limited by the largest loop boundary. Here the largest boundary hysteresis is called the main hysteresis. In a hysteresis loop, each loop represents torque that corresponds to two different electric currents. The difference between the two electric currents is called electric current shift. Investigation of the static characteristic indicated that the MR actuator had sub-hysteretic behaviors. Based on the following three assumptions, the conception of sub-hysteresis was proposed to model the actuator hysteretic behaviors: (a) all the sub-hysteresis is limited to the main hysteresis domain; (b) all the electric

current shifts of the sub-hysteresis loops are constant and equal to the electric shift of the main hysteresis; and (c) the top slopes of the sub-hysteresis loops are constant in the linear area. In terms of these assumptions, a sub-hysteresis model was constructed and the concept is shown in Fig. 5.4.

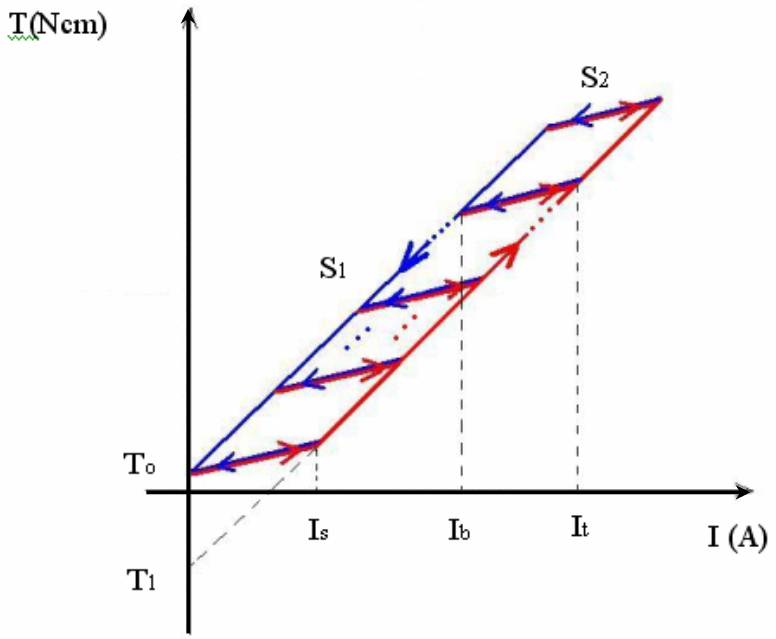


Figure 5.4 Sub-hysteresis model.

The red arrows are the paths of the resistant torque when electric current increases. The blue arrows indicate the paths of the resistant torque when electric current decreases. These paths and the superimposed red and blue paths form the sub-hysteresis model combining with the pure red and blue paths. In this model, $T_0$ is the resistant torque exhibited in the absence of electric current; $I_s$ is the constant difference in the electric current; $S_1$ and $S_2$ are the two constant slopes of $T$ in the model; $I_t$ and $I_b$ are the two vertices of a sub-hysteresis loop and their values can be changed when the torque moves along the red or blue arrow.

The resistant torque can be calculated according to the input electric current based on this sub-hysteresis model. The program model of the sub-hysteresis behavior contains three modules as shown in Table 5.1:

| | | |
|---|---|---|
| Initialization Module | $I_0 \le I_s$ | $I_b = 0;\ I_t = I_s;$ $T = S_2\ I_0 + T_0$ |
| | $I_0 > I_s$ | $I_b = I_0 - I_s;\ I_t = I_0;$ $T = S_1\ I_0 + T_1$ |

| | | | |
|---|---|---|---|
| Step 1 | $I_t - I \ge I_s$ | | Dec=1; Inc=0 |
| | $0 < I_b - I < I_s$ or $0 < I - I_t < I_s$ | | Dec=0; Inc=0 |
| | $I - I_b \ge I_s$ | | Dec=0; Inc=1 |

| | | | |
|---|---|---|---|
| Step 2 | $\dot{I} > 0$ | Inc=1 | $I_t = I;\ I_b = I - I_s;\ T = S_1\ I + T_1$ |
| | | Inc=0 | $T = S_1\ I_b + T_0 + S_2\ (I - I_b)$ |
| | $\dot{I} < 0$ | Dec=1 | $I_b = I;\ I_t = I + I_s;\ T = S_1\ I + T_0$ |
| | | Dec=0 | $T = S_1\ I_t + T_1 + S_2\ (I - I_t)$ |
| | $\dot{I} = 0$ | | $T = T$ |

Table 5.1 Program model of the sub-hysteresis behavior.

The left section in each module is the name of the module. A double-line separates the logical area into two sections: the sections on the left side are the conditions, and the right sections are the output results that are used as the initial conditions for the next iteration. $\dot{I}$=dI/dt, and $\dot{I}>0$ means that the electric current is increasing. Dec=1 means that the torque track is on the pure blue arrow; Inc=1 means that the torque track is on the pure red arrow; Dec=0 and Inc=0 means the torque track is in the middle of the main hysteresis loop. In other words, it is on the mixed color paths. The diagram of the program model adopts a loop structure as shown in Fig. 5.5. The program will first

determine the initial resistance torque of the actuator following the rules described in the initialization module and then apply these rules in Step 1 to determine the path followed by the current change. Step 2 gives the equations to calculate torque for each path. The loop is repeated upon further current change.

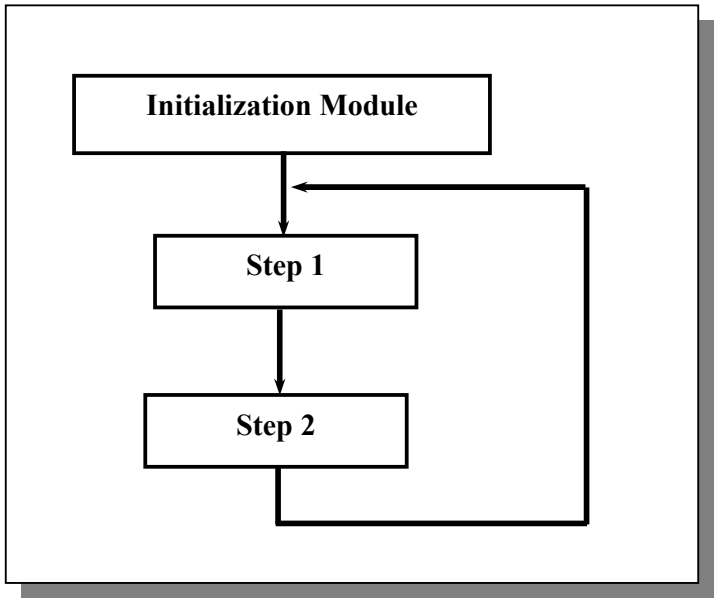


Figure 5.5 Diagram of the iterative sub-hysteresis model.

It can be inferred that an MR actuator is characterized by four constants, namely, $I_s$, $S_1$, $S_2$, and $T_0$. In terms of the results of the experiments, the values of these parameters were identified as $I_s$=0.6, $S_1$=387.5, $S_2$=233.3, and $T_0$=45. The torque prediction results programmed by MATLAB are shown in Fig. 5.6(a). A comparison of the experimental results and the program predictions is shown in Fig. 5.6(b), in which the program was able to predict the output resistant torque within 5% error. (The initial electric current increase from 0 to 0.6A was not expressed in this model.) The MATLAB m-file programming is attached in Appendix B.

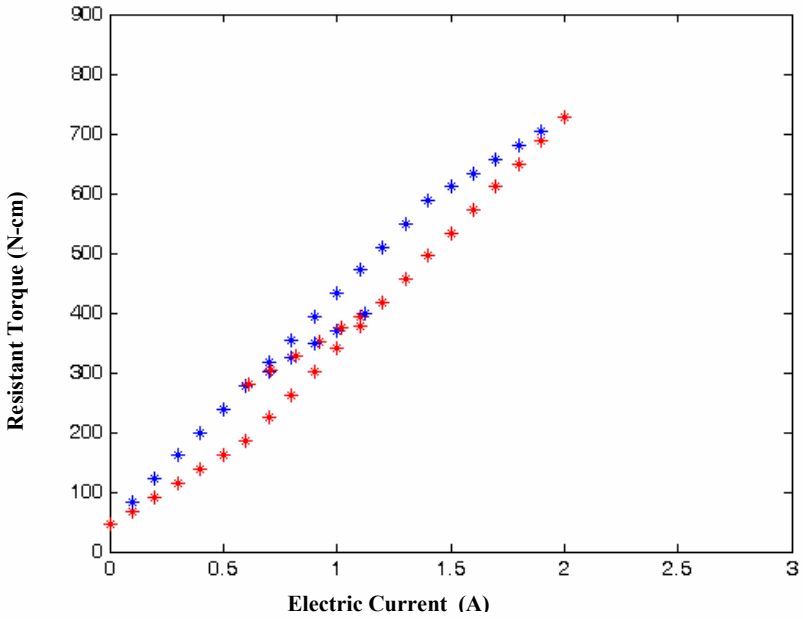


(a) Prediction of the sub-hysteresis model.

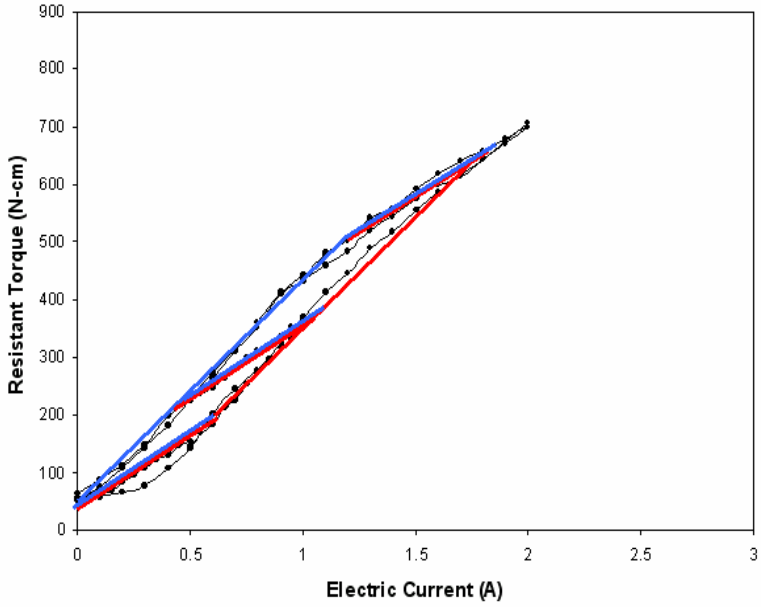


(b) The comparison of the experiment and the prediction.

Figure 5.6 The sub-hysteresis model prediction.

This model can be used to predict the output torques with any initial current within a working range from 0 to 3A. The continuous variable torques caused by a variety of control currents can also be predicted from the influence of the hysteresis property.

# CHAPTER 6
# MR JOYSTICK DESIGN AND ANALYSIS

## 6.1 INTRODUCTION

The design and analysis of the MR haptic joystick will be described in this chapter. The position feedback MR actuators have been assembled and tested in the last chapter, so the task of this section is to fabricate an MR haptic joystick by using the two MR actuators as the force generator. The central gimbal structure will be presented in the mechanical design of the joystick. In the static torque analysis, the torque composition and working surface deformation will be presented according to the geometrical structure of the joystick. Following the force analysis, a pseudo 3D analysis will be demonstrated to meet the requirements of 3D virtual reality (VR) applications.

## 6.2 OVERVIEW OF THE MR JOYSTICK

The 2-DOF MR joystick plays an important role in this haptic system. The two MR actuators get the control signal amplified by the power amplifier and perform resistant torques in each direction individually. The MR joystick uses the MR actuators and the gimbal structure to achieve virtual force simulation in a 2D area. With the help of special control strategies, this 2-DOF system can carry out a pseudo 3D simulation. The main components of the joystick are two MR disc-shaped actuators, a gimbal structure, a handle and the frames of the joystick. A schematic diagram of the 2-DOF MR joystick is shown in Fig. 6.1.

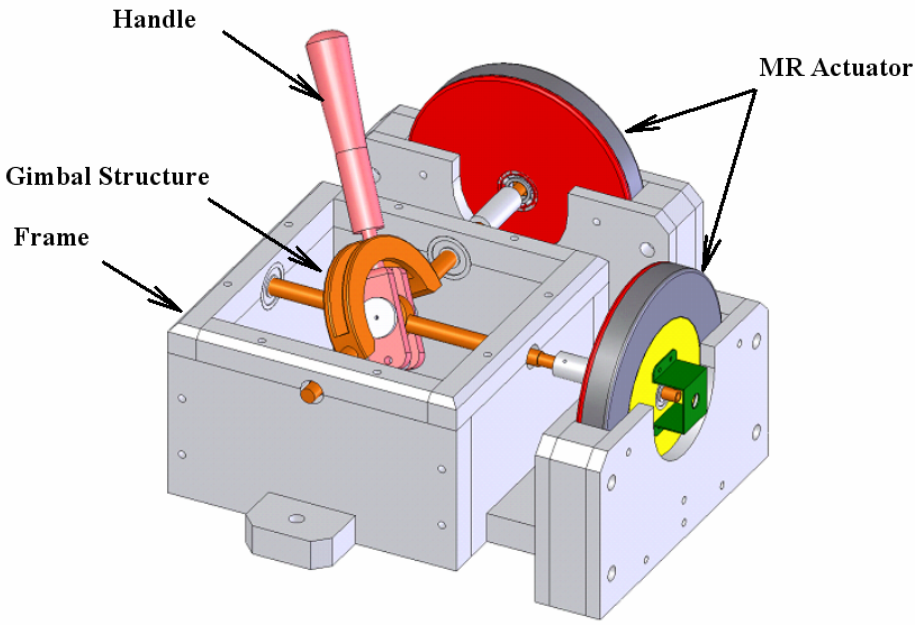


(a) The 3D view of the joystick

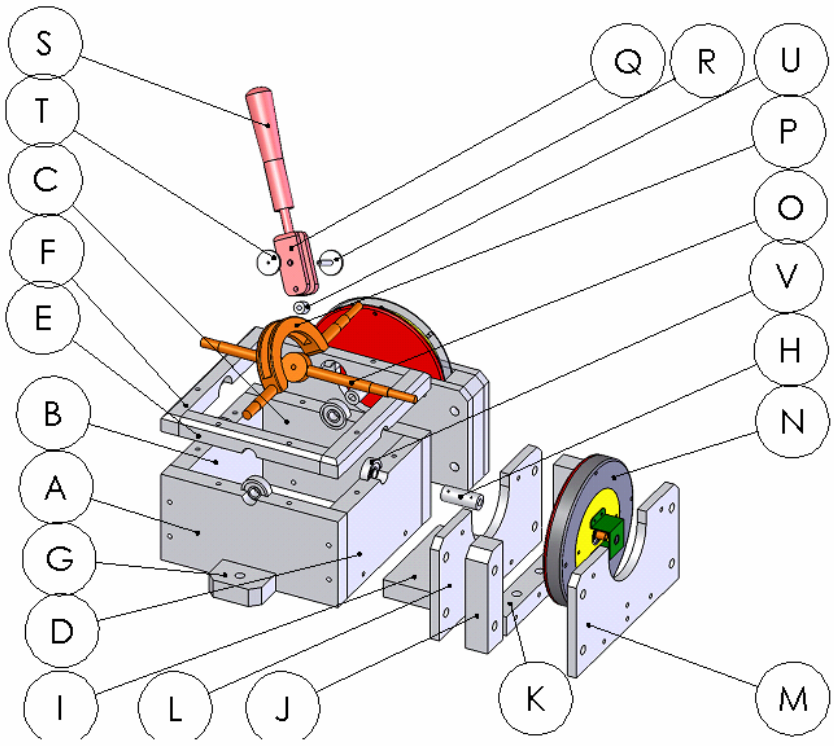


(b) An exploded view of the joystick

Figure 6.1 2-DOF MR haptic joystick.

The two MR actuators are the torque generation elements, which are set orthogonally and connected to the shafts of the gimbal mechanism, which is fixed in a square frame by bearings. Each one can be used to detect the one-dimensional position of the handle by means of a linear potentiometer attached to the shaft of the MR actuator, and generates resistance in the same direction according to the control current generated from the computer. The gimbal structure, made of standard steel, enables the user to feel a resistant force in a two-dimensional area through the handle of the joystick. This structure converts the two orthogonal torques generated from the MR actuators into the resistant force that can be felt in the working area. All the movable elements of the joystick are limited and linked by the frame, which was made of aluminium, due to considerations of weight and of the capability and the strength requirements. Another function of the frame structure was to make it possible to fix the joystick on the experiment table by the screws when the simulating force was stronger than the weight of the joystick. The components of the gimbal structure and one of the actuator holders are shown in an exploded view in Fig. 6.1(b), and drawings of all of the components are given in Appendix C. The mechanical design of the crucial components will be described in the next part.

## 6.3 DESIGN OF THE GIMBAL STRUCTURE

The gimbal structure is the essential structure in the joystick design that converts the two resistant torques into a resistant force on the working surface. This structure includes a handle, an arch shaft and a straight shaft as shown in Fig. 6.2. In the consideration of the strength and the rotation range, the rotation of the handle was limited to $50^{o}$, so the handle can be rotated along the x direction within a range of $120^{o}$ as shown in Fig. 6.2(a) and (b). The rotation limitation of the arch shaft was also

designed at 120° to make the movement of the handle symmetric in both directions, see Fig. 6.2 (c) and (d).

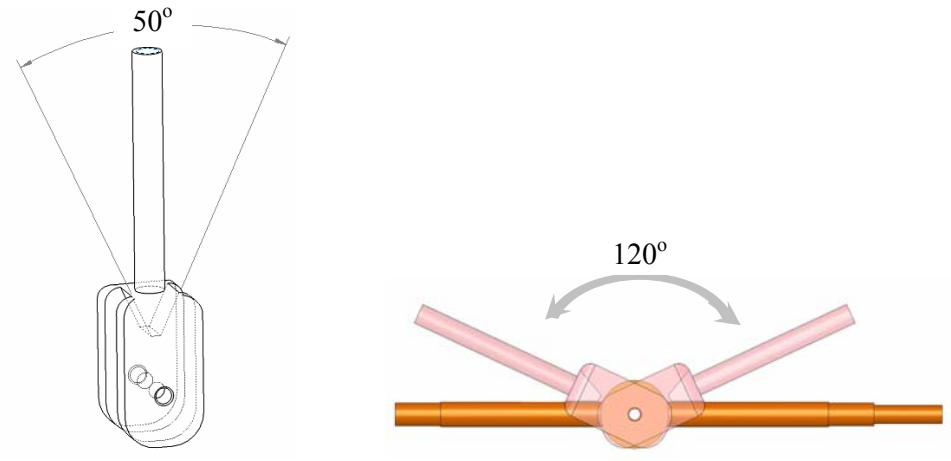


(a) Handle

(b) Movement along X direction

(c) Arch shaft

(d) Movement along Y direction

(e) Assembled structure

Figure 6.2 Gimbal structure.

The assembled structure, shown in Fig. 6.2(e), shows that the handle can be arbitrarily rotated in the working area. Pictures of the MR joystick are given in Fig. 6.3.

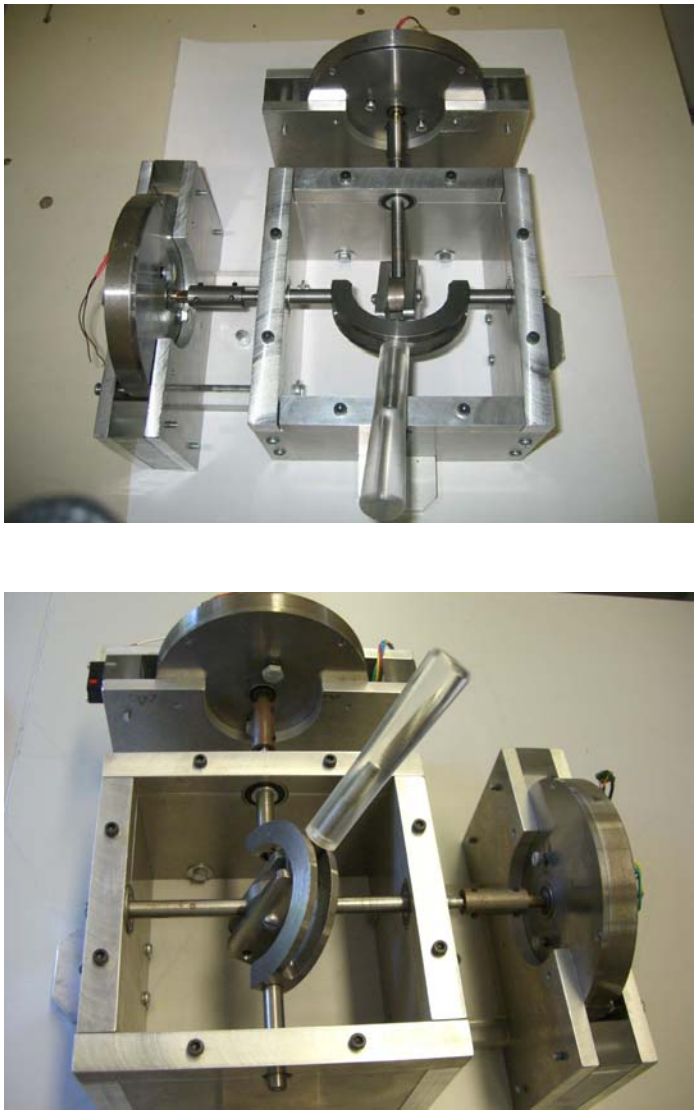

Figure 6.3 The MR joystick.

## 6.4 STATIC TORQUE ANALYSIS OF THE JOYSTICK

The sub-hysteresis model was derived to predict the actuator torque accurately in the previous chapter. The purpose of the joystick torque analysis was to get an accurate

handle torque that is composed of the two actuator torques and acts directly on the palm of the operator..

The torque model was set up in spherical coordinates for the reason that the working surface of the top point of the handle is a spherical surface. The origin of the spherical coordinates was set coincident with the origin of the rectangular coordinates, which was built up based on the geometrical relationship of the actuators. As shown in Fig. 6.4, $\theta$ is the degree of longitude and $\phi$ is the degree of latitude of the spherical coordinates. $\alpha_x$ and $\alpha_y$ are the degrees of rotation of the two MR actuators. *M* is used to express the components of the torque in different directions.

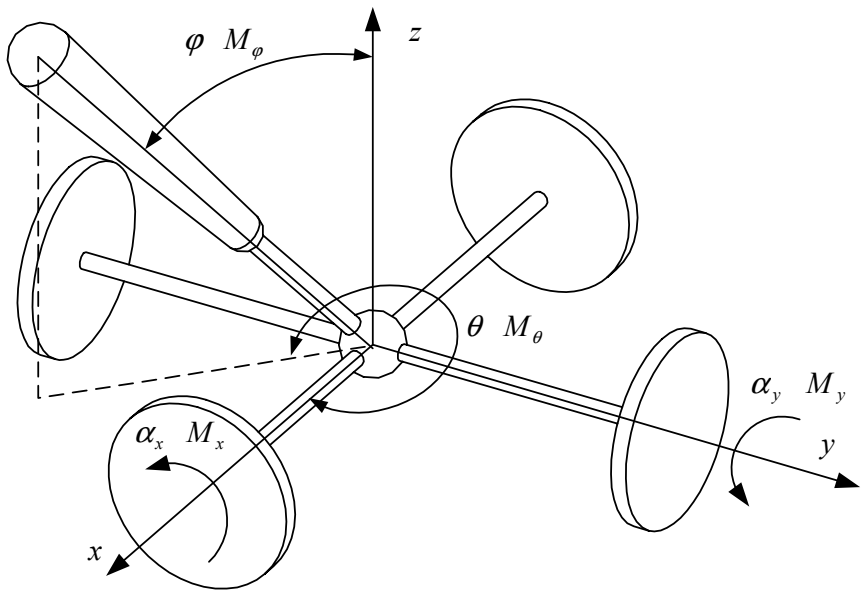


Figure 6.4 Static torque analysis.

The relationship between the spherical coordinates and the angles of the MR rotor can be expressed as:

$$\varphi = \arctan\sqrt{\tan^2\alpha_x + \tan^2\alpha_y}$$
$$\theta = -\arctan\left(\frac{\tan\alpha_x}{\tan\alpha_y}\right) \tag{6.1}$$

Then the differential matrix can be obtained as:

$$\begin{bmatrix} d\varphi \\ d\theta \end{bmatrix} = \begin{bmatrix} \dfrac{\tan\alpha_x}{\sqrt{\tan^2\alpha_x+\tan^2\alpha_y}(1+\tan^2\alpha_x+\tan^2\alpha_y)\cos^2\alpha_x} & \dfrac{\tan\alpha_y}{\sqrt{\tan^2\alpha_x+\tan^2\alpha_y}(1+\tan^2\alpha_x+\tan^2\alpha_y)\cos^2\alpha_y} \\ -\dfrac{\tan\alpha_y}{(\tan^2\alpha_x+\tan^2\alpha_y)\cos^2\alpha_x} & \dfrac{\tan\alpha_x}{(\tan^2\alpha_x+\tan^2\alpha_y)\cos^2\alpha_y} \end{bmatrix} \begin{bmatrix} d\alpha_x \\ d\alpha_y \end{bmatrix}$$
$$= \begin{bmatrix} A_{11} & A_{12} \\ A_{21} & A_{22} \end{bmatrix} \begin{bmatrix} d\alpha_x \\ d\alpha_y \end{bmatrix} \tag{6.2}$$

By using the principle of virtual work, which can be used in statics for solution of equilibrium problems, the relationship between the torque of the handle and the damping torque of the MR actuator can be expressed as:

The torque due to $M_\varphi$

$$\begin{cases} M_x = \dfrac{-\tan\alpha_x}{\sqrt{\tan^2\alpha_x+\tan^2\alpha_y}(1+\tan^2\alpha_x+\tan^2\alpha_y)\cos^2\alpha_x} M_\varphi \\ M_y = \dfrac{-\tan\alpha_y}{\sqrt{\tan^2\alpha_x+\tan^2\alpha_y}(1+\tan^2\alpha_x+\tan^2\alpha_y)\cos^2\alpha_y} M_\varphi \end{cases} \tag{6.3}$$

and the torque due to $M_\theta$

$$\begin{cases} M_x = -\dfrac{\tan\alpha_y}{(\tan^2\alpha_x+\tan^2\alpha_y)\cos^2\alpha_x} M_\theta \\ M_y = -\dfrac{\tan\alpha_x}{(\tan^2\alpha_x+\tan^2\alpha_y)\cos^2\alpha_y} M_\theta \end{cases} \tag{6.4}$$

The resistant torques of the two MR actuators can be given as:

$$\begin{bmatrix} M_x \\ M_y \end{bmatrix} = \begin{bmatrix} A_{11} & A_{21} \\ A_{12} & A_{22} \end{bmatrix} \begin{bmatrix} M_\varphi \\ M_\theta \end{bmatrix} \tag{6.5}$$

The torque values of any points on the spherical working surface can be decomposed into the two resistant torques by Eq. 6.5. Therefore, the controllable torque generated by the two MR actuators can be used to simulate the virtual force.

## 6.5 WORKING SURFACE DEFORMATION

The real working surface of the joystick is a part of a spherical surface, which is calculated by MATLAB and plotted in Fig. 6.5. The length of the handle is 10cm. The top point in the figure shows the position of the end point of the joystick handle in a vertical state. The four corners of the figure represent the handle positions in the limiting cases: the two rotations get their maximum (+120$^o$) or minimum (-120$^o$) values respectively.

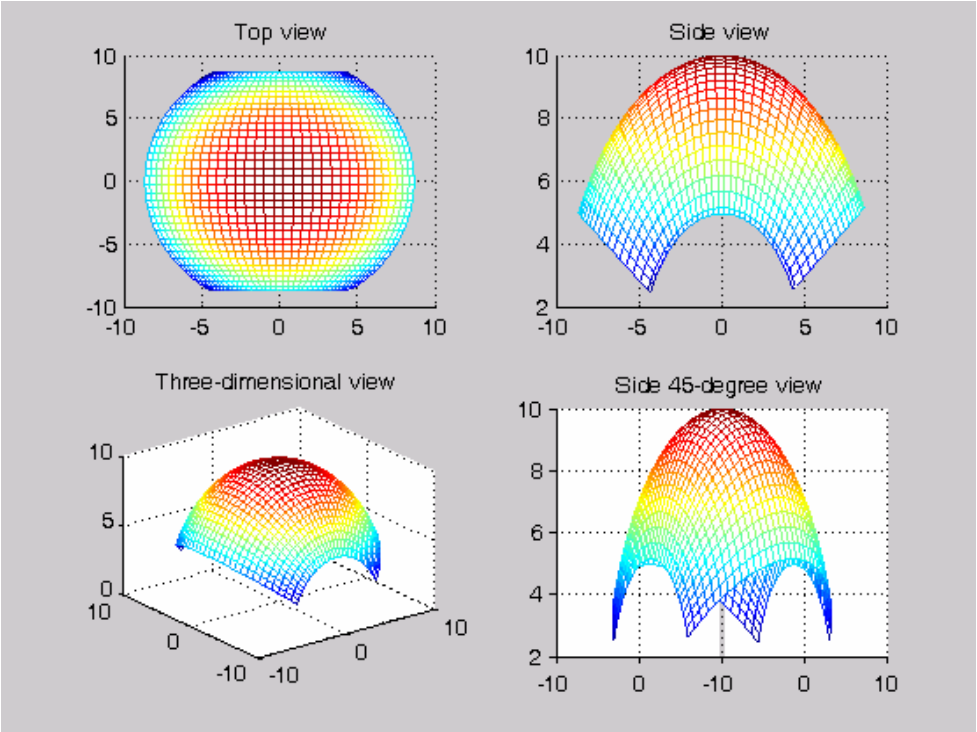


Figure 6.5 The working surface of the joystick.

The virtual environment in the computer is usually built up in rectangular coordinates rather than spherical coordinates, so a certain mapping transformation needs to be defined between the two environments. This spherical working surface is defined by the longitude lines and the latitude lines, which means by the corresponding rotary degrees of the two MR actuators. Each of them runs from –120$^o$ to +120$^o$. The force users can feel is always tangent to the sphere surface. To make this working sphere surface simulate the virtual flat surface in the virtual environment, the spherical surface is deformed into a square surface by changing the angle units into length units as shown in

Fig. 6.6. This mapping method was based on human perception and reduces the calculation of the surface deformation by ignoring the coupling of the two rotations.

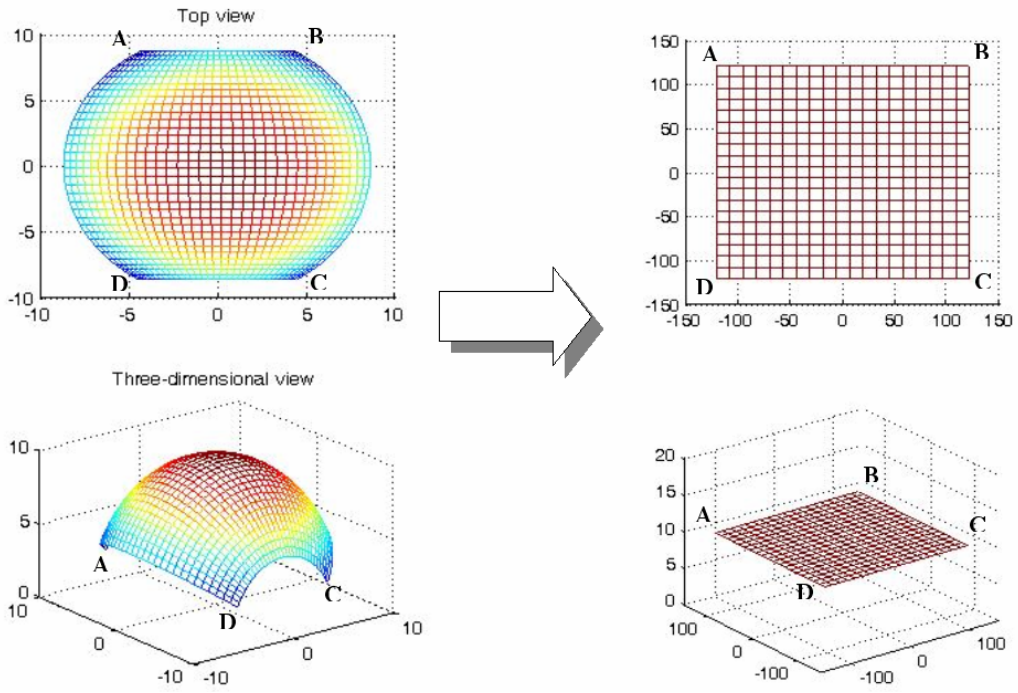


(a) Before deformation (b) After deformation

Figure 6.6 Working surface deformation.

## 6.6 PSEUDO 3D STRATEGY

### 6.6.1 Surface Switching Strategy

This joystick was designed as a 2-DOF haptic device that can be used to simulate the virtual force in a 2D surface. If this device can simulate a 3D virtual environment, the field of application of the joystick would be significantly extended. The structure of the joystick makes it impossible to perform 3D applications by a mechanical method. So a working surface switching control strategy was developed to make the 2D haptic joystick simulate 3D applications.

In the working surface switching method a surface-switching button was used to switch the working surface between the X-Y plane and the X-Z plane as shown in Fig. 6.7. The joystick uses two potentiometers: potentiometer A and potentiometer B, to detect

the rotation in the two directions. A surface-switching button was fixed on the frame of the joystick. In the working surface switching strategy, potentiometer A is used to detect the rotation in the horizontal direction all the time, and the value of the potentiometer is the value of the X direction; Potentiometer B is used to detect the vertical rotation, which is the sum of the Y and Z directions. The surface-switching button is used to decide whether the detected value represents the value of Y or the one of Z. For instance, if the button is switched off, the value detected by potentiometer B represents the value of Y, so the working surface is chosen as the X-Y plane. The cursor in the computer can be moved arbitrarily in the X-Y plane. When the button is switched on, the value detected by potentiometer B represents the value of Z, and the working surface is switched into the X-Z plane. The present value $y_o$ is held in a certain address in the RAM of the computer, and the cursor movement can be controlled in the X-Z plane by the joystick as shown in Fig. 6.7(a). Similarly, when the button is switched off again, $z_o$ as the present value of Z is held in the RAM. The working surface is switched back into the X-Y plane with a different value of Z as shown in Fig. 6.7(b). Therefore, the MR joystick can simulate a virtual environment in a 3D space. This pseudo 3D simulating strategy can not be used in the circumstance where all the three position parameters change at the same time, so the applications of this joystick are focused on all the 2D and certain 3D VR fields. A joystick that can detect any 3D information will be designed in our further research.

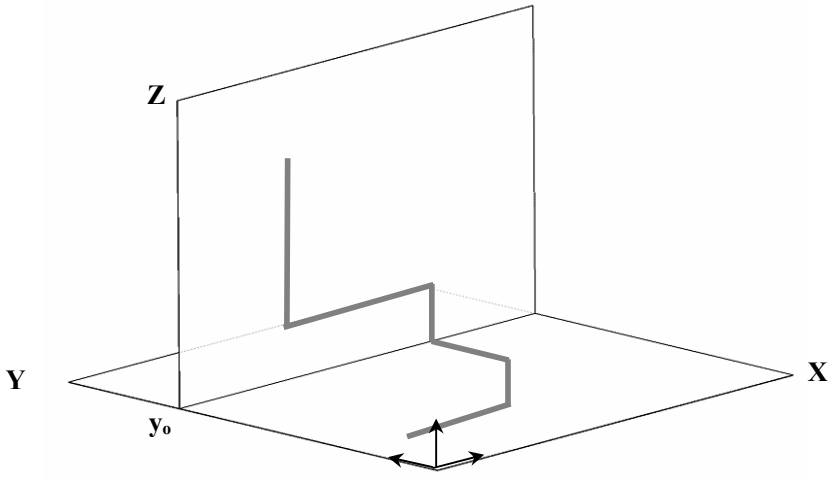


(a) The first switch of the working surface

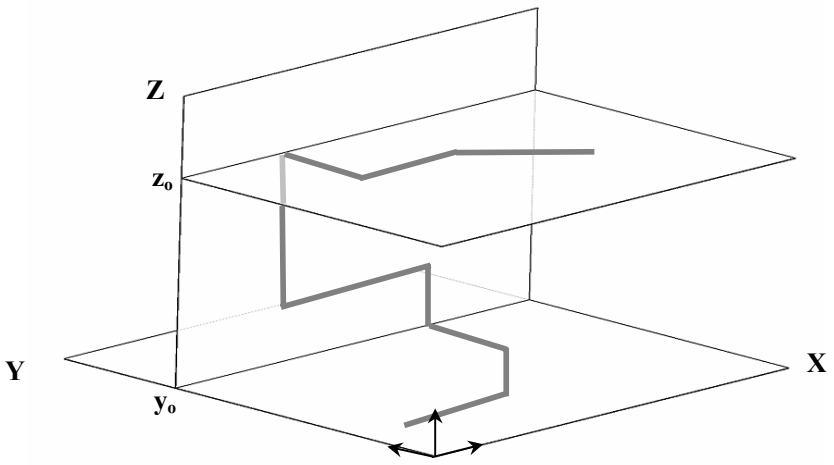


(b) The second switch of the working surface

Figure 6.7 Surface switching control strategy.

### 6.6.2 3D Working Space Deformation

The simulation space of the joystick in VR is a part of a thick spherical shell when the working surface switching strategy is used as shown in Fig. 6.8. People are not familiar with this space. This is because it would feel strange if they move the handle of the joystick by the same distance in different areas of this shell space and the movement of the cursor would be different. This will involve mistakes when people simulate the virtual force in a 3D space by the joystick.

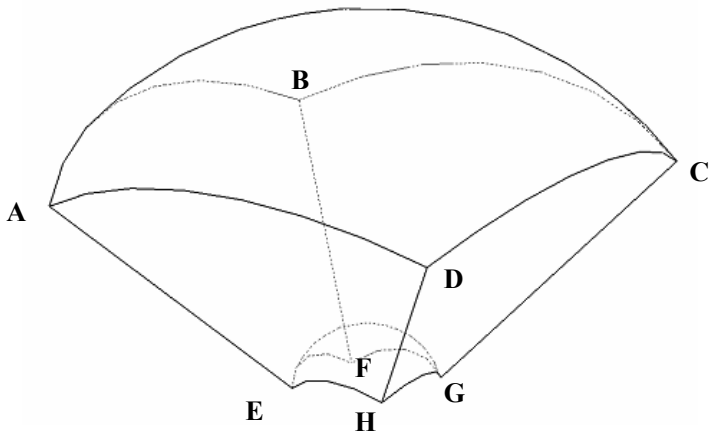


Figure 6.8 The original simulation space.

To solve this problem, a space deformation method was used for the 3D VR applications that was similar to the surface deformation mentioned before. By using the three angle units as the length units in a new set of rectangular coordinates, the spherical shell space can be deformed into a rectangular parallelepiped that is 120 units in length and 60 in width and height as shown in Fig. 6.9(b).

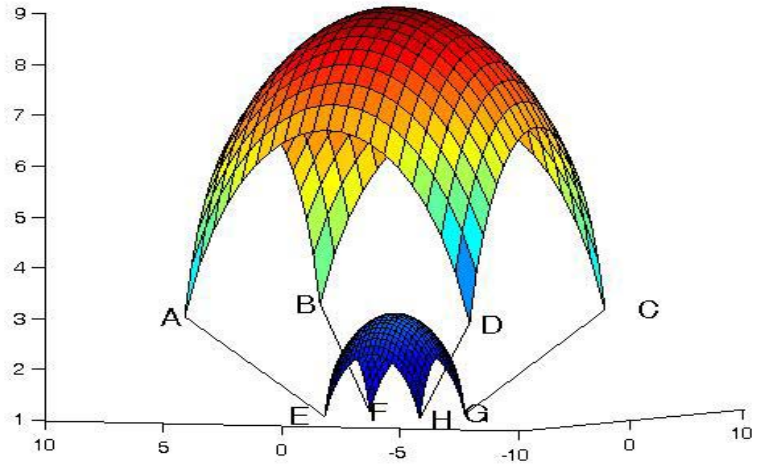


(a) Original spherical shell space

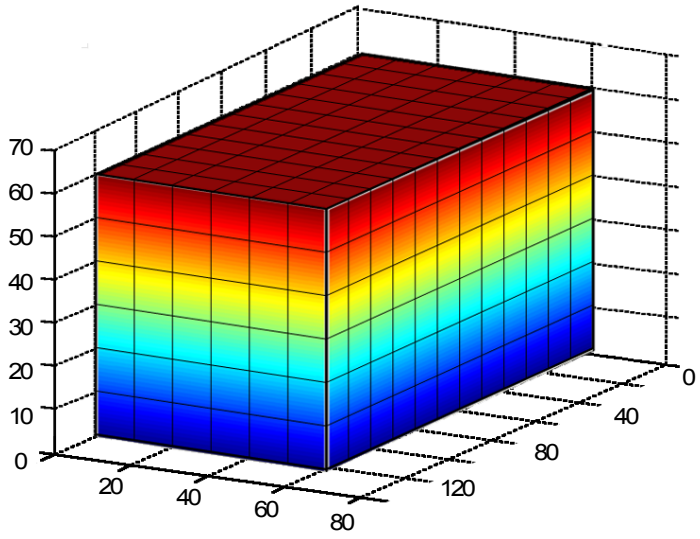


(b) Rectangular parallelepiped space

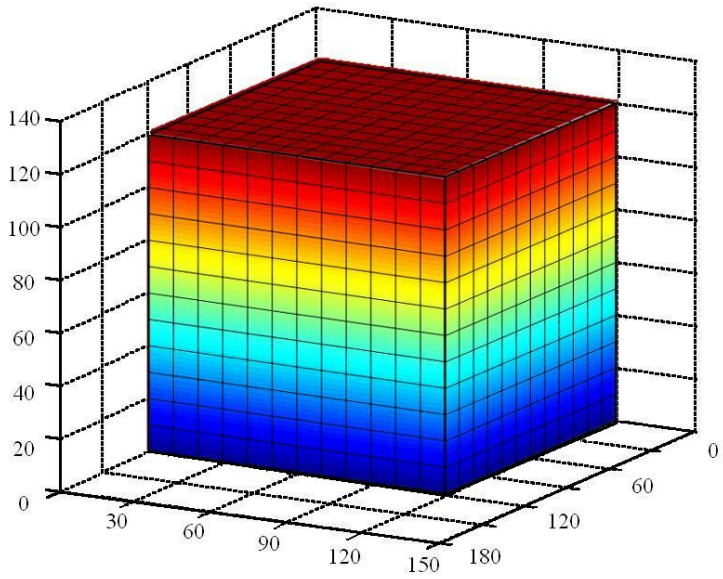


(c) Cubic space

Figure 6.9 Working space deformation.

In this parallelepiped, the movement of the cursor and that of the handle are in a linear relationship. By enlarging the units of Y and Z twice, the parallelepiped can be further deformed into a cubic solid as shown in Fig. 6.9(c). Both these two rectangular simulation spaces with their own properties can be used in VR, and some applications based on the two spaces will be demonstrated in Chapter 8.

# CHAPTER 7
# DATA ACQUISITION AND POWER AMPLIFICATION

This chapter focuses on the electric circuit design including the data acquisition (DAQ) system and the power amplification pack. The host computer gets position information on the MR joystick via the DAQ system and controls the joystick by an electric current amplified by the power amplifier. The major tasks associated with the DAQ are sensor selection, DAQ card selection, sample rate, filtering, and digitization. These tasks are not isolated, and the parameters of the elements have relations and interactions with each other in a working system. A 2-channel linear power amplifier will be designed in the second part of this chapter. Each channel of the amplifier can provide a strong and accurate drive current to one MR actuator, respectively. The current limitation strategy adopted in this amplifier can protect the coils of the MR actuators in the condition of high current. The DAQ system, the power amplifier, and the MR joystick are linked by shielded cables as shown in Fig. 7.1.

Figure 7.1 DAQ and Power amplifier for the MR joystick.

## 7.1 DATA ACQUISITION (DAQ)

Data acquisition is the process of gathering information in an automated fashion from analog and digital measurement sources such as sensors and devices under test. Data acquisition uses a combination of PC-based measurement hardware and software to provide a flexible, user-defined measurement system [60]. Usually, the raw input signal

is in the form of an analog voltage whose amplitude varies continuously over time. This voltage is produced by DAQ hardware, which can modify it by amplification and filtering processes. This procedure is named signal conditioning. After signal conditioning, the analog voltage is sampled at regular intervals. The signal is then converted from an analog signal into a digital signal before transmission to the attached computer. The software in the computer is used to analyze the detected signal and display this signal in a certain form. The user, through the LabVIEW DAQ package, can set most of the parameters that affect acquisition. To make a good detection, the parameters must be appropriate for the signals being detected. In some disciplines, tables of suggested sampling rates, ranges, and filter settings can be found, but these should not be applied blindly. A specific DAQ system should be set up based on the characteristics of the signal and the circumstances. The DAQ procedures in the haptic system are shown in Fig. 7.2.

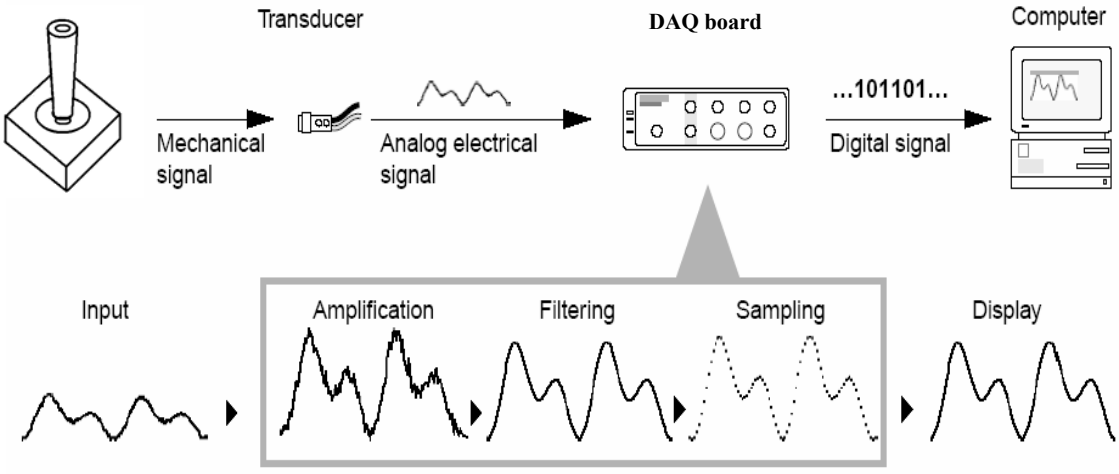


Figure 7.2 DAQ procedures in the haptic system.

The following sections will present the detailed information on transducer selection, sampling, filtering, and digitization of the DAQ procedures of this project.

### 7.1.1 Sensor Selection and Testing

In this project the linear properties of the sensor are crucial, and the rotation of the joystick handle needs to be accurately detected. Two linear low resistance single gang potentiometers were chosen as transducers that could be rotated by the shaft of the MR actuators. The potentiometer has a 9mm diameter panel mounting holes and all pots include aluminium nuts and washers. The potentiometer was chosen to be 3W 50V 1kOhm model, since the detecting range of the DAQ board is –10 - +10V and the power supply can provides the potentiometers with a +12V voltage input. A picture of the linear potentiometer and the installation of the potentiometer are shown in Fig. 7.3.

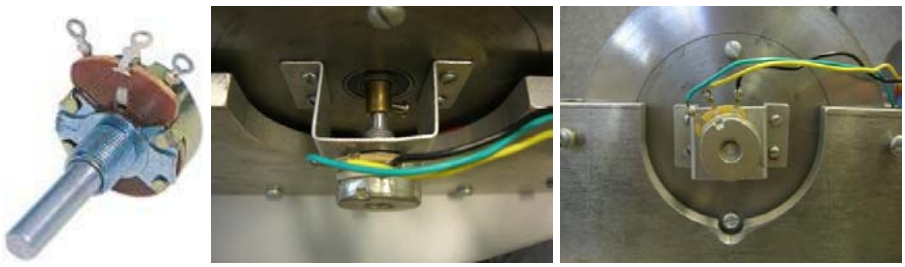

Figure 7.3 The linear potentiometer.

The test results on the linearity on the potentiometer are shown in Fig. 7.4. This figure shows the curve of the output voltage versus the degree of rotation with a +12V power supply. The error range of this kind of potentiometer is 0.1%.

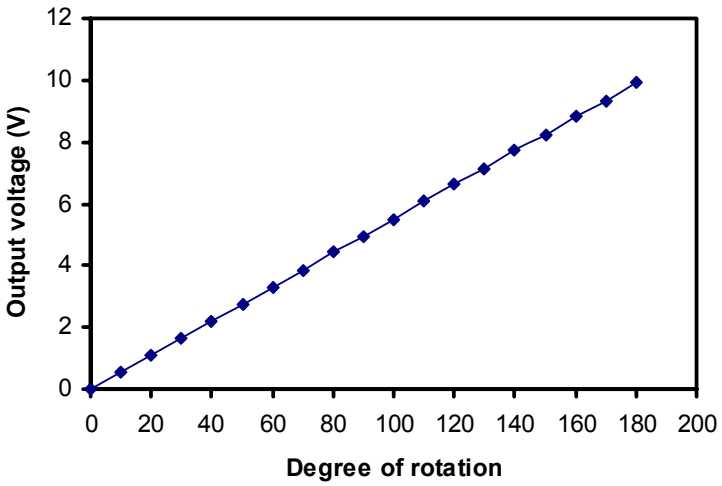


Figure 7.4 Testing of the potentiometer.

### 7.1.2 DAQ Board

A National Instruments PCI-6221 was chosen as the DAQ board for this project, since this DAQ board can be seamlessly linked with LabVIEW, which was used to design the control and display unit in this haptic system. PCI-6221 is a low-cost multifunction M Series DAQ board optimized for multiple data acquisition applications. The board offers 16 analog inputs, 2 analog outputs, 24 digital I/O lines, and two counter/timers. The NI PCI-6221 is ideal for applications including data logging, control, and sensor and high-voltage measurements when used in conjunction with NI signal conditioning.

The maximum frequency of data acquisition provided by the PCI-6221 is 1MHz, which can fulfil the requirements of the haptic signal acquisition and generation. The sample frequency of the system will be discussed in the next section. The ADC (Analog-to-Digital Converter) and DAC (Digital-to-Analog Converter) provide 16 analog input and 2 analog output ports on this board. Two analog input ports (P.68 and P.33) were used to acquire the position signal expressed by X and Y values of the 2D working area. Another input port (P.65) was used to detect the working plane switching signal when a 3D haptic simulation task was performed. The two analog output ports (P.21 and P.22) provided control signals to the power amplifier to drive the two MR actuators. The grounds of the input and the output were chosen as P.67 and P.55 respectively. The corresponding pins can be found in Fig. 7.6, which shows the interface of the PCI-6221.

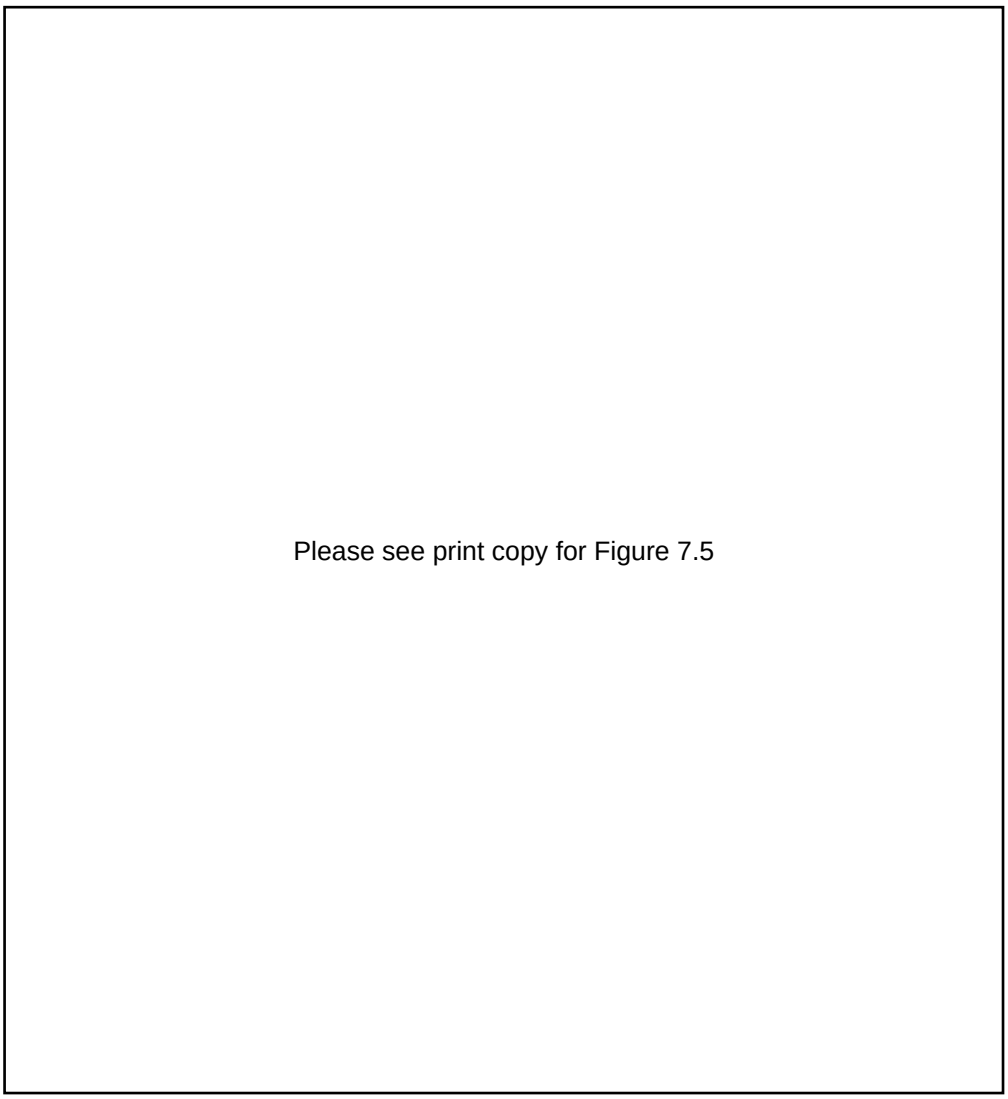


Figure 7.5 PCI-6221 (68 Pin) Pin-out schematic[62].

The PCI-6221 was connected to the SCB-68 with a shielded 68-conductor cable. The SCB-68 is a shielded I/O connector block with 68 screw terminals for easy signal connection to a National Instruments 68-pin DAQ device. The SCB-68 features a general breadboard area for custom circuitry and sockets for interchanging electrical components. These sockets or component pads allow RC filtering, 4 to 20 mA current sensing, open thermocouple detection, and voltage attenuation. The position signal can be transferred to the DAQ board, and the control signal can be sent to the MR joystick via this connector block. A picture of the SCB-68 is shown in Fig. 7.6.

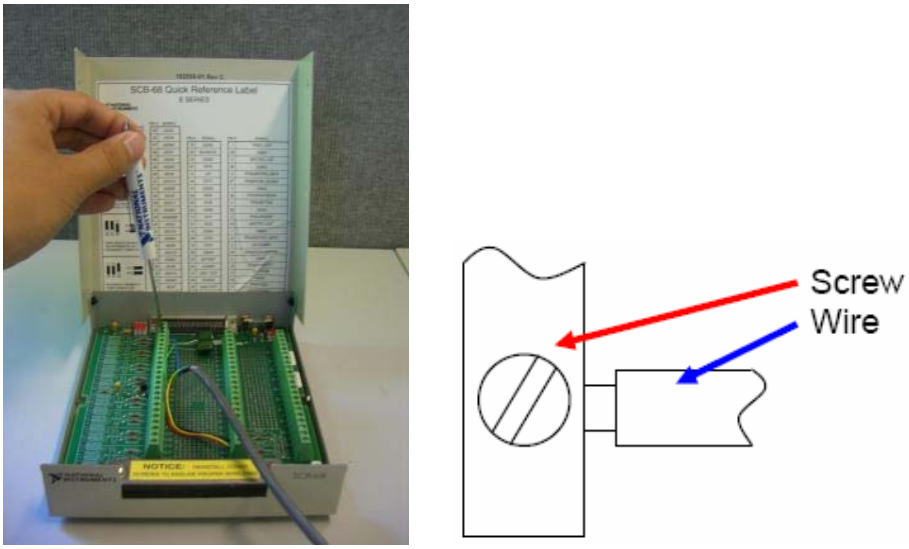


Figure 7.6 SCB-68 connector block.

The analog input channels on the SCB-68 can be configured for one of three input modes: differential, referenced single-ended, or non-referenced single-ended. These modes are called DIFF, RSE, and NRSE input modes, respectively. In this project, the RSE mode was adopted because the position information was in the form of slow varying signals and a common ground was necessary in this system. The block diagram for RSE is given in Fig. 7.7.

Please see print copy for Figure 7.7

Figure 7.7 Referenced single-ended (RSE) mode [63].

The SCB-68 printed circuit diagram, reference label, and jumper configuration are attached in Appendix D. When measuring single-ended floating signal sources, the DAQ device must be configured for RSE input mode to supply a ground reference. In this mode, the negative input of the instrumentation amplifier on the DAQ device is tied

to the analog ground. To use the SCB-68 with single-ended inputs, where ACH<i> and ACH<i+8> are used as two single-ended channels, it is necessary to configure the SCB-68 jumpers in their factory-default configuration as shown in Fig. 7.8. In the factory-default configuration, jumpers on the SCB-68 were in the two series positions. In this configuration all the signal grounds were connected to AIGND and the connection method is shown in Fig. 7.9.

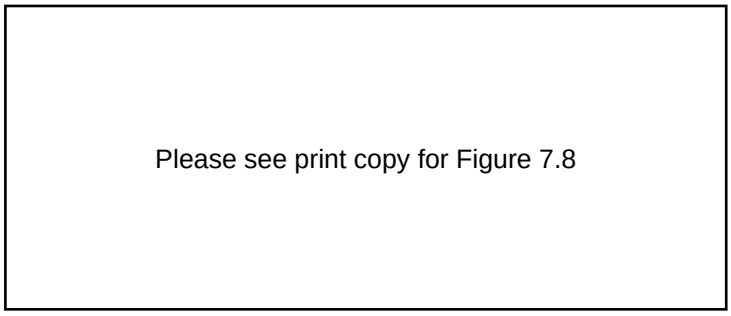


Figure 7.8 Jumper Configuration for RSE mode [63].

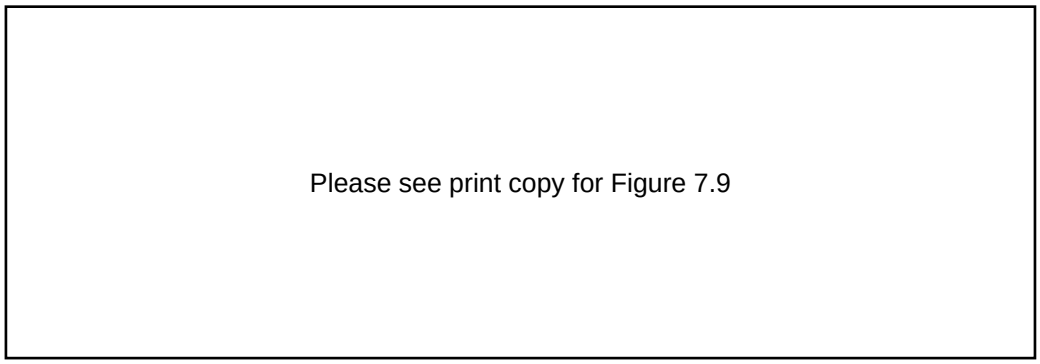


Figure 7.9 Single-Ended Input Connections for Floating Signals [63].

### 7.1.3 Sampling

The system is expected to detect accurately the movement of the hand and fluently show the effects on the VR though the monitor. The minimum working frequency of this haptic system is decided by the maximum frequency of the movement of the joystick handle and the frequency associated with the persistence of vision. As is known, the maximum frequency of hand movements is about 10 Hz, and the critical flicker frequency for a monitor is 45 Hz. In consideration of both the critical biological

frequency and the capabilities of the DAQ card and computer, the system frequency was chosen as 100Hz, which can be set by a timer in software programming.

### 7.1.4 Noise and Filtering

Lowpass filters are designed to help reduce noise and give a smoother signal in this system. A simple lowpass filter consists of a resistor and a capacitor; the voltage across the resistor is the measured input signal to the filter. The structure of the lowpass filter is shown in Fig. 7.10.

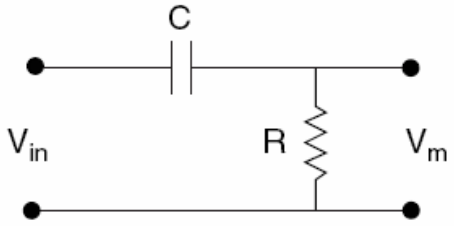


Figure 7.10 Structure of the lowpass filter.

This filter has a time constant of $\frac{1}{2\pi RC}$. The cut-off frequency $f_c$, is defined as the frequency beyond which the gain drops 3 dB. Instead of having a gain of absolutely zero for frequencies greater than $f_c$, the real filter has a transition region between the passband and the stopband, a ripple in the passband, and a stopband with a finite attenuation gain.

The component values in the circuit can be determined by fixing $R$ as 1.6 kΩ and by choosing $f_c$ as 100Hz. The value of $C$ can be derived as 1μF from equation 7.1 as follows:

$$C = \frac{1}{2\pi R f_c} \tag{7.1}$$

### 7.1.5 Digitization

The last step in the DAQ procedure is to convert the analog signal into a digital signal by using the ADC. The analog data must conform to a fixed number of values when it is converted into digital form for use by the computer.

The PCI-6221 has a multiplexer that acts like a switch between different channels in the ADC. Therefore with one ADC, this DAQ board is able to perform a multi-channel acquisition task. The PCI-6221 is a 16-channel analog input board. This makes it possible to acquire up to 16 analog signals in parallel. This project used two of them to acquire a 2D position signal from the joystick handle.

Resolution of the analog input signal converted into digital data is another critical parameter for an ADC that is dependent upon the number of bits the ADC uses. The resolution of the converted signal is a function of the number of bits the ADC uses to represents the digital signal. The higher the resolution, the higher the number of divisions the voltage range is broken into, and therefore, the smaller the detectable voltage change. In the PCI-6221, a 24-bit ADC is used for signal conversion. Therefore, the minimum change in voltage that could be discerned for a 10V range would be $10/2^{24}$=0.6 $\mu$ V, which was accurate enough for various VR applications.

## 7.2 POWER AMPLIFICATION

The DAC on the DAQ board can not drive an electromagnet directly since the electric current provided by it is not strong enough to generate a suitable magnetic field. The maximum drive current of the PCI-6221 is 5mA, but the maximum working current for the MR actuators was calculated as 2A. Therefore, a two-channel linear power amplifier needs to be designed to amplify the control signal between the DAC and the joystick.

### 7.2.1 Amplifier Circuit

Two amplifier circuits were designed for this project. The first one used a simple Darlington amplifier circuit to amplify the control signal. The circuit is shown in Fig. 7.11 (a) and the test results on this circuit are given in 7.11 (b).

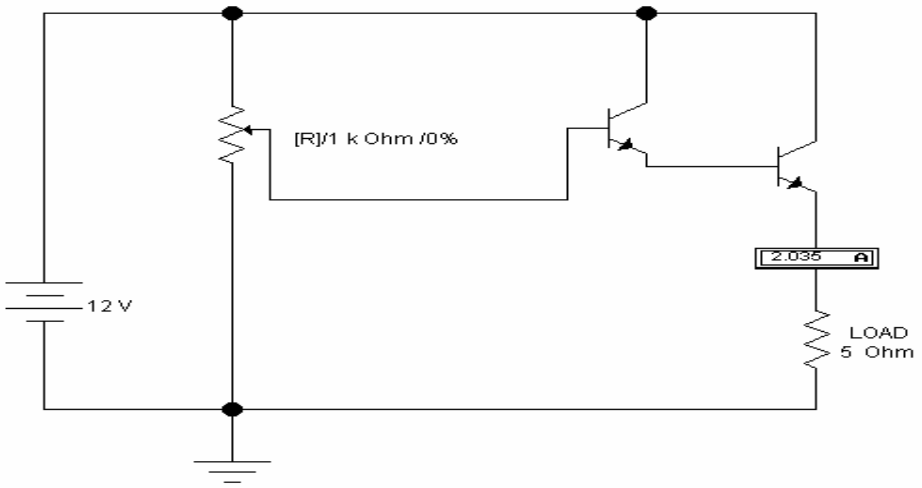


(a) Simple Power Amplifier Circuit

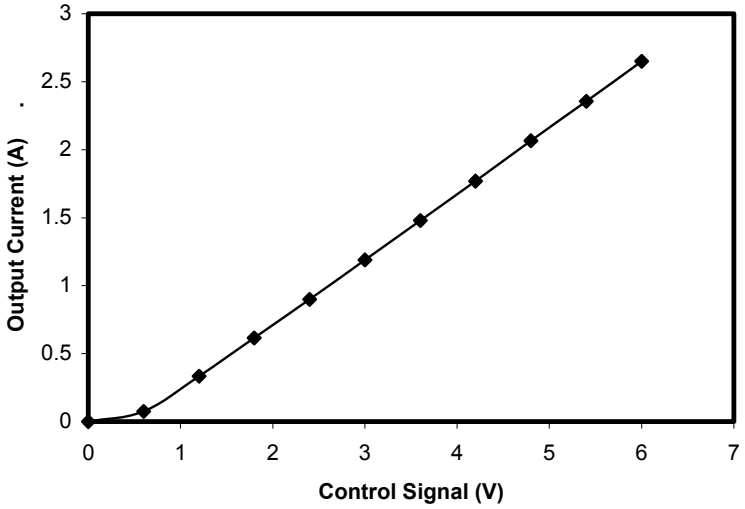


(b) Testing results

Figure 7.11 Simple power amplifier circuit and testing results.

This circuit can be easily set up for the testing of the MR actuator performance. The MR actuator was driven by this amplifier in the sub-hysteresis testing experiments before a more complicated circuit was designed. However, the output current can increase more than 3A proportionally to the control signal without any limitation, which may cause damage to the coil of the MR actuator. A fuse is needed on each drive channel to protect the coil under the conditions of excessive current if this design is adopted. Hence, a more advanced amplifier circuit was developed as shown in Fig. 7.12 (a) and (b).

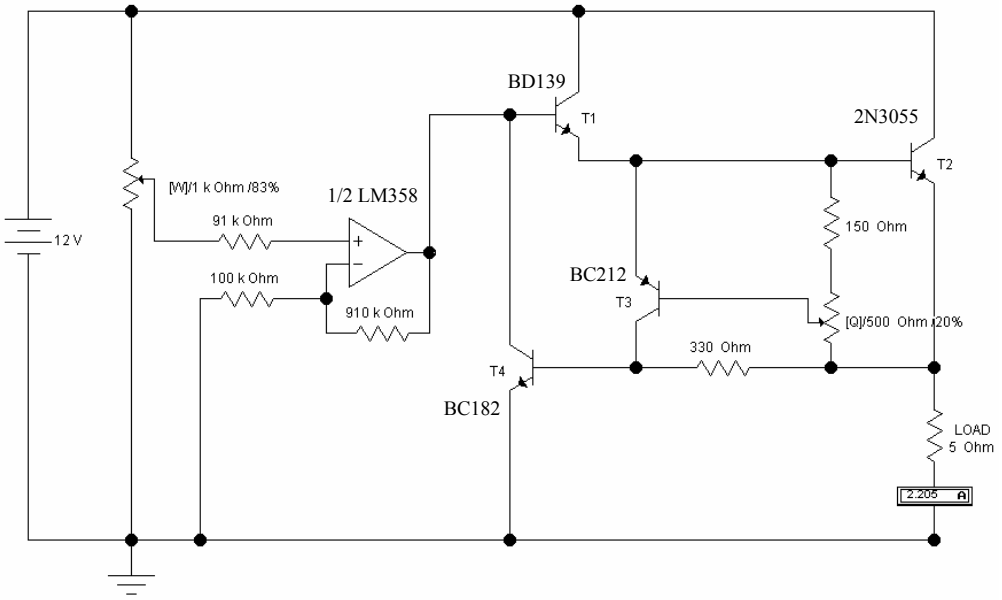


(a) Current-limiting Power Amplifier Circuit

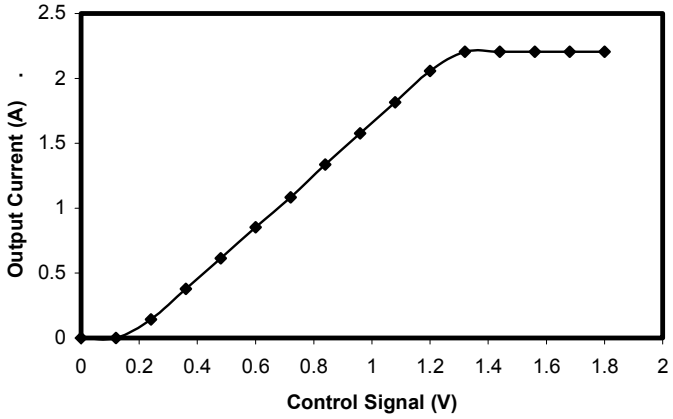


(b) Testing results

Figure 7.12 Current-limiting power amplifier circuit and testing results.

The picture just shows one channel of the amplifier, as the other channel has the same structure as this one. In the left part of this circuit an LM358 operational amplifier was used to enlarge the small control signal. In this negative feedback circuit the gain of this op amp can be calculated by

$$\frac{U_0}{U_i} = \frac{(100+910)}{100} \approx 10 \tag{7.2}$$

A Darlington structure (T1 and T2) was used to enlarge the drive current on the right side of this circuit. A heat sink is necessary when a high current passes through T2. Transistors T3, T4 and potentiometer Q are used for current limitation by current feedback when the output current is too high. The maximum driving current for the joystick coil was designed as 2.2 A, which can be adjusted by potentiometer Q. The details of the transistors used in this circuit are listed below in Table 7.1.

| Symbol | Product Code | Max Voltage (V) | Max Current (A) | Type |
|---|---|---|---|---|
| T1 | BD139 | 80 | 1.5 | NPN |
| T2 | 2N3055 | 60 | 15 | NPN |
| T3 | BC212 | 50 | 0.1 | PNP |
| T4 | BC182 | 50 | 0.1 | NPN |

Table 7.1 Transistor list.

Two 16-bit analog outputs (833 kS/s) were used to generate control analog signals that were transferred to the power amplifier via SCB-68 output ports. Pictures of the printed circuit board (PCB) are shown in Fig. 7.13.

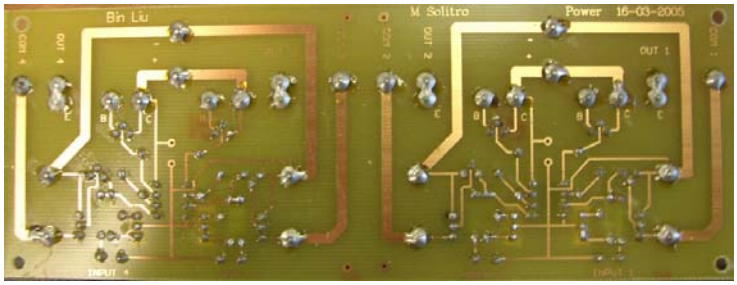


(a) Front view of the amplifier PCB

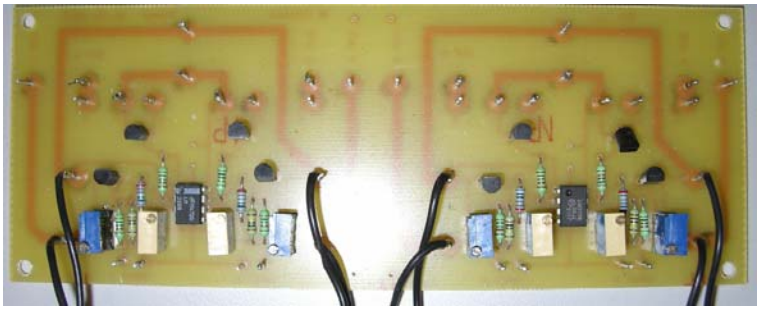

(b)Back view of the amplifier PCB

Figure 7.13 Power amplifier PCB.

### 7.2.2 Power Amplifier Interface

The sockets of the amplifier can be divided into two groups as shown in Fig. 7.14(a). The four-pin sockets are connected to the MR actuators, two pins of which are the anodes of the position sensor and the coil. The other two pins are the respective grounds. The five-pin socket is connected to the SCB-68 connecting board. Two pins are the two control signal inputs; the other two are the outputs of the joystick positions; the last pin is the common ground. The front view and the back view of the power amplifier are shown in Fig. 7.14(b).

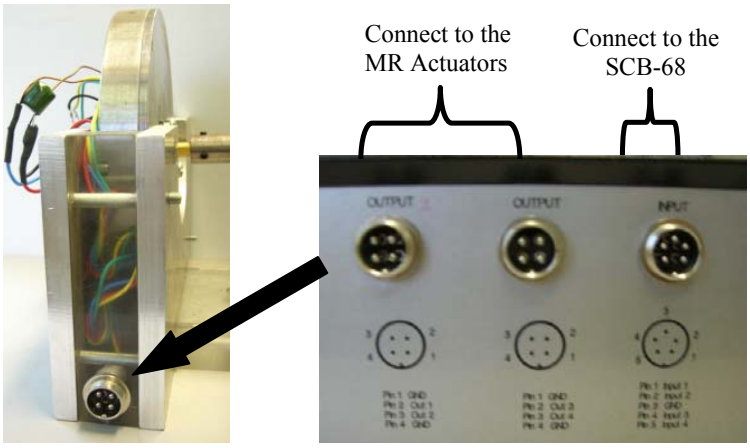


(a) Connection of the MR actuator and the amplifier


(b)The power amplifier

Figure 7.14 The 2-channel current limiting power amplifier.

# CHAPTER 8
# SOFTWARE DESIGN

The MR joystick mechanical design and the electric circuit design have been discussed in the previous chapters. This chapter will discuss the software design and present some typical applications using the developed haptic system. The program designed in this chapter acts as the control unit and display unit for the MR haptic system programmed by in LabVIEW [64], which is a graphical and event driving program tool developed by the NI company for integrating, testing, and control purposes. The designed program combines the data acquisition (DAQ) hardware, the power amplifier, and the MR joystick to form an effective real-time haptic system.

LabVIEW is a graphical development environment for creating flexible and scalable test, measurement, and control applications rapidly and at minimal cost. The graphical development platform allows the program to be developed by dragging and dropping test and measurement user interface objects from the control palette. The multiple development tools of the LabVIEW package provide numerical analysis, instrument I/O, communication solutions, etc. that simplify the program development process and enhance the reliability of the products. This automation package also offers systematic DAQ solutions and assistance for various applications related to data processing, presenting, and storage, such as fitting, FFT and file I/O. LabVIEW facilitates a wide array of applications on test and control in the areas of aerospace, the automotive and electronics industries, etc.

This system uses a computer to act as the control module and the display module. The MR joystick performs as the human interface module, through which people can feel the corresponding virtual resistance and generate reactions to the virtual environment. A picture of this haptic system is shown in Fig. 8.1.

Figure 8.1 The MR haptic joystick system.

The spirit of this system is the LabVIEW package, which is used to control the whole system and to display the visual interface for the user through a computer screen. This graphical software tool provides the user with an efficient approach for designing test, measurement, and control systems. It can also be seamlessly connected to equipment such as the PCI6221 DAQ board and the SCB-68 board that are used as the interface between the computer and the MR actuator in this haptic system. This software is composed of a block diagram panel for graphical programming and a front panel for the interface display. All the DAQ and control processes are in a while loop frame designed in the block diagram panel, the frequency of which can be set by a timer. Data acquisition is critical in a haptic application because it affects the response and the accuracy of the whole system. This project adopts DAQmx strategies to improve the DAQ performance instead of traditional NI-DAQ, as discussed in the next section.

## 8.1 DAQmx INTRODUCTION AND CONFIGURATION

### 8.1.1 DAQmx Introduction

NI-DAQmx driver software involves innovative techniques to deliver increased productivity and performance. NI-DAQmx driver software and additional measurement services software are included with a single programming interface for programming analog input, analog output, digital I/O, and counters on hundreds of multifunction DAQ hardware devices. The DAQ software designed with DAQmx can be applied in

LabVIEW, LabWindows/CVI, Visual Basic, Visual Studio .NET, and C/C++ circumstances [65]. A comparison of DAQmx and traditional NI-DAQ is given in Table 8.1.

Please see print copy for Table 8.1

Table 8.1 NI-DAQmx versus Traditional NI-DAQ [65].

### 8.1.2 DAQmx Configuration

The DAQ hardware must be installed and the driver program must be configured before DAQ programming. Measurement and Automation Explorer provides a platform for the automatic installation and some categories are device-specific. These are listed on the left of the configuration window as shown in Fig. 8.2. By simply selecting NI-DAQmx devices in the device and interfaces configuration tree, the PCI-6211 can be found and installed.

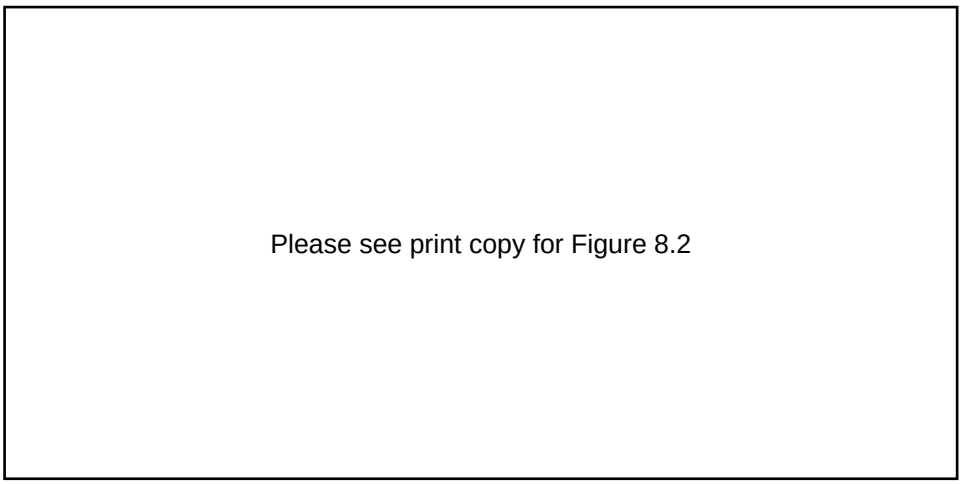


Figure 8.2 Measurement and Automation Explorer.

A DAQmx data acquisition procedure can be set up by either DAQmx single sets or DAQmx Assistant as shown in Fig. 8.3. The DAQ Assistant configuration provides the users with analog I/O, digital I/O, and counter operations in a user-friendly interface as shown in Fig. 8.4.

Most of the main parameters of a DAQ procedure, such as the voltage range, DAQ channel, sampling rate, and acquisition mode, can be simply set in this configuration interface, which greatly reduces the development time for the whole system. A program based on DAQmx single sets will be demonstrated in the next section. Single sets are used to generate more effective code by users who are familiar with every step and parameter of a DAQ procedure.

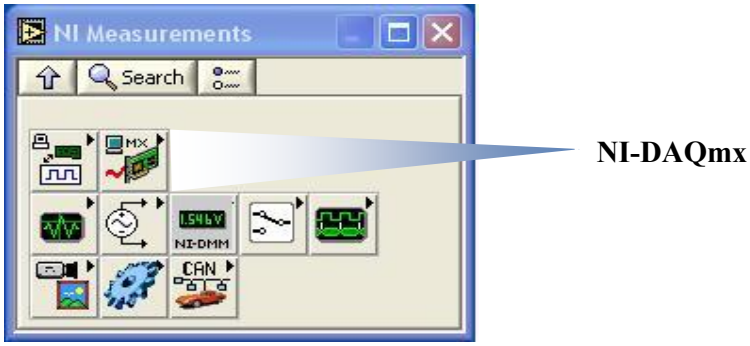


(a)

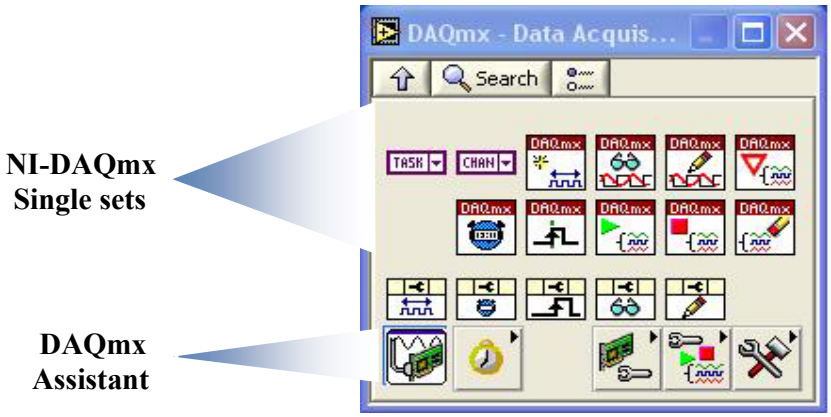


(b)

Figure 8.3 DAQmx sets in function palette.

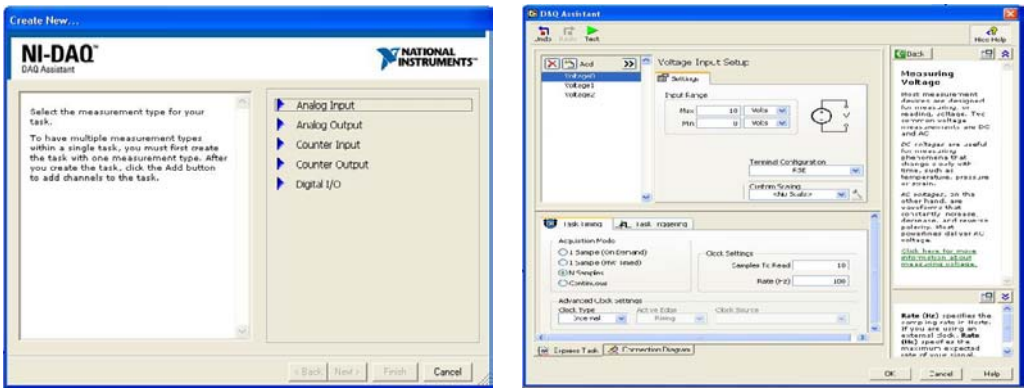


(a) (b)

Figure 8.4 DAQmx assistant configurations.

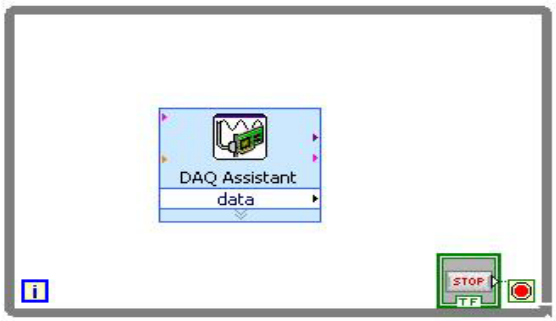


Figure 8.5 Voltage input DAQ module in a while-loop structure.

Finally, a voltage input DAQ module was built in the while-loop structure shown in Fig. 8.5. The interfaces for 1-DOF (degree of freedom) MR actuators presented in next paragraph were designed based on this structure.

## 8.2 DEMONSTRATION AND CASE STUDY

Six typical interfaces were designed for three groups of haptic applications: 1-DOF, 2-DOF, and 3-DOF applications. The front panels and the functions of the components in the front panels will be demonstrated in the first five interfaces. More programming details, including back panel and graphical displays will be presented in the last demonstration.

### 8.2.1 1-DOF Interface

There are two different interfaces, which are illustrated below in Fig. 8.6 (a) and (b). Both of them have two working models: the Joystick Control and Knob Control models. In the square screen of the first interface, the cursor can be moved vertically when the MR actuator or the simulation knob is rotated. Similarly, the pointer in the second interface would turn synchronously with the rotation of the actuator or the knob and make the actuator generate a corresponding resistant torque in terms of the value of the colour. Both of them have a press switch, a slide switch, a simulation knob, and a display unit. The press switch is the main switch of the programming, working as the power switch of a device. The slide switch is used to change the working module

between the actuator control and the knob control, which is used to simulate in the absence of the MR actuator. The significant difference between these two interfaces is derived from the display unit. The first one can only demonstrate a discrete resistant torque, while the second one can be used to simulate a continuously changing resistant torque without grading.

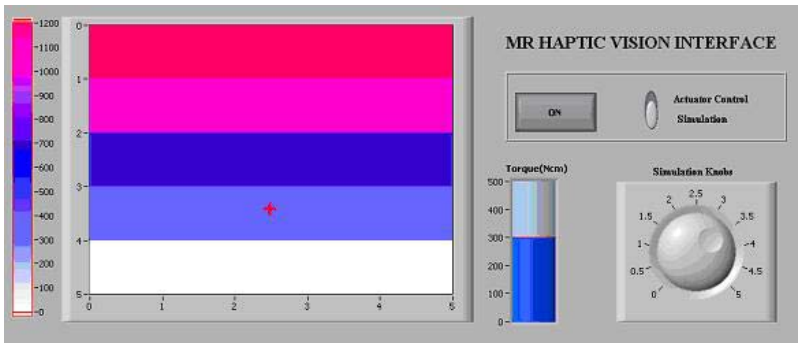


(a) Discrete torque vision interface.

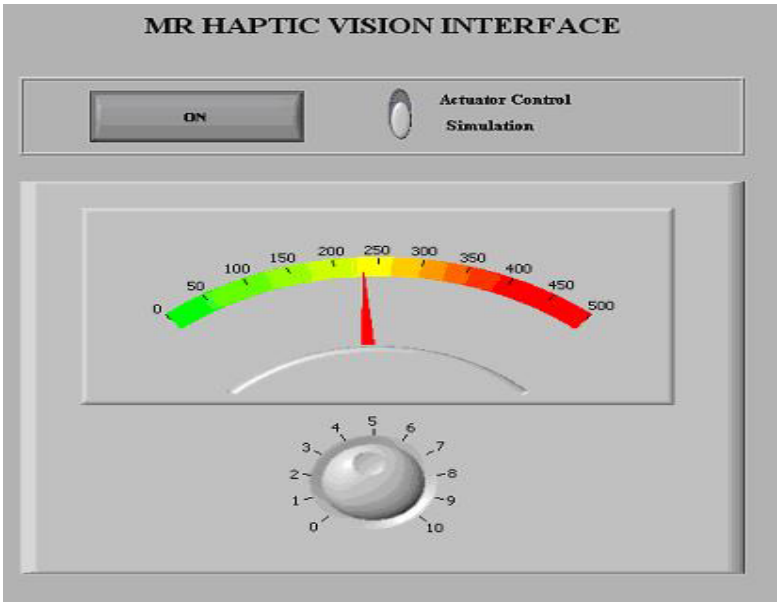


(b) Continuous torque vision interface.

Figure 8.6 1-DOF haptic interface.

### 8.2.2 2-DOF Interface

2-DOF application interfaces were designed for the joystick with two MR actuators instead of a single MR actuator. The computer generates control signals, which correspond to the position of the actuator rotors detected by the linear potentiometers. Meanwhile, such control signals activate the MR actuators to generate the resistant forces by means of the amplified current. Therefore, the operator can feel different resistant forces when the cursor is moved, controlled by the position signal generated from the potentiometer, through the image shown on the screen of the computer.

The three specific interfaces designed for 2-DOF applications are illustrated below in Fig. 8.7 (a), (b), and (c). These interfaces have adopted the same press button and slider switch to control the running procedure and to choose the working models. Two control knobs were used to present and control the movement along the X and Y directions respectively in the knob control model.

Users can feel different forces when the cursor is moved into different color square areas in the interface screen (a). A matrix is used to set the value of the resistant force, which is expressed in different colors, while the value of the resistance is presented by the force display bar. Interface (b) is a simple maze game. The user can easily move the cursor along the path using the MR joystick. If the cursor touches the blue wall, the joystick handle will not move further, as the resistant force generated by the two MR actuators becomes high. Meanwhile, the “Wrong Way” indicator light is turned on, advising the user to change the direction of motion. A slope with different types of friction was also designed in the interface (c). The sections with the white, green, and yellow colors represent ice, grass and sand areas, respectively. The resistant force

changes when one pushes the cube on the surfaces of the different materials with the haptic joystick. In the same color area, minor force changes can also be felt because of the different grades of the slopes.

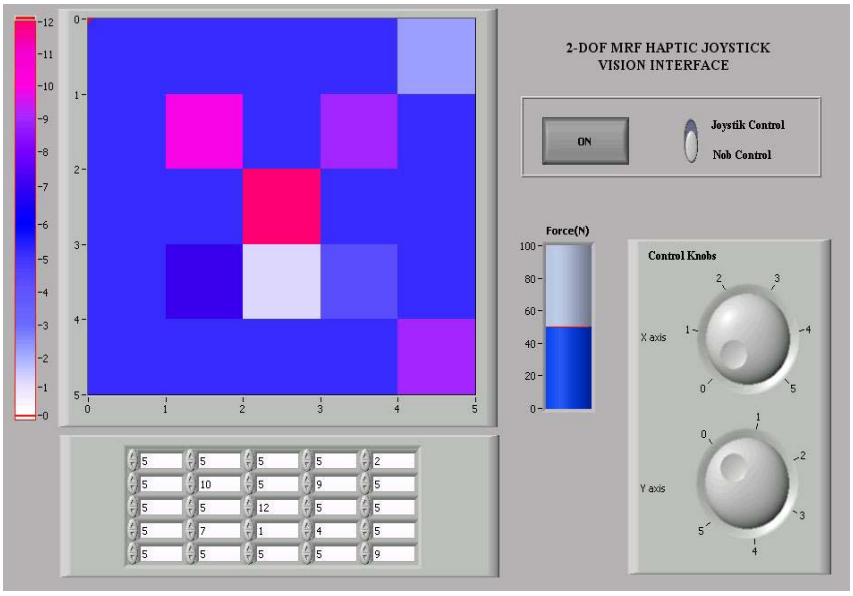


(a) 2-DOF force matrix

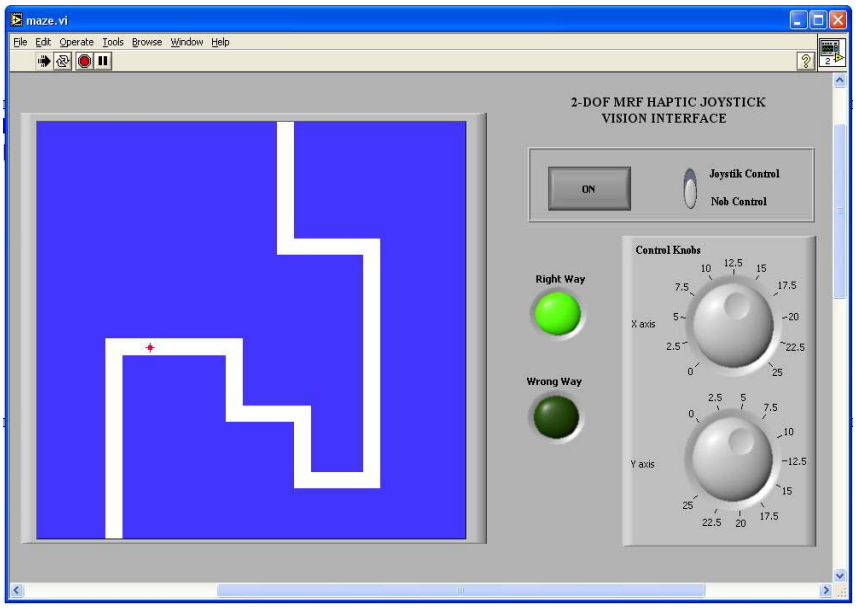


(b) Maze game with force feedback

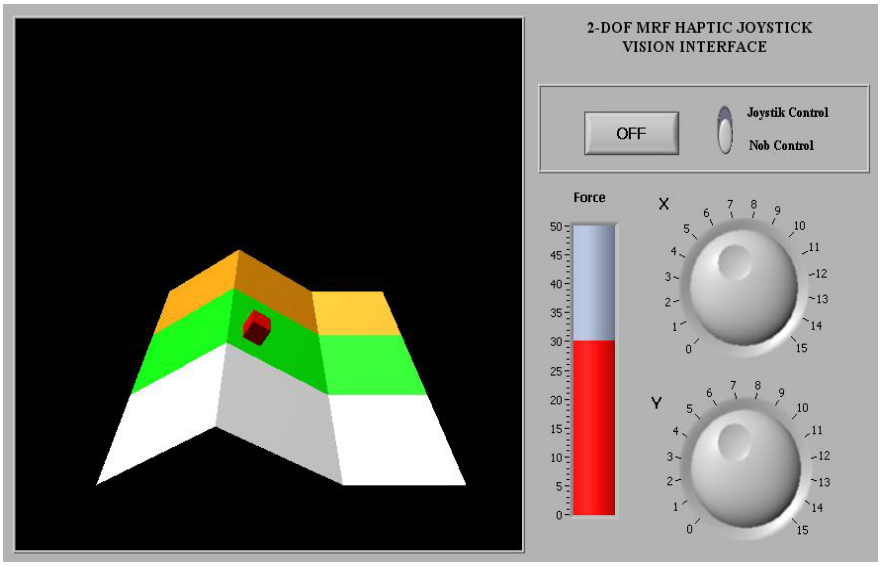


(c) Slope with different types of friction

Figure 8.7 2-DOF haptic applications.

### 8.2.3 3-DOF Application Interface

The last interface is a pseudo 3-DOF virtual surgery application. The window on the left side shows a 2D x-ray picture of a finger, and the window on the right side shows a 3D model that has been built up based on the 2D x-ray picture as shown in Fig. 8.8. When the cursor cuts into the different parts of the finger, such as the tissues and the bones, the user can feel different force exerted on the handle of the joystick. The 3D finger model can be observed in all directions by dragging the buttons of the vertical and horizontal vision control bars. The system was designed for surgical training and helping doctors to find the best surgical methods.

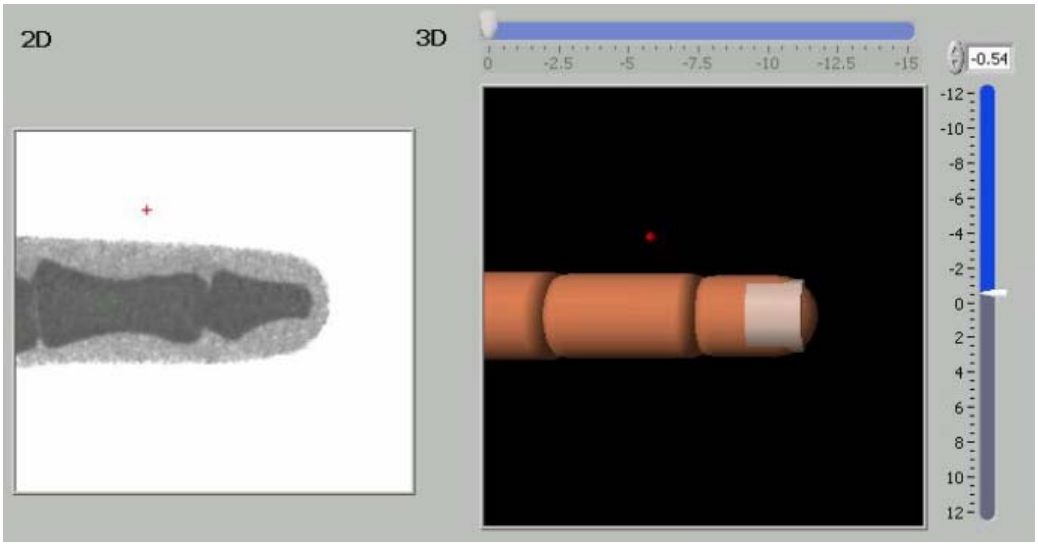


Figure 8.8 2D and 3D display windows.

The flow chart of the program is shown in Fig. 8.9. The main features of this program are the iterative remodelling and the display procedure, which are realized by a loop structure.

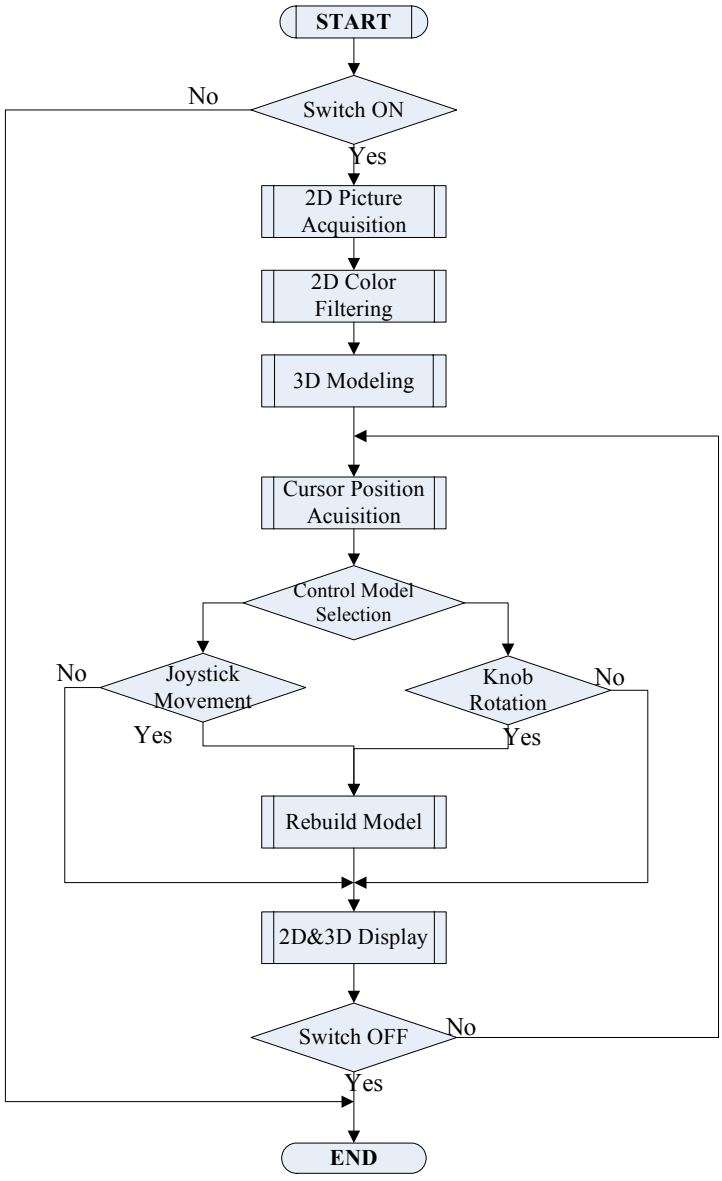


Figure 8.9 Flow chart of the programming.

The display unit includes 2D and 3D display windows, which are used to display the 2D picture and the 3D model synchronously as shown in Fig. 8.10(a). An X-ray finger picture file is read into the system and converted into a pixel map by the Pixmap function during the picture acquisition period. Then a read cross cursor is created to denote the position of the joystick. The force control signal is generated based on the gray values of the center point of the cursor. As is well known, the same tissue is

expected to show with the same gray value in an X-ray film, but real films always have disturbance colors. That means that there are always several white pixels distributed in a black area, which is caused by the resolution and the precision of the X-ray machine. These unwanted points should be detected and smoothed by the colors around them, so that the output force can represent the intensity of the tissue accurately. Hence, a color filter was introduced to smooth the center point color with the values of the neighboring five pixels as shown in Fig. 8.10(b).

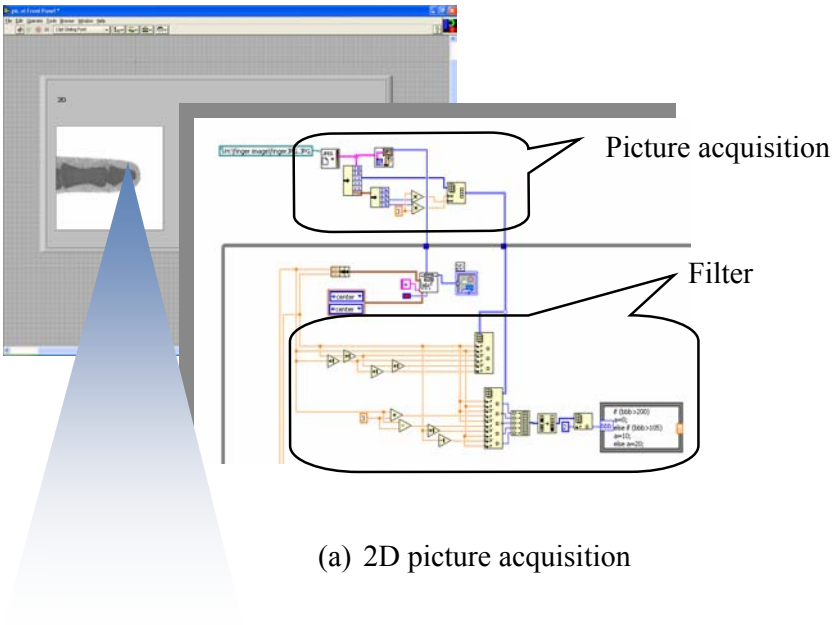


(a) 2D picture acquisition

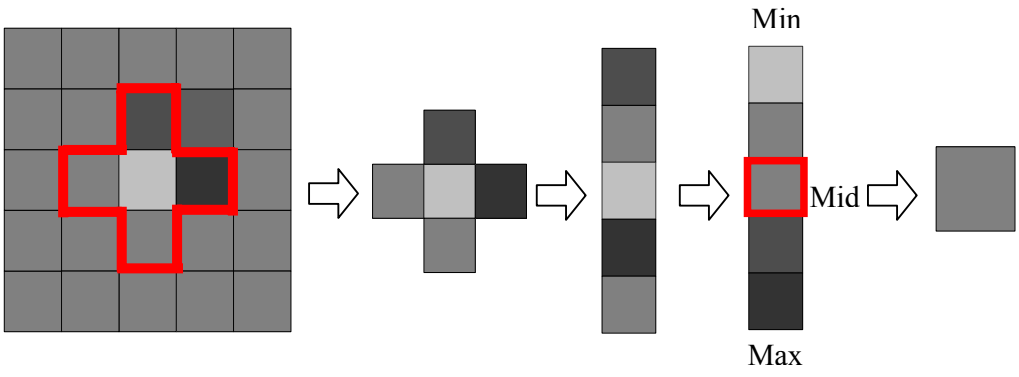


(b) Color filtering

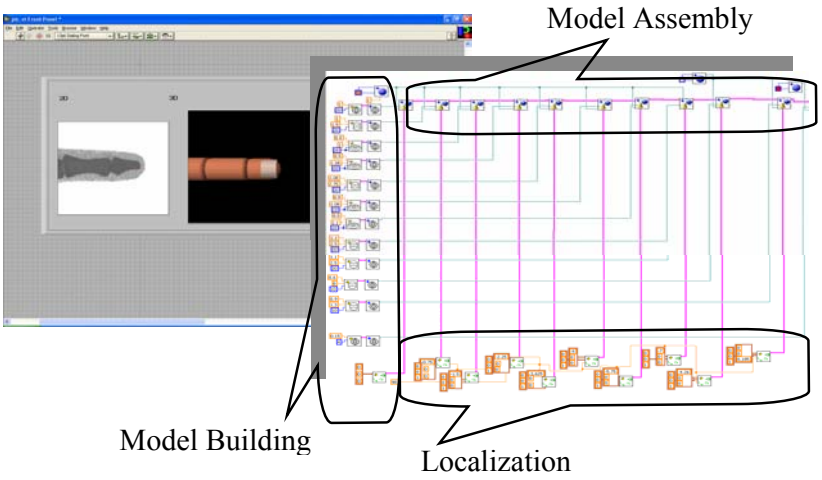


(c) 3D Modelling

Figure 8.10 The display unit.

The 3D model was built up according to the 2D picture. Since the structure of the finger, including tissue, bone, and nail, is too complicated to express by simple functions, the 3D finger was made up of several simple components as shown in Fig. 8.10(c). All of the components were built up on the left of the back diagram, and the location of each component could be set at the bottom of the window.

People can choose any direction to observe the 3D model and control the cursor movement along the X, Y or Z axes by the control knobs as shown in Fig. 8.11. The vision control bar and the control knobs are the components of the control units in the program.

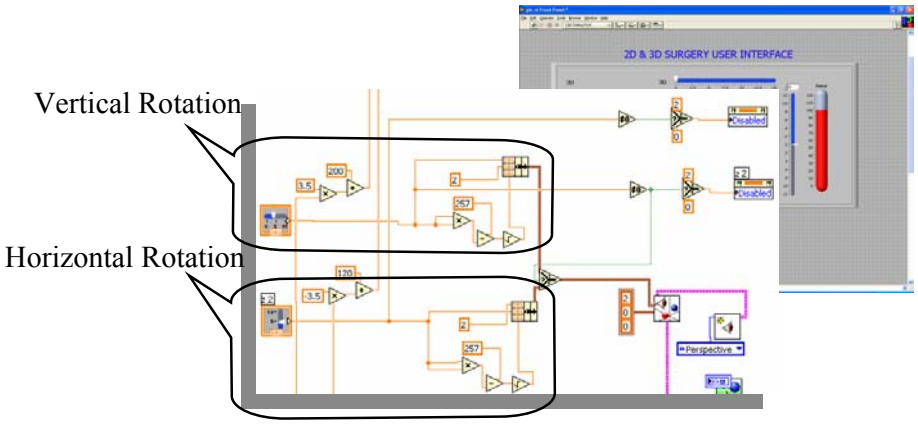


(a) 3D vision control bar

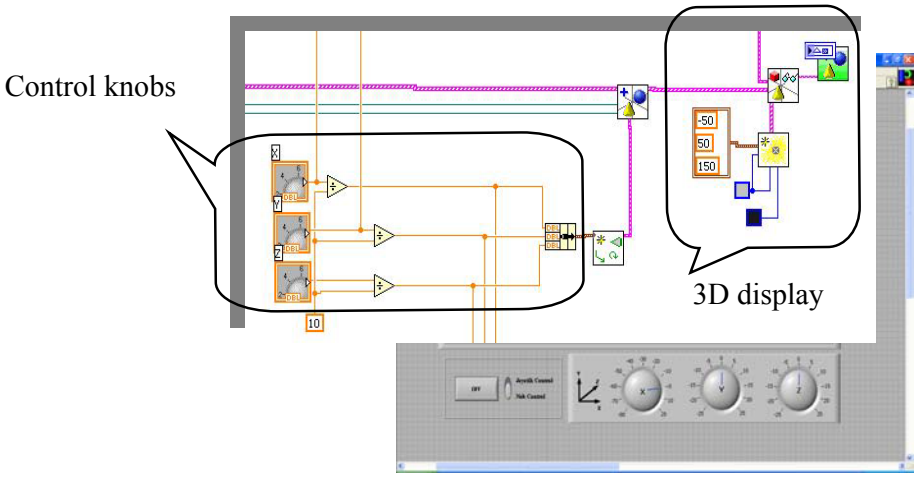


(b) Control knobs

Figure 8.11 The control unit.

DAQmx single sets were used to compose the DAQ system program in a while loop structure as shown in Fig. 8.12. The Start Task and the Stop Task sets were necessary outside the while loop, so that the CPU resources could be effectively used by the 3D remodelling when a DAQ procedure was finished. The working frequency of this system was chosen to be 100Hz and set by a timer in the loop structure. The case structure was used to switch between joystick and knob control modules. The 2D and 3D surgery user interface for the MR haptic joystick is shown in Fig. 8.13 by linking all the functions presented before.

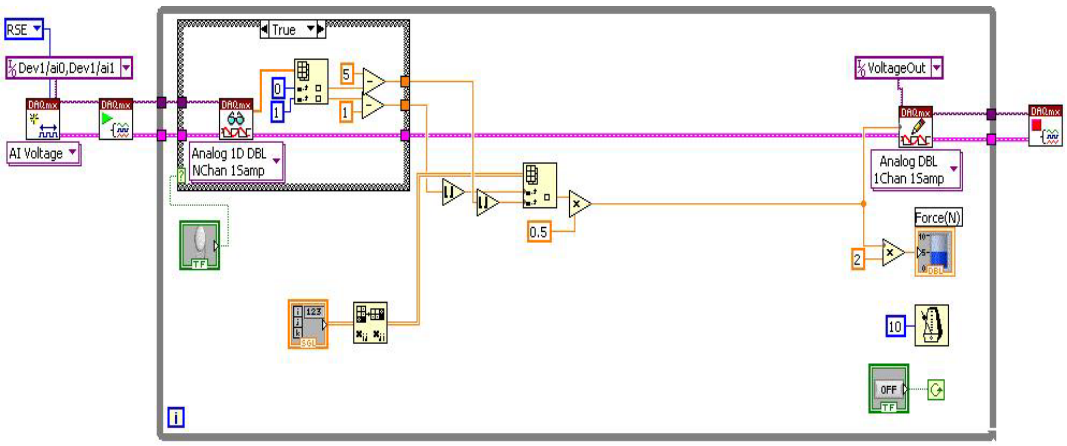


Figure 8.12 Data acquisition with DAQmx.

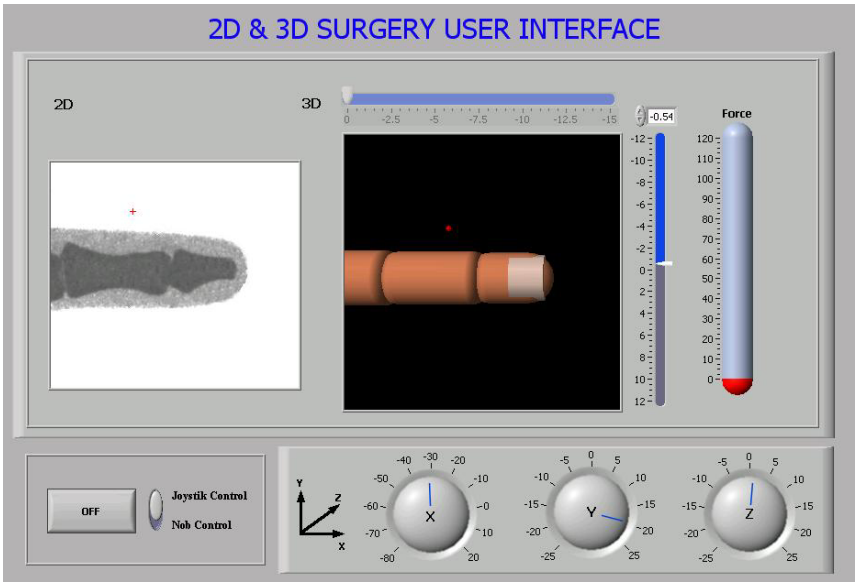


Figure 8.13 2D and 3D surgery user interface.

# CHAPTER 9
# CONCLUSIONS AND FUTURE WORK

The MR haptic joystick system presented in this thesis is an MR-fluid-based haptic system designed for several VR applications. This project attempts to explore a new way to extend MR applications by developing a 2-DOF force feedback system with a combination of MR devices and computer control. In the first part of this chapter, the main contributions of this project will be summarized and the characteristics of this system will be outlined. The second part will suggest the direction for further research work toward commercialization.

## 9.1 SUMMARY

The main contributions of this project can be divided into four aspects: 1) Design, testing and modelling of a compact position-feedback MR actuator; 2) MR joystick design, and working space and torque converting analysis; 3) DAQ strategy and power amplifier design; and 4) Software programming.

- **MR Actuator**

The finite element method was used in the mechanical design of the MR actuator. The optimized structure enables the actuator to work in the linear area and adequately utilize the magnetic and electrical energy. The clockwise/counter-clockwise rotary features and hysteresis features were tested experimentally, and a parametric sub-hysteresis model was proposed based on the results of the tests, providing an accurate torque control for haptic applications.

- **MR Joystick**

The MR joystick could generate a resistant force according to the VR circumstances by combining a pair of rectangular torques. The gimbal structure played an important role in the torque conversion. So, the torque calculation and the working space analysis were discussed in the joystick mechanical design section. Considering the practicability of the

joystick for VR applications, a pseudo 3D strategy was proposed, and the working surface and space deformation was calculated.

- **Electric Circuit Design**

This part includes DAQ hardware and the power amplifier circuit. DAQ card and sensor selection, sample rate, filtering and digitization principles were discussed, and the parameters of the DAQ components were calculated and determined in the DAQ system design. A current limiting power amplifying circuit was designed to provide the MR joystick with a safe and steady power source.

- **Software Design**

The program designed in this project works as the brain of the system and makes all the hardware work together in a certain order. The control unit and the display unit designs were the main task of the software design work. The DAQmx functions provided by LabVIEW were used to acquire a position signal from the joystick and to send out a control signal to the power amplifier. As the visual interface of this system, six different programs were developed for various VR applications.

The objective of this project is to overcome the distinct shortcomings of motor-based haptic devices by developing and using the MR haptic joystick. The system composed by the MR actuators and the joystick possesses the following features:

- The actuators are able to provide stepless control fitting for virtual applications, such as virtual surgery training.
- This MR joystick provides a wide resistance torque range (up to 1000Ncm), which can meet various applications of virtual reality.
- A sub-hysteresis model and a torque composing technique are proposed to accurately predict the joystick performance.
- Virtual instrument techniques are employed in this haptic system. The application of virtual instruments has the following advantages: (a) modularized system for easy maintenance; (b) a user-friendly interface for the people who are not familiar with computer controls.

- The 1D, 2D and 3D interfaces are demonstrated to show basic applications of the developed system.

## 9.2 FUTURE WORK

To realize the commercial potential of this haptic system, the volume and weight of the MR actuators need further reduction in order to meet more demanding industrial applications.

The current MR joystick can only provide passive resistance forces. The next generation of the MR haptic joystick should provide both passive resistant forces and active elastic forces in a 3D space. A group of magnetic torsion spring clutches with different elastic coefficients will be installed on each axis of the gimbal structure of the current MR joystick to generate active elastic torques. An MR damper with springs will be used as the handle of the joystick, which will make the device perform real 3D haptic simulations. Meanwhile, the clutch group control strategy needs to be developed as well.

Distribution control and telecommunication through the Internet or Ethernet will be added into the next generation system to realize remote haptic applications. For instance, a doctor, performing surgery using a robot arm from a distance or even from a different country, can feel the corresponding force through this haptic system when the surgical instruments touch the different organs of the patient.

The model developed in this thesis is based on low speed testing. By taking the varying speed and the acceleration into consideration, the fluid-dynamic and mechanical-dynamic model will be developed to enhance the force control accuracy. Meanwhile, the new 3D model designed in the OpenGL language will accelerate the graphic and 3D remodelling procedure.

# REFERENCES

[1] H. Block and P.J. Kelly, “Electro-Rheology”, Journal of Physics, D: Applied Physics, Vol. 21, pp. 1661, 1988.

[2] W.H. Li, G.Z. Yao, G. Chen, S.H. Yeo, and F.F. Yap, “Testing and steady state modelling of a linear MR damper under sinusoidal loading”. Smart Materials and Structures, 9, pp. 95-102, 2000.

[3] X.J. Wang and F. Gordaninejad, “Lyapunov-based control of a bridge using magneto-rheological fluid dampers”, Journal of Intelligent Material Systems and Structures, 13, pp. 415-419, 2002.

[4] K. Salisbury, D. Brock, T. Massie, N. Swarup, and C. Zilles, “Haptic rendering: programming touch interaction with virtual objects”, Proc. Symposium on Interactive 3D Graphics, ACM. pp.123-130, 1995.

[5] V. Hayward and O.R. Astley, “ Haptic Interfaces and Devices”, Sensor Review, 24(1), Feb. 2004.

[6] P.J. Rankin, A.T. Horvath and D.J. Klingenberg, Rheologica Acta 38, pp. 471, 1999.

[7] J. Rabinow, “The magnetic fluid clutch”, AIEE Transactions, 67, pp.1308-1315, 1948.

[8] J.D. Carlson, D.M. Catanzarite and K.A. St. Clare, “Commercial magnetorheological devices”, Proceedings of the 5th International Conference on ER fluids, MR suspensions and their applications, pp. 20-28, 1996.

[9] M.R. Jolly, J.W. Bender and J.D. Carlson, “Properties and applications of commercial MR fluids”, Journal of Intelligent Material Systems and Structures, 10, pp. 5-13,1999.

[10] S. Genç and P. Phulé “Rheological properties of magnetorheological fluids”, Smart Mater. Struct. 11, pp. 140-146, 2002.

[11] A. Osama, C.A. Rogers and W. Kordonsky, “Magnetorheological Fluids: Materials, Characterization, and Devices”, J. Intell. Mater. Syst. and Struct., 7, pp.123, 1996.

[12] Brownian motion, http://www.britannica.com/nobel/micro/88_96.html

[13] J.L. Meins, P. Moldenaers and J. Mewis, “Suspensions of monodisperse spheres in polymer melts: particle size effects in extensional flow”, 42, 1-2, pp 184-190, 2003.

[14] M. Hagenbuchle and J. Liu, “Rheology of Magnetorheological fluid”. J. Intell. Mater. Syst. and Struct., 7, pp.589-593, 1996.

[15] T.C. Hasley, J.E. Martin and D. Adolf, “Rheology of Electrorheological fluids”, Phys. Rev. Lett. 68, pp.1519-1522, 1992.

[16] G.R. Burgos and A.N. Alexandrou, “On the determination of Yield Surfaces in Herschel-Bulkley Fluids”. J.Rheol., 43, pp.463-483, 1999.

[17] M.R. Jolly and J.D. Carlson, “Controllable Squeeze Film Damping Using Magnetorheological Fluid” Actuator 96, 5th Int. Conf. on New Actuators, eds. H. Borgmann and K. Lenz, Axon Technologies Consult GmbH, 1996.

[18] R.W. Phillips, "Engineering Applications of Fluids with a Variable Yield Stress", Ph.D. Thesis, University of California, Berkeley, 1969.

[19] Z. Lou, D. Ervin and F.E. Filisco, “A preliminary Parametric Study of Electrorheological Dampers”, J. Fluid Mechanics, Transactions of ASME, 116, pp.570-576, 1994.

[20] F. Gordaninejad, and D.G. Breese, “ Magneto-Rheological Fluid Damper’, US Patent No.6, 019, 201, 2000.

[21] J.D. Carlson and K.D. Weiss, US Patent 5,382,373 1995.

[22] Lord Corporation. http://www.lord.com. 2005

[23] Carrera Shocks product brochure: MagneShock.

[24] E.M. Shtarkman, US Patent 4,942,947 1990.

[25] S.B. Gentry, J.F. Mazur and B.K. Blackburn, US Patent 5,460,585 1995.

[26] J.D. Carlson and K.D. Weiss, US Patent 5,382,373 1995.

[27] Chase VD, Appliance Manufacturer 1996:6.

[28] W. Vogt, Equipment Today, September 1995.

[29] T.G. Duclos, Future Transportation Tech. Conf. and Exp., San Francisco, CA, Aug. pp.8-11, 1988.

[30] E.M. Shtarkman, US Patent 5,176,368 1993.

[31] T. Erickson, “Artificial Realities as data visualization environments: problems and prospects”, in A. Wexelblat, ed., “Virtual Reality - Applications and explorations”, pp. 3-22, Academic Press, London, 1993

[32] F. Biocca and M.R. Levi, “Virtual Reality as a Communication Medium” in F. Biocca and M.R.Levi, eds., “Communication in the Age of Virtual Reality”, pp. 15-32, Lawrence Erlbaum Ass., Hove, UK, 1995.

[33] D.N. Chorafas and H. Steinmann, "Virtual Reality: Practical applications in business and industry" (sections 1 and 2), Prentice Hall, London, 1995.
[34] N.O. Bernsen, "A taxonomy of input modalities", 1996, the Amodeus-II WWW-site, http://www.mrc-apu.cam.ac.uk /amodeus/

[35] C. Cadoz, and C. Ramstein, "Capture, representation, and composition of the instrumental gesture", Proc. International Computer Music Conference, pp. 53-56, 1990.

[36] M. Akamatsu, S. Sato, and I.S. MacKenzie, "Multimodal mouse: A mouse-type device with tactile and force display", Presence, 3: pp. 73-80, 1994.

[37] D.V. Keyson, Touch In user in interface navigation, Ph.D. Thesis, Technische Universiteit Eindhoven. Netherlands, 1996.

[38] Sensable Techonologies: Introduction to Phantom system, http://www.sensable. com/, retrieved Oct. 5, 2005.

[39] PHATOM: http://www.sensable.com/products/phantom_ghost/overview.asp

[40] W. McNeely, K. Puterbaugh and J. Troy, "Six degree-of-freedom haptic rendering using voxel sampling". Proc. of ACM SIGGRAPH, pp. 401-408, 1999.

[41] H. Kajimoto, N. Kawakami, S. Tachi, and M. Inami, "Smarttouch: Electric skin to touch the untouchable," IEEE Computer Graphics and Applications, vol. 24, Issue 1, pp. 36 – 43, 2004.

[42] K. Kaczmarek, J. Webster, P. Bach-y-Rita, and W. Tompkins, "Electrotactile and vibrotactile displays for sensory substitution systems," IEEE Transactions on Biomedical Engineering, vol. 38, Issue 1, pp. 1– 16, 1991.

[43] M. Richard J. Voyles, G. Fedder, and P.K. Khosla, "Design of a modular tactile sensor and actuator based on an electrorheological gel", IEEE International Conference on Robotics and Automation, Minneapolis, MN, April 1996.

[44] Y. Bar-Cohen, C. Mavroidis, M. Bouzit, C. Pfeiffer and B. Dolgin, "Remote mechanical mirroring using controlled stiffness and actuators (MEMICA)," Rutgers Docket Number 99-0056 A US and International PCT patent application was filed by Rutgers University, September 2000.

[45] Electrorheological joystick: http://www.robots.neu.edu/ERF/Joystick.htm

[46] Magnetorheological glove: http://www.vancouver.wsu.edu/fac/hgurocak/Haptic. html

[47] Y. Yamaguchi, J. Furusho, K. Koyanagi, and S. Kimura, "Development of 2-D Force Display System Using MR Actuators", Proceedings of the 13th International Conference on Artificial Reality and Telexistence, pp.185-190, 2003.

[48] Introduction to Pulse Width Modulation: http://www.netrino.com/Publications/ Glossary/PWM.html

[49] W.H. Li, H. Du and N.Q. Guo. "Finite Element Analysis and Simulation Evaluation of a Magnetorheological Valve". International Journal of Advanced Manufacturing Technology , 21, pp. 438-445, 2003.

[50] Cosmos(2005).CosmosEMS. retrieved Aug, 2005. http://www.cosmosm.com/ pages/products/cosmosems.html

[51] J.D. Carlson, D.F. Leroy and J.C. Holzheimer, et al., "Controllable Brake", US Patent 5, 842, 547, 1998.

[52] MRF-132AD Product Bulletin.

[53] R.G. Dong, T.W. Mcdowell and D.E. Welcome, "Biodynamic Response at the Palm of the Human Hand Subjected to a Random Vibration", Industrial Health, 43, pp. 241–255. 2005.

[54] G. Seval and P. Pradeep, "Rheological properties of Magnetorheological fluids" Smart Materials and Structure, pp. 140-146, February 2002.

[55] Magnetic_circuit_design: http: // literature.lord.com / root / other / rheonetic / Magnetic _Circuit _Design.pdf

[56] Solidworkd: http://www.solidworks.com/

[57] Steels-carbon steels, mild steel, carbon-manganese steels, alloys steels, low-alloy steels and micro-alloy steels. retrieved Aug, 23,2005. from: http://www.azom.com/details.asp?ArticleID=2537

[58] T. Butz and O. V. Stryk. "Modelling and Simulation of Rheological Fluid Devices". Preprint SFB-438-9911, Sonderforschungsbereich 438, Techniche Univerität München, May 1999.

[59] Georgia State University(2005) Hysteresis in ferromagnetic material. retrieved Aug, 23,2005. http://hyperphysics.phyastr.gsu.edu/hbase/solids/hyst.html

[60] Foundation of data acquisition: http://www.ni.com/dataacquisition/

[61] M Series DAQ: http://sine.ni.com/nips/cds/view/p/lang/en/nid/ 14114
[62] NI PCI-6211 reference label.

[63] NI SCB-68 68-Pin shielded connector block user manual.

[64] NI LabVIEW Development Systems (2005) Retrieved Aug, 23, 2005. from: http://www.ni.com/labview/

[65] DAQmx technique: http://www.ni.com/dataacquisition/nidaqmx.htm

# APPENDIX A:
# PROPERTIES OF MR FLUID – MRF-132AD

| Properties | Value/Limits |
|---|---|
| Base Fluid | Hydrocarbon |
| Operating Temperature | -40$^{o}$C – 130$^{o}$C |
| Density | 3.09 g/cc |
| Colour | Dark gray |
| Weight Percent Solids | 81.64% |
| Coefficient of Thermal Expansion (calculated values) | Unit Volume per $^{o}$C |
| 0 to 50$^{o}$C | 0.55 x $10^{-3}$ |
| 50 to 100$^{o}$C | 0.66 x $10^{-3}$ |
| 100 to 150$^{o}$C | 0.67 x $10^{-3}$ |
| Specific Heat @ 25$^{o}$C | 0.80 J/g $^{o}$C |
| Thermal Conductivity @ 25$^{o}$C | 0.25 - 1.06 w/m $^{o}$C |
| Flash Point | >150$^{o}$C |
| Viscosity<br>Calculated for slope between 800 1/s and 500 1/s at 40$^{o}$C | 0.09 (+/-0.02) Pa-s. |

# APPENDIX B:
# SUB-HYSTERESIS MODEL PROGRAM

```
%The initialization--To locate the initial torque %
clc
Is=0.6;
S1=387.5;
S2=233.3;
T0=45;
T1=(S2-S1)*Is+T0;

disp('You are running the MR sub-hysteresis force prediction program ');
while (1)
  I0=input('Please input the valid initial current(0-3A): ');
  if (I0<=3)&&(I0>=0)
           if I0<=Is
                Ib=0;
                It=Is;
                T=S2*I0+T0;
           else
                Ib=I0-Is;
                It=I0;
                T=S1*I0+T1;
           end
           disp('The Toqure is: (Ncm)');
          disp(T);
          plot(I0,T,'*r');
          axis([0 3 0 900])
          hold on;
         disp('Input the value(0-3A) of the control current if you want to continue')
         disp('Input "-1" if you want to stop');
          break
```

```
   else
        disp('Invalid initial value');
  end
end

%The closest to the I0 input is I1. In other words, the difference
%between I1 and I0 (I1-I0=dI) can be modelled as the increment or
%decrement of the electric current

while (1)
   I=input('Please input the current value: ')
   if (I<=3)&&(I>=0)
      if I<=It-Is
         dec=1;inc=0;
      elseif I-Ib>=Is
         dec=0;inc=1;
      else
         dec=0;inc=0;
      end

      dI=I-I0;
      if dI>0
         if inc==1
            It=I;Ib=I-Is;T=S1*I+T1;
         else
            T=S1*Ib+T0+S2*(I-Ib);
         end
             plot(I,T,'*r');
      elseif dI<0
         if dec==1
             Ib=I;It=I+Is;T=S1*I+T0;
         else
             T=S1*It+T1+S2*(I-It);
         end
```

```
            plot(I,T,'*b');
        else
            T=T;
        end
        I0=I;
        disp('The Toqure is: (Ncm)');
        disp(T);
    elseif I==-1
        disp('Program stop')
        break
    else
        disp('Invalid input')
    end
end
```

# APPENDIX C:

# MANUFACTURING DRAWINGS OF THE MR JOYSTICK

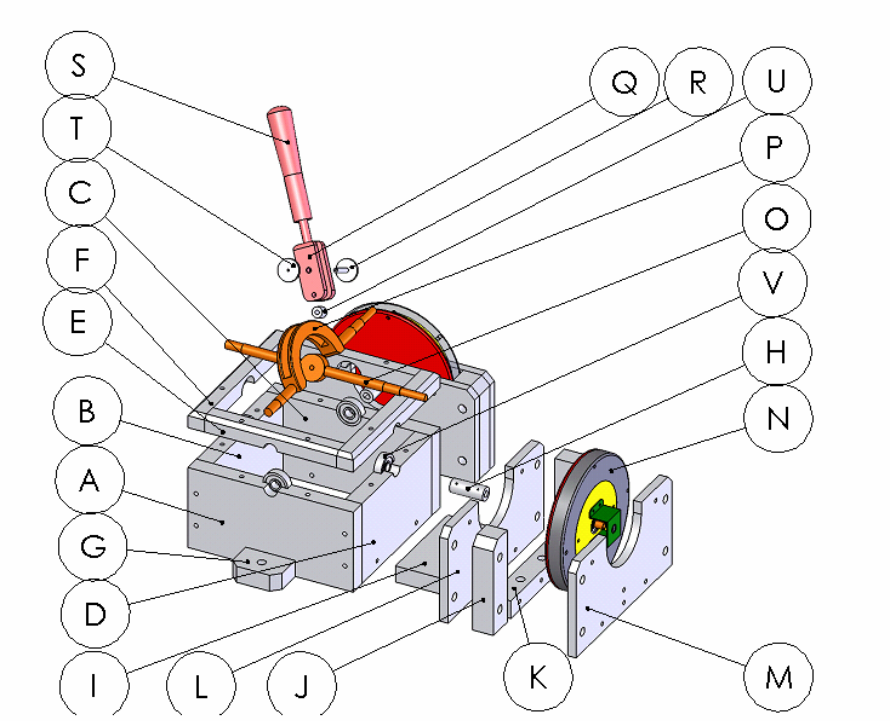


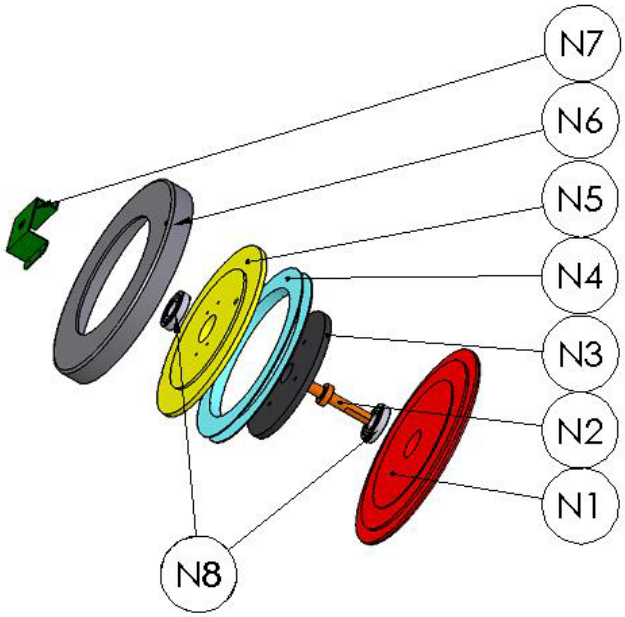


MR joystick and MR actuator

| Title | Code | Material | Amount |
|---|---|---|---|
| | A | Aluminium | 1 |
| | B | Aluminium | 1 |
| | C | Aluminium | 1 |
| | D | Aluminium | 1 |
| | E | Aluminium | 2 |
| | F | Aluminium | 2 |
| | G | Aluminium | 2 |
| | H | Standard steel | 2 |
| | I | Acrylic Board | 2 |
| | J | Acrylic Board | 4 |
| | K | Acrylic Board | 2 |
| | L | Aluminium | 2 |
| | M | Aluminium | 2 |
| | N | | 2 |
| | O | Standard steel | 1 |
| | P | Standard steel | 1 |
| | Q | Standard steel | 1 |
| | R | Standard steel | 1 |
| | S | Plastic | 1 |
| | T | Standard steel | 1 |
| | U | Aluminium | 1 |
| Ball bearing | V | (30mm(ED)x10mm(ID)x9mm(thick)) | 4 |
| | N1 | Mild steel | 2 |
| | N2 | Standard steel | 2 |
| | N3 | Mild steel | 2 |
| | N4 | Aluminium | 2 |
| | N5 | Mild steel | 2 |
| | N6 | Mild steel | 2 |
| | N7 | Aluminium | 2 |
| Sealed bearing | N8 | 608-2RSH (22mm(ED)x8mm(ID)x7mm(thick)) | 4 |

Material list for the MR haptic joystick

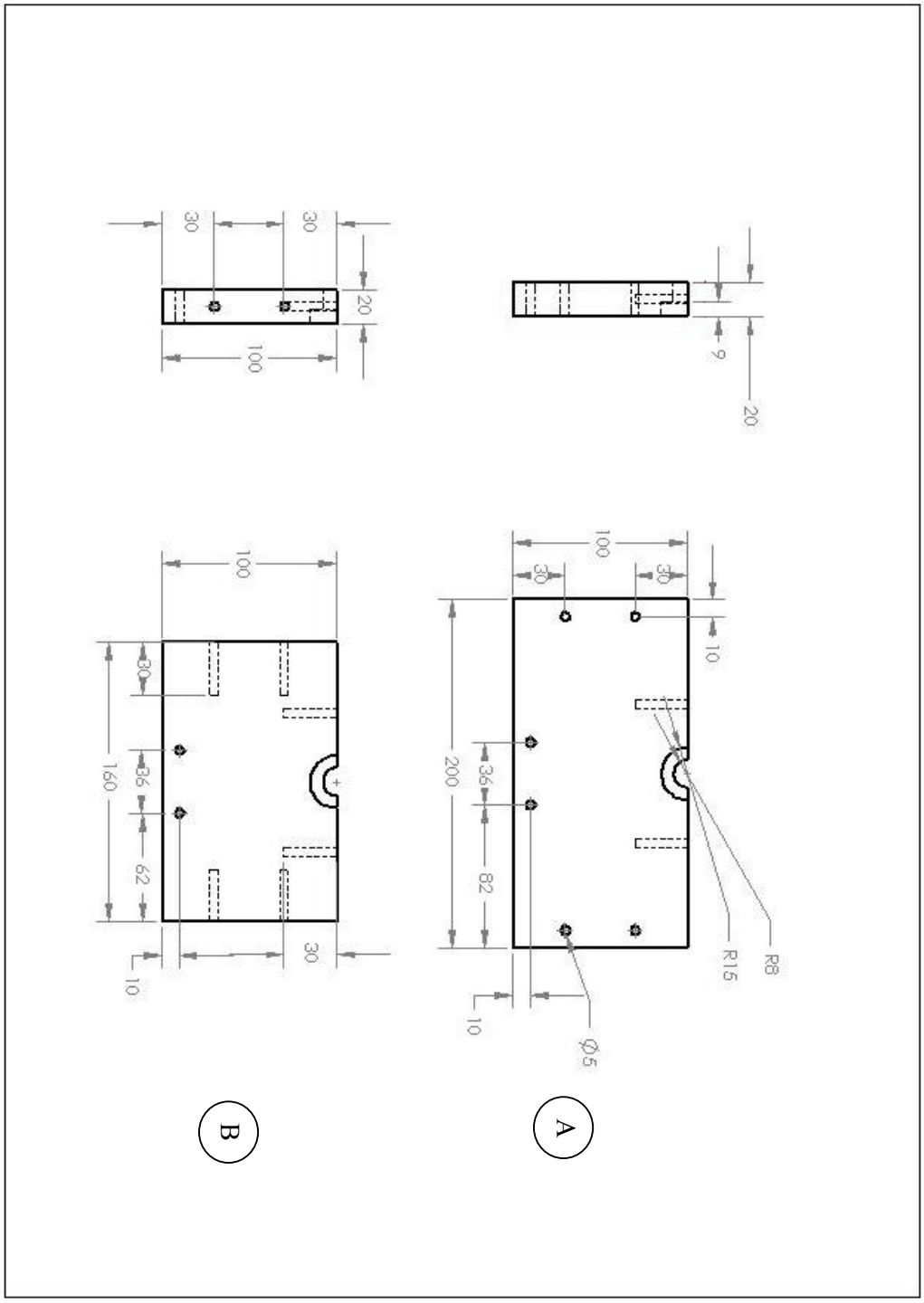
30
30
20
100
9
20
100
30
30
10
200
36
82
R15
R8
10
Ø5
100
30
160
36
62
30
10
B
A

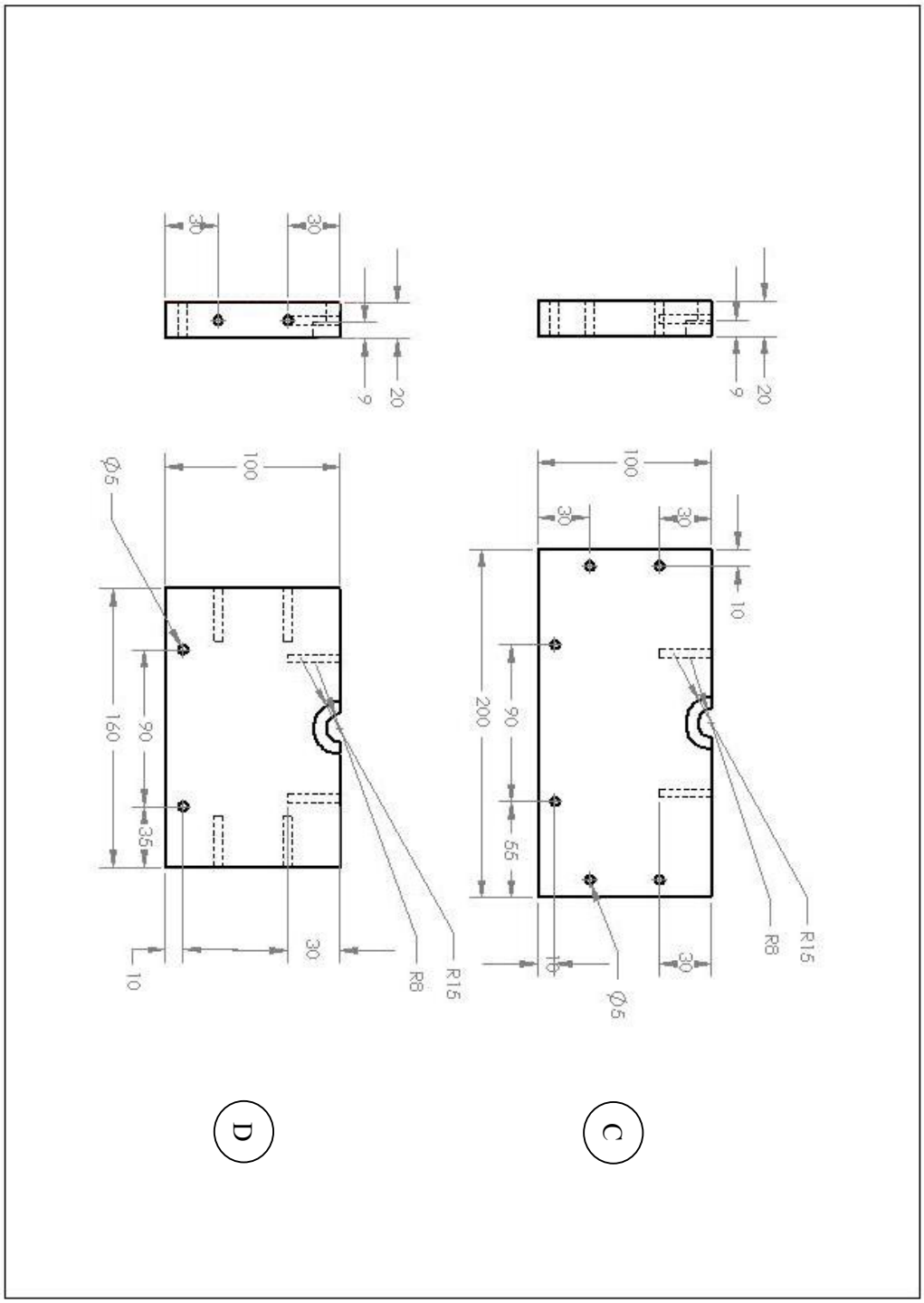
30
30
9
20
100
30
30
10
200
90
55
10
Ø5
R8
R15
30
D
C

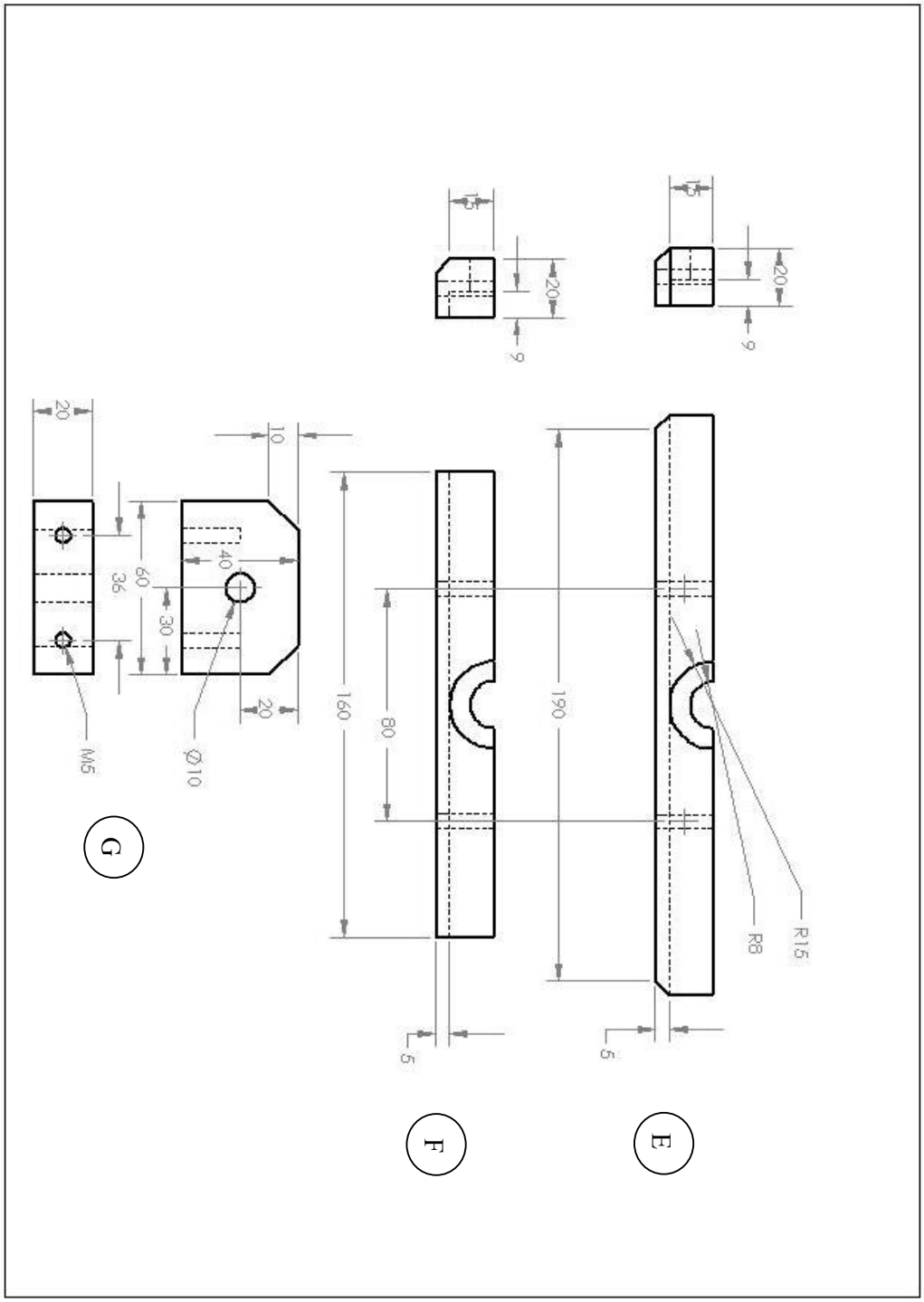
15
20
9
15
20
9
20
10
40
60
36
30
20
M5
Ø10
160
80
190
R8
R15
5
5
G
F
E

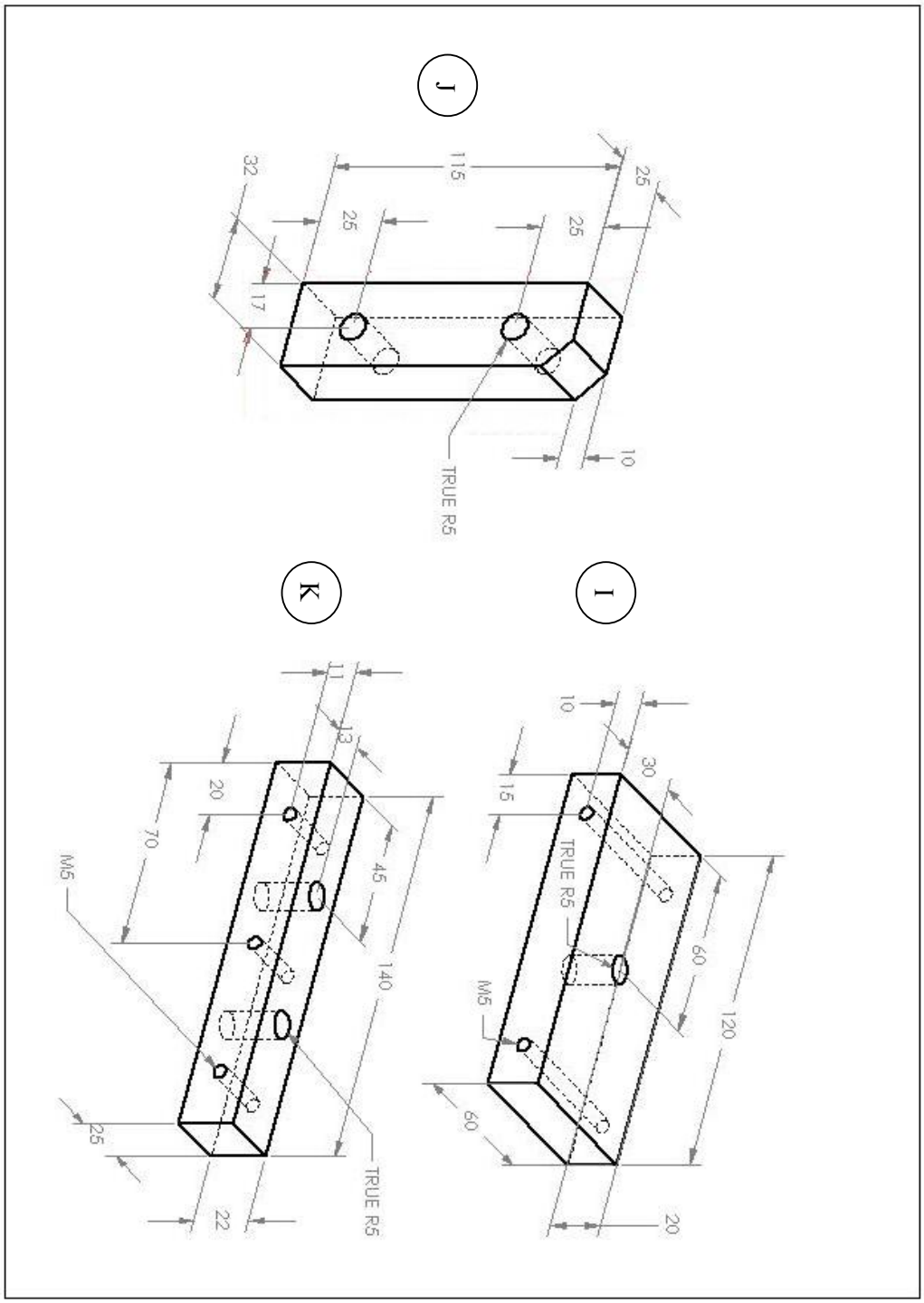
J
115
25
32
25
25
17
TRUE R5
10
K
I
11
13
20
70
45
140
M5
25
22
TRUE R5
10
30
15
TRUE R5
60
M5
120
60
20

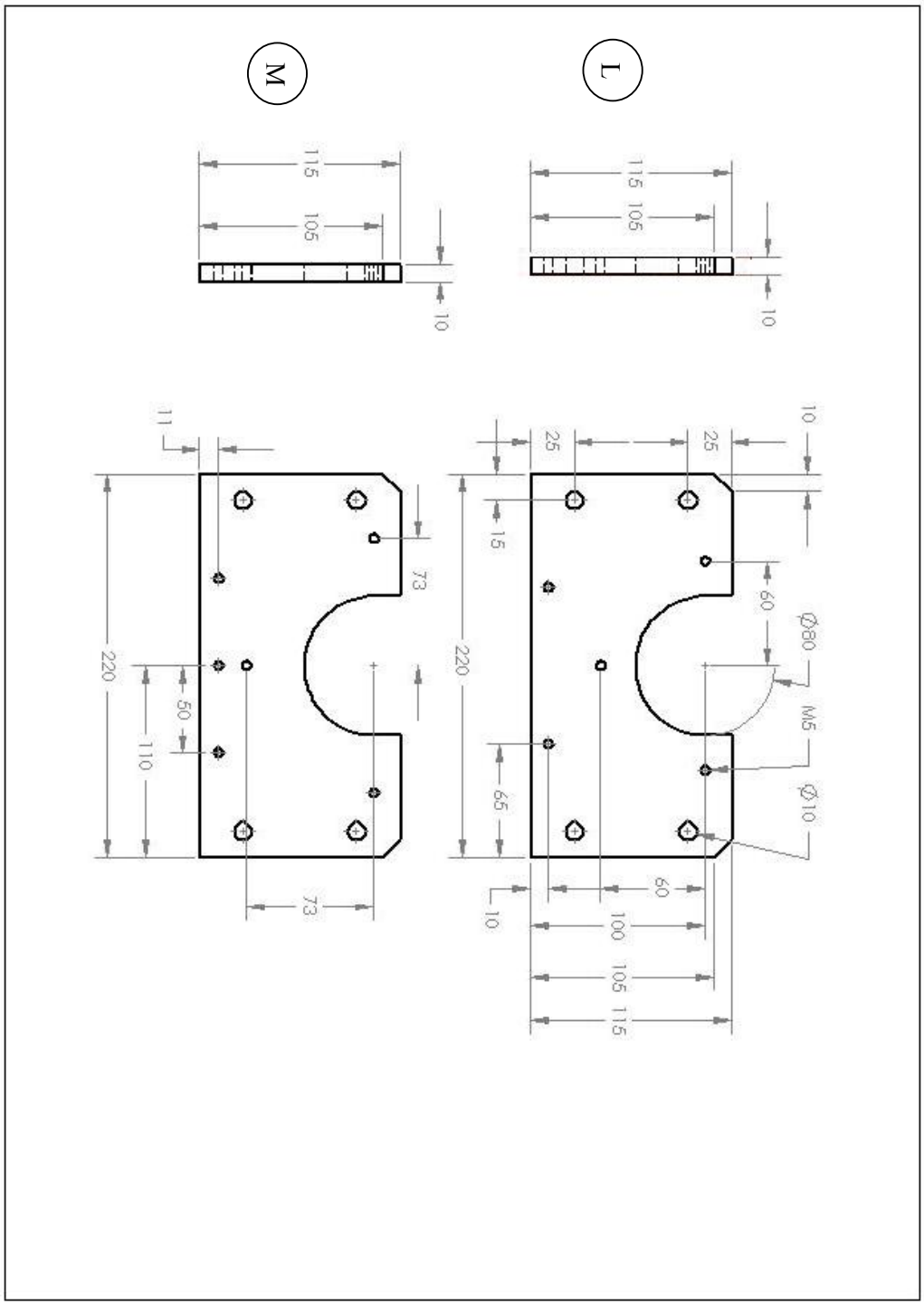
M
115
105
10
11
73
220
50
110
73
L
115
105
10
10
25
25
15
60
Ø80
M5
Ø10
220
65
10
60
100
105
115

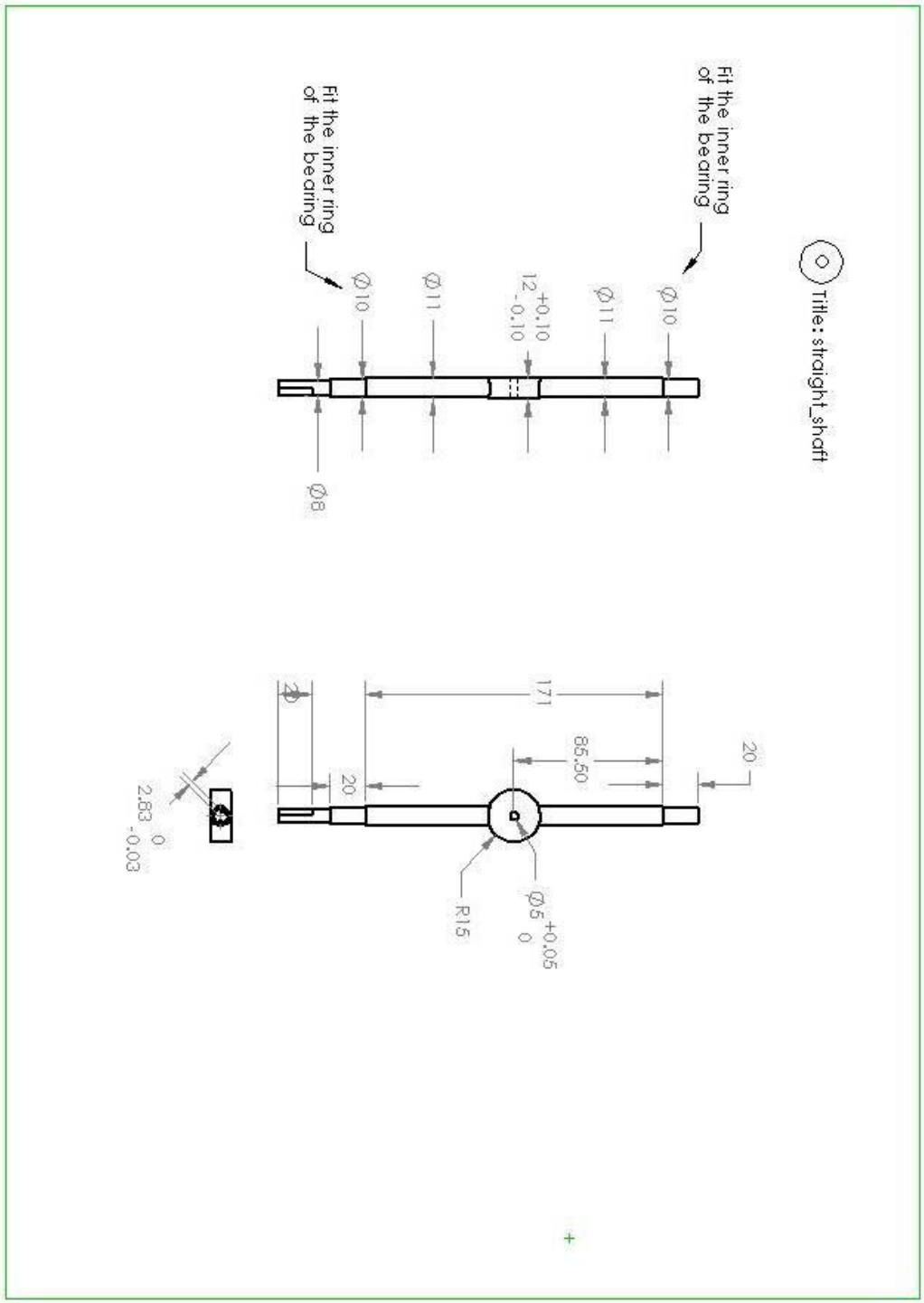
Title: straight_shaft
Fit the inner ring of the bearing
Fit the inner ring of the bearing
Ø10
Ø11
12 +0.10 -0.10
Ø11
Ø10
Ø8
171
85.50
20
20
R15
Ø5 +0.05 0
2.83 0 -0.03

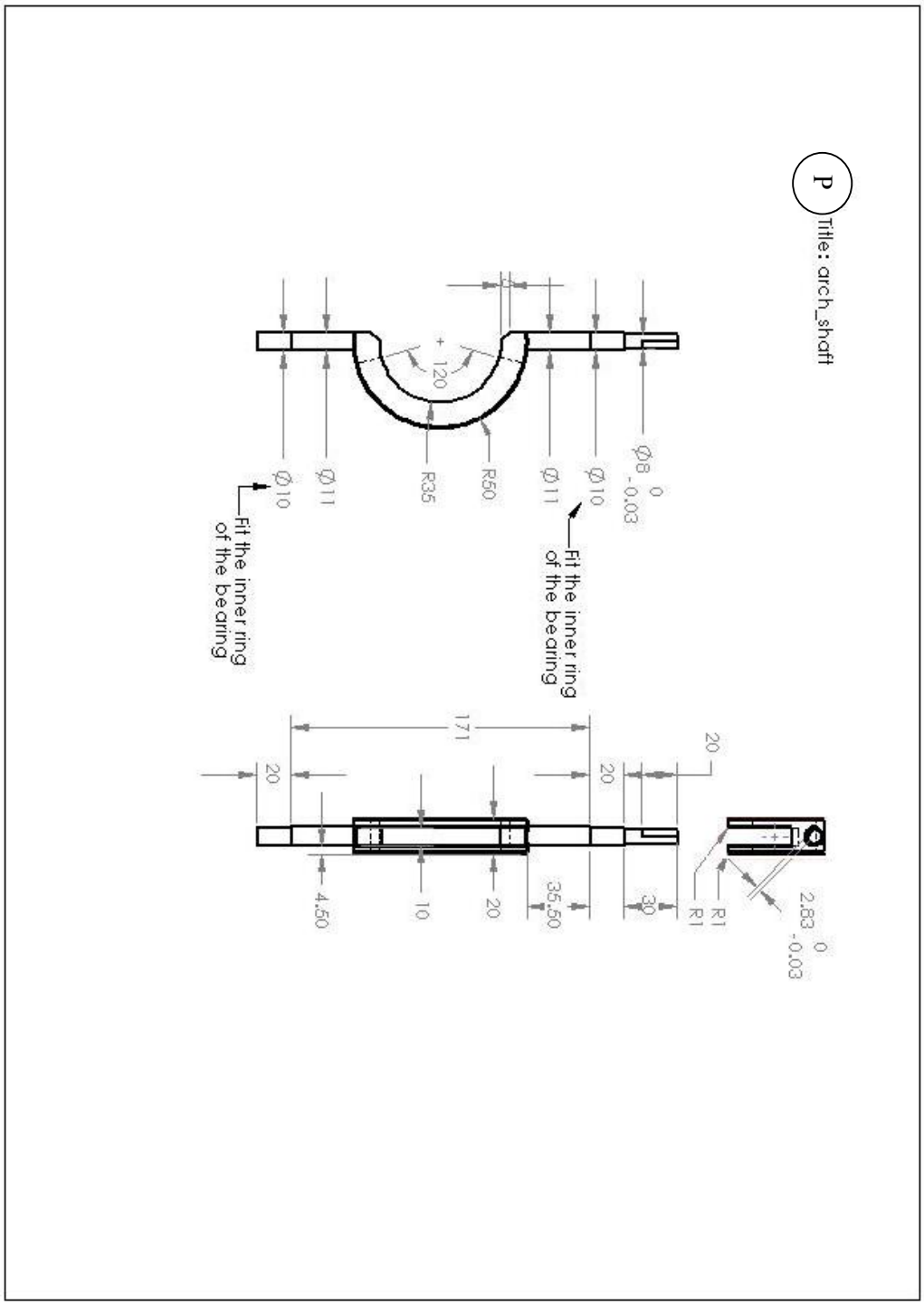
P
Title: arch_shaft
Ø8 0 -0,03
Ø10
Ø11
R50
R35
120
Ø11
Ø10
Fit the inner ring of the bearing
Fit the inner ring of the bearing
171
20
20
20
4,50
10
20
35,50
30
R1
R1
2,83 0 -0,03

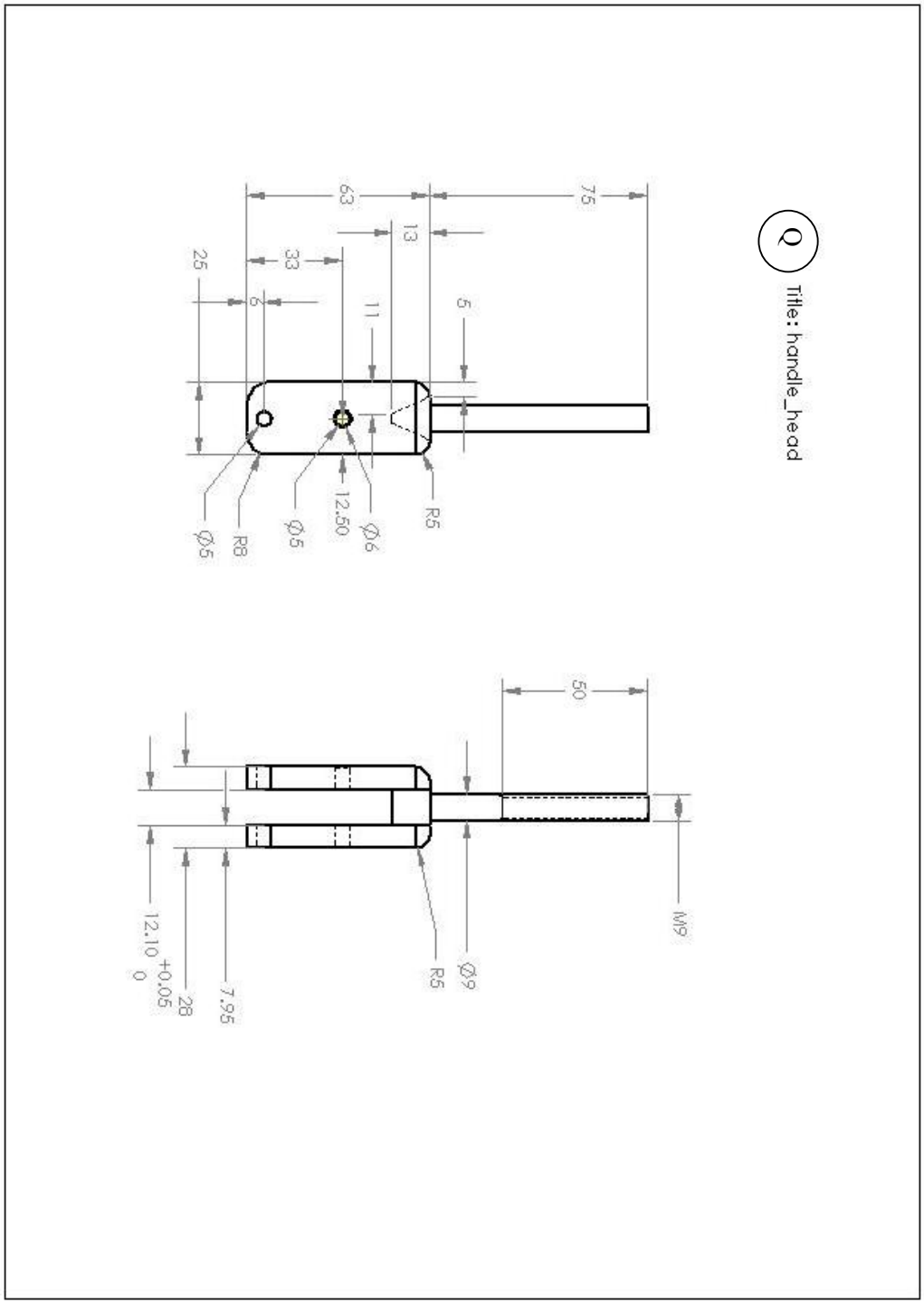
Q
Title: handle_head
63
75
13
33
25
8
11
5
Ø5
R8
Ø5
12.50
Ø6
R5
50
12.10 +0.05 0
28
7.95
R5
Ø9
M9

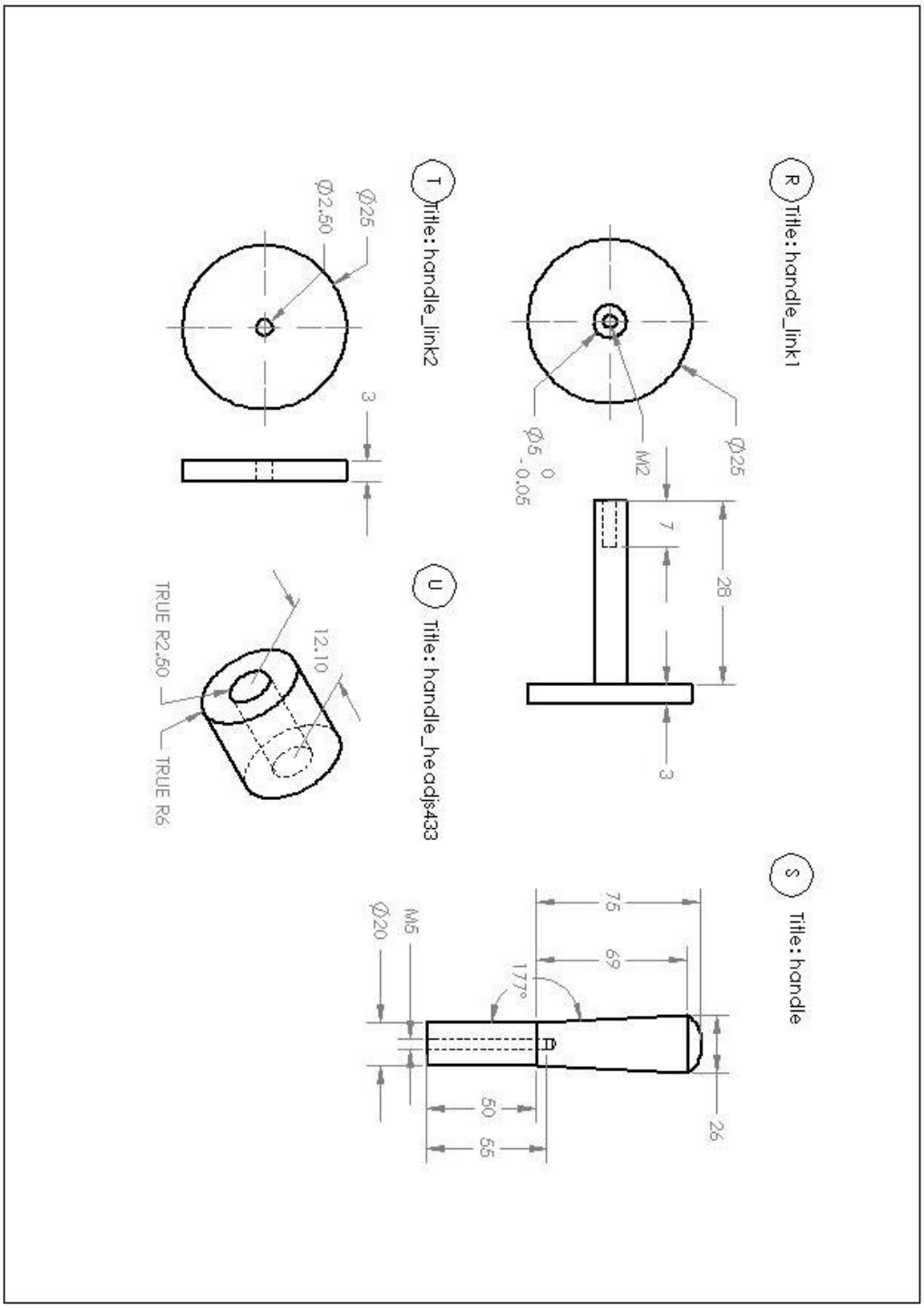
R
Title: handle_link1
Ø25
M2
Ø5 0 -0.05
7
28
3
T
Title: handle_link2
Ø25
Ø2.50
3
U
Title: handle_head|s433
12.10
TRUE R2.50
TRUE R6
S
Title: handle
75
69
177°
M5
Ø20
26
50
55

# APPENDIX D:
# SCB-68

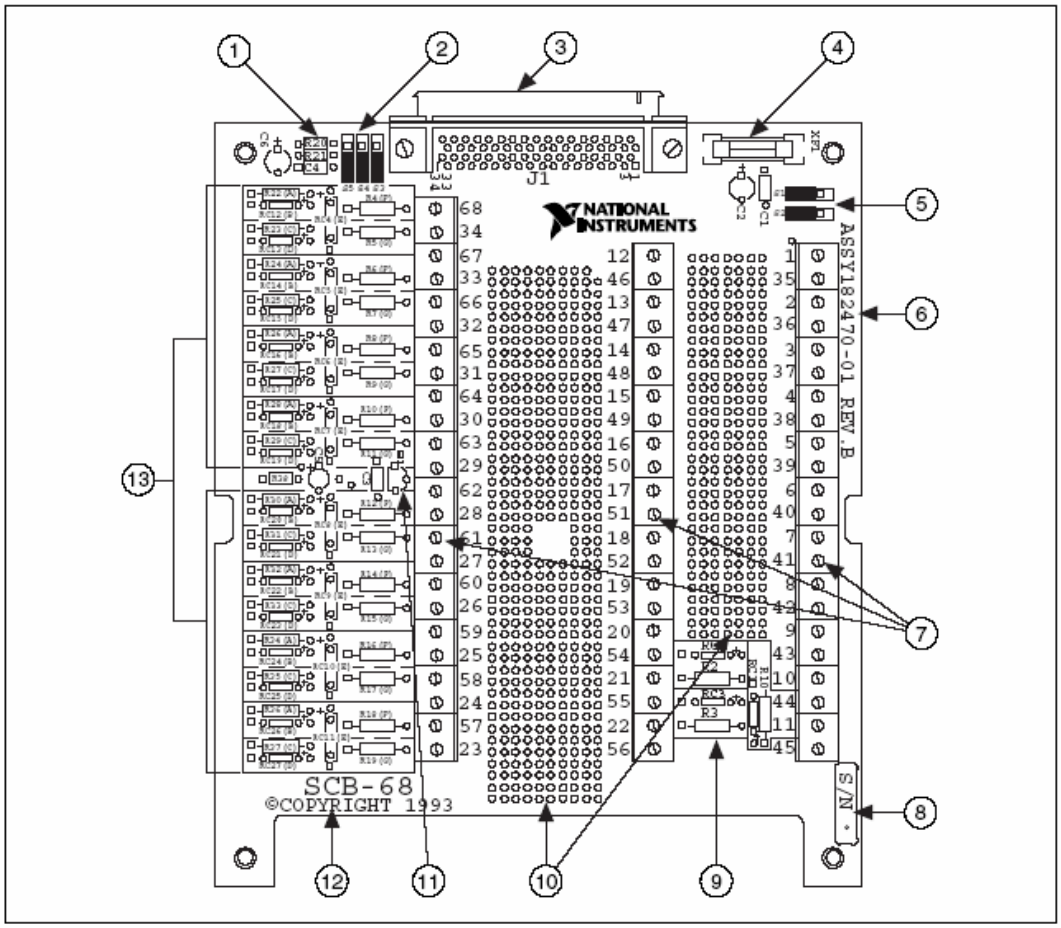


| | | | |
|---|---|---|---|
| 1 | Pads R20 and R21 | 8 | Serial Number |
| 2 | Switches S3, S4, and S5 | 9 | RC Filters and Attenuators for DAC0, DAC1, and TRIG1 |
| 3 | 68-Pin I/O Connector | 10 | Breadboard Area |
| 4 | Fuse (0.8 A) | 11 | Temperature Sensor |
| 5 | Switches S1 and S2 | 12 | Product Name |
| 6 | Assembly Number and Revision Letter | 13 | Pads for AI Conditioning |
| 7 | Screw Terminals | | |

SCB-68 Printed Circuit Diagram

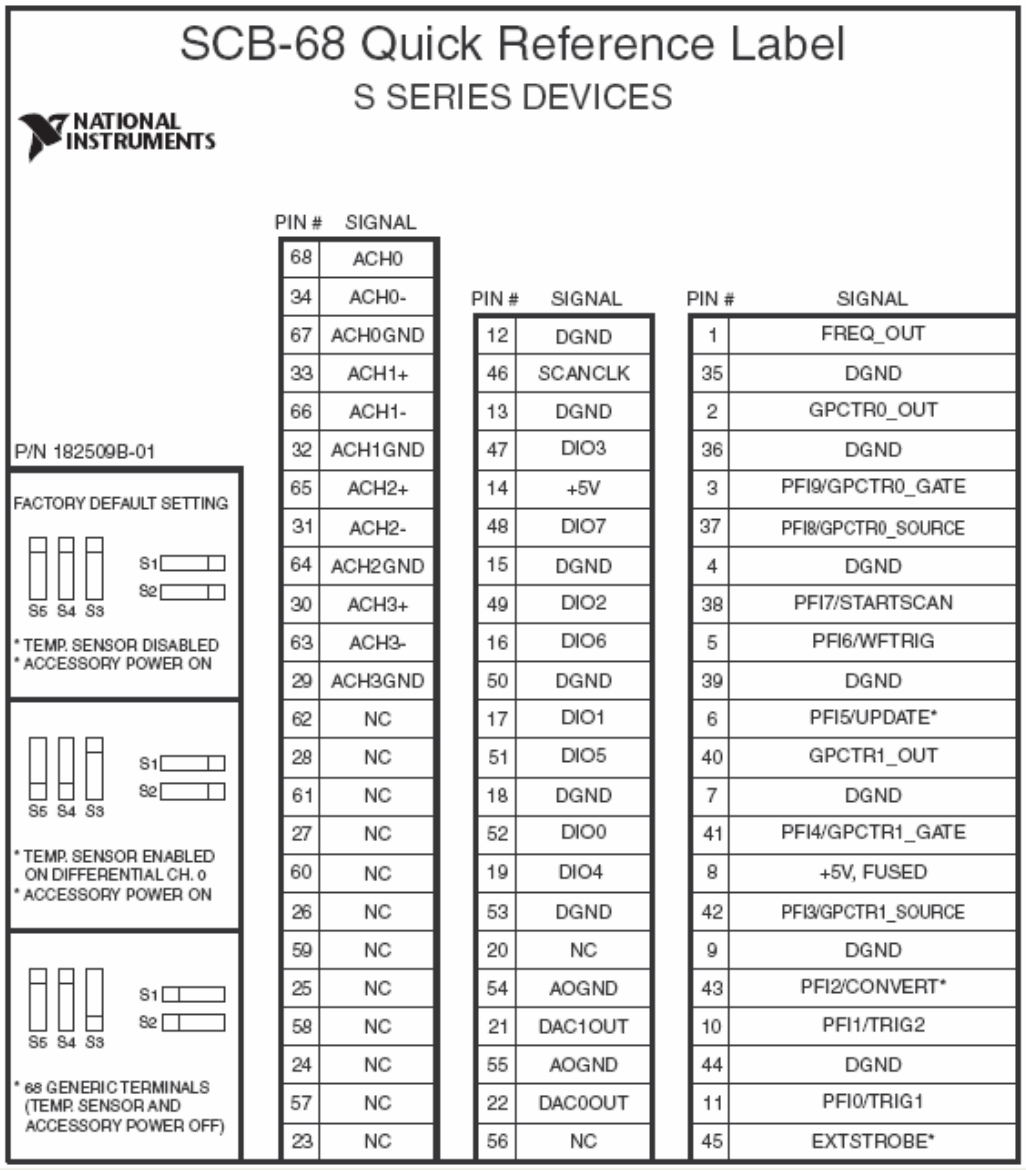

SCB-68 Quick Reference Label

S SERIES DEVICES

NATIONAL INSTRUMENTS

P/N 182509B-01

FACTORY DEFAULT SETTING

S1 S2 S5 S4 S3

* TEMP. SENSOR DISABLED
* ACCESSORY POWER ON

S1 S2 S5 S4 S3

* TEMP. SENSOR ENABLED ON DIFFERENTIAL CH. 0
* ACCESSORY POWER ON

S1 S2 S5 S4 S3

* 68 GENERIC TERMINALS (TEMP. SENSOR AND ACCESSORY POWER OFF)

| PIN # | SIGNAL |
|---|---|
| 68 | ACH0 |
| 34 | ACH0- |
| 67 | ACH0GND |
| 33 | ACH1+ |
| 66 | ACH1- |
| 32 | ACH1GND |
| 65 | ACH2+ |
| 31 | ACH2- |
| 64 | ACH2GND |
| 30 | ACH3+ |
| 63 | ACH3- |
| 29 | ACH3GND |
| 62 | NC |
| 28 | NC |
| 61 | NC |
| 27 | NC |
| 60 | NC |
| 26 | NC |
| 59 | NC |
| 25 | NC |
| 58 | NC |
| 24 | NC |
| 57 | NC |
| 23 | NC |

| PIN # | SIGNAL |
|---|---|
| 12 | DGND |
| 46 | SCANCLK |
| 13 | DGND |
| 47 | DIO3 |
| 14 | +5V |
| 48 | DIO7 |
| 15 | DGND |
| 49 | DIO2 |
| 16 | DIO6 |
| 50 | DGND |
| 17 | DIO1 |
| 51 | DIO5 |
| 18 | DGND |
| 52 | DIO0 |
| 19 | DIO4 |
| 53 | DGND |
| 20 | NC |
| 54 | AOGND |
| 21 | DAC1OUT |
| 55 | AOGND |
| 22 | DAC0OUT |
| 56 | NC |

| PIN # | SIGNAL |
|---|---|
| 1 | FREQ_OUT |
| 35 | DGND |
| 2 | GPCTR0_OUT |
| 36 | DGND |
| 3 | PFI9/GPCTR0_GATE |
| 37 | PFI8/GPCTR0_SOURCE |
| 4 | DGND |
| 38 | PFI7/STARTSCAN |
| 5 | PFI6/WFTRIG |
| 39 | DGND |
| 6 | PFI5/UPDATE* |
| 40 | GPCTR1_OUT |
| 7 | DGND |
| 41 | PFI4/GPCTR1_GATE |
| 8 | +5V, FUSED |
| 42 | PFI3/GPCTR1_SOURCE |
| 9 | DGND |
| 43 | PFI2/CONVERT* |
| 10 | PFI1/TRIG2 |
| 44 | DGND |
| 11 | PFI0/TRIG1 |
| 45 | EXTSTROBE* |

SCB-68 Reference Label

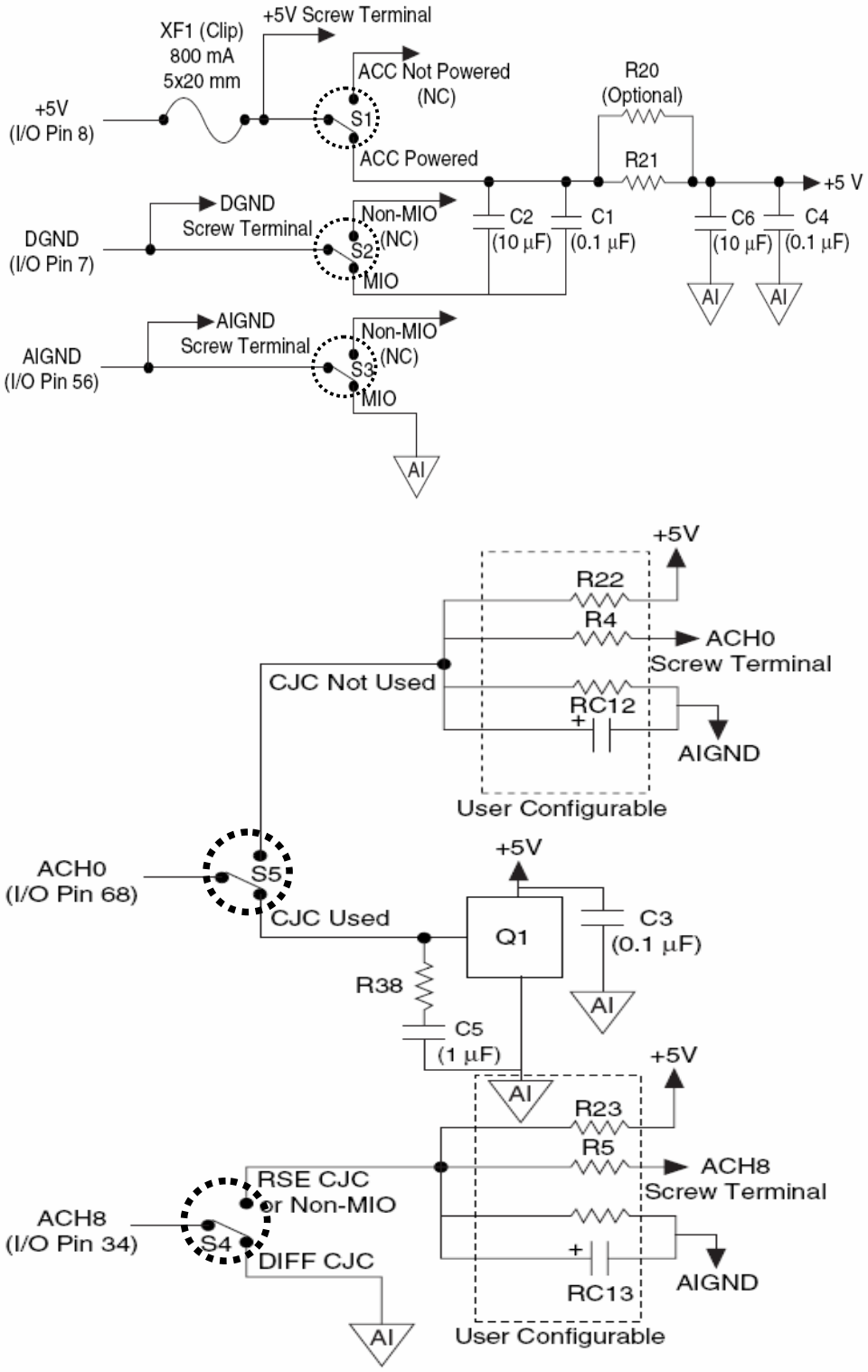


SCB-68 Jumpers Configuration